The Tomographic Reconstruction of Holographic
Interferograms

by Anthony Leslie Collins

Doctor of Philosophy
City University
Department of Mechanical Engineering and Aeronautics
December 1998

Contents

Acknowledgements

I would like to thank Dr F. Henry and Dr R. Preator for their supervision and assistance during the writing of this thesis. I would also like to thank Professor M. Collins for his supervision of this research and Mr R. Parker of Rolls Royce Plc for his support of this work. Finally I would like to thank Dr R. Swain for his assistance in producing holographic test data.

Abstract

The development of a tomographic reconstruction system for use with limited viewing angle data is described in this thesis. It covers the development of novel tomographic reconstruction software, the construction of a practical tomography system, and the testing of the system on real data.

The aim of this work was to produce a system which would allow the reconstruction in a computer of three dimensional density fields that had been recorded using holographic interferometry, from two dimensional views of the holograms. By their nature holograms have a restricted range of directions over which they may be viewed, whereas tomography usually relies on taking measurements about a wide range of views. Hence it was necessary to devise a means to overcome the loss of resolution that occurs in reconstructions when the angle of view is limited, as was the case with the holograms we used. This resulted in the principal novel development of this work, namely the use of a direct 3-D projection scheme in combination with an iterative reconstruction method using the Multiplicative Algebraic Reconstruction Technique algorithms. The application of this approach to data from real situations was also novel. The software for the 3-D projection scheme was designed to allow the flexible use of views from different directions to facilitate it's application to a variety of experimental configurations. It's performance when tested on model data is described, with the results showing the advantage of a direct 3-D reconstruction approach over the conventional 2-D slice approach in the case of limited viewing angles. The conclusion is drawn that a new practical method of extracting full field data from holographic interferograms has been demonstrated. Further, because of it's generality it is applicable to other whole field optical recording systems.

4

1.0 Introduction

The initial aim of this research was to investigate automatic methods for recovering three dimensional data from holographic interferograms, in a form suitable for computer manipulation. This was to be attained by applying tomographic reconstruction methods to data from the holograms, necessitating the development of techniques to circumvent the problem of *restricted view*. This would allow the extremely large amount of three-dimensional data present in the holograms to be fully utilised in a quantitative manner. While investigating this problem it became apparent that the special techniques evolved were of value not only in the area of holographic interferogram interpretation but also in other applications which had limited access to views.

The initial applications for this technology were holographic interferograms of the flow around a turbine blade showing shockwave formation, as well as other flow data. The development of holographic interferometry techniques for gas turbine engine investigation at Rolls Royce has been described by Dr. R. Parker in a series of papers, ref.[34]-[36]. One of these was a manual technique for the extraction of the shockwave position that had been implemented in practice. It was based on a pointer which could be moved in the reconstructed hologram's field of view and then have its position recorded. This allowed a series of points defining the shockwave's position to be mapped. The drawback to this technique was the need for a skilled operator to spend a relatively long time on a monotonous task, thus indicating the necessity to automate the process. The method of tomographic reconstruction was considered as it is particularly

suited to the extraction of three dimensional data from density fields.

Tomographic reconstruction of the particular holographic interferograms Rolls Royce had produced presented a major problem to the researcher as they had an extremely limited angular range of view, while tomographic reconstruction usually relies on a complete set of views around the field being studied. The problem of the limited angle of view present was inherent in the holograms being considered, being dictated by the optical arrangement used to form them. As the views were limited to + 5 or - 5 degrees this was obviously the principle problem to be overcome.

From this starting point a series of technical possibilities were investigated as means to improve the resolution of limited angle tomographic reconstruction. A range of different algorithms were considered and also the effect of a three dimension projection scheme. A number of tomographic algorithms designed specifically for problems involving incomplete or limited angle data had been proposed, and hence it was decided to evaluate the most promising of these experimentally. The possible advantages of a direct three-dimensional projection scheme in contrast to the conventional procedure of reducing a three-dimensional field to a series of two-dimensional slices also merited a full investigation for our application.

After conducting a series of comparative tests on a computer generated test object which confirmed the improved accuracy of the three-dimensional approach, it was decided to use it in preference to the conventional slice technique. While considering the complete field as a whole complicated the calculations required during the tomographic process this allowed the used of rays varying in orthogonal directions leading to improved reconstruction quality.

6

A complete system to collect the data from the holograms and perform the tomography was then constructed, using an IBM compatible PC computer with frame grabber card to capture the images and a Silicon Graphics workstation to process this data.

Once our tomographic system had been successfully demonstrated Rolls Royce requested a modified version of our tomographic software to work with data from neutron studies. After the appropriate modifications had been made to the software some reconstruction of limited viewing angle data from this source were produced. These demonstrated the potential of our novel approach in this area.

2.0 Literature Review

2.1 Introduction

Both holographic interferometry and tomographic reconstruction have a well documented history. This review describes attempts to use these techniques in combination as well as discussing the methods themselves.

The application of tomography to data from holographic interferograms of air flows was successfully demonstrated by Synder and Hesselink in 1984, ref.[87]. In this case the flow around a helicopter blade was studied. The experimental set up used allowed a wide range of views about the flow, an aspect that is a particularly important as will be explained further. Recently interferometric tomography has been applied to flow visualisation of density fields in supersonic jets and convective fields by Soller et al, ref.[88]. Once again these experiments were configured to allow a relatively wide range of viewing angle, (180 degrees in this case). Thus it can be seen from these examples that tomographic interferometry is a well founded technique provided the interferometric data is gathered over a wide range of viewing angles.
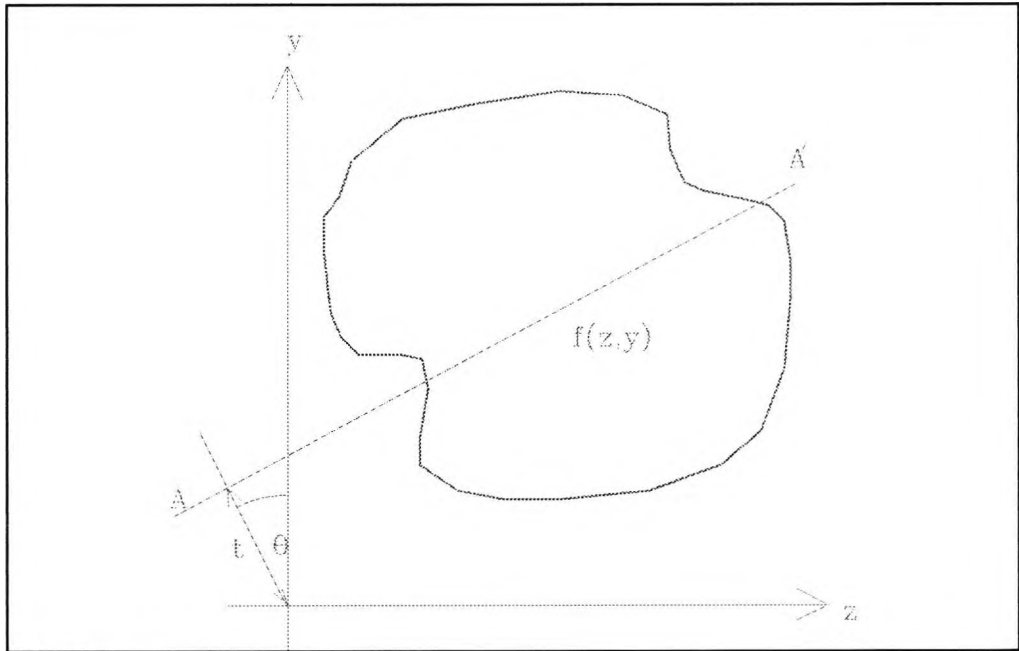
Figure 1

Tomographic reconstruction dates back to the publication of the theory of the Radon transform by Radon ref.1. It is mathematically defined as the inverse of the Radon Transform. The forward Radon Transform is itself defined as the sum of all the line integrals of all possible projections through a field. If we consider the field shown in Figure 1 this can be written as

$$p(t,\omega) = \int_{ray} f(z,y)\,ds \qquad (1)$$

We can express this as

$$p(t,\omega) = \int_{-\infty}^{\infty}\int_{-\infty}^{\infty} f(z,y)\delta(t+z\sin\omega+y\cos\omega)\,dz\,dy$$

$$(2)$$

The inverse of this is given analytically as:

$$f(x,y) = (-1/2\pi^2) \int_{\pi/2}^{\pi/2} d\omega \int_{-\infty}^{\infty} dt P(t,\omega)/(t+zsin\omega-ycos\omega)$$

(3)

This solution assumes an infinite number of ray measurements and of course this is not the case for any practical system, thus *all practical tomography is dealing with an ill-posed problem*. If we consider cases with limited angles of view the reconstruction problem becomes *very* ill-posed with *multiple* solutions for a given set of measurements. The practical solution of the inversion of the Radon transform has been proposed by several different methods, some of which will be discussed later.

Modern interest in tomography stems from the invention of the EMI body scanner, by G.N. Hounsfield, ref.[2], who was awarded the Nobel Prize with A.M. Cormack in 1979 for this work. This invention has stimulated the interest in three dimensional reconstruction which has led to the application of tomography to many other problems. The application of tomographic reconstruction techniques to optical problems has been one area widely investigated and a number of comprehensive reviews published.

The tomographic reconstruction techniques can be divided into two broad groups, transform methods and series expansion methods. These are considered in detail in section 2.0. The transform methods have been comprehensively reviewed by R. Lewitt ref.[94] and the series expansion methods by Y. Censor ref.[2]. Overviews of tomographic processes specifically tailored to limited data, limited angle of view problems have been produced by Hunter ref.[12] and Rangayyan et al, ref.[13]. It is noteworthy that Hunter concluded that the series expansion methods

10

were most suited to limited angle problems, while
noting the sensitivity of the methods of solution to
the particular problem involved. This case sensitivity
was also pointed out by Rangayyan.

2.1.1 Transform Methods

The transform methods are based on analytic
inversion formulae, designed to solve the inverse
radon transform. The principle advantage of this class
of solution in comparison to the series expansion
methods is its speed. The Fourier transform technique
has been widely applied to tomographic problems for
example x-ray imaging. These operate by transforming
projection data into Fourier space thus obtaining some
of the values of the Fourier transform of the complete
field. The mathematics of this method for a weakly
refractive phase object is as follows:

Consider a refractive index field $f(x,y,z)$. The
phase change, ϕ, along the path of a ray, i, as it
passes through the field may be expressed as:

$$\phi_i = \int_{s_i} f(x,y,z) dS_i \qquad (4)$$

If we use the coordinate transform illustrated in
figure 2

$$x = r\sin\theta + \varrho\cos\theta, \qquad (5)$$

$$y = -r\cos\theta + \varrho\sin\theta \qquad (6)$$

11
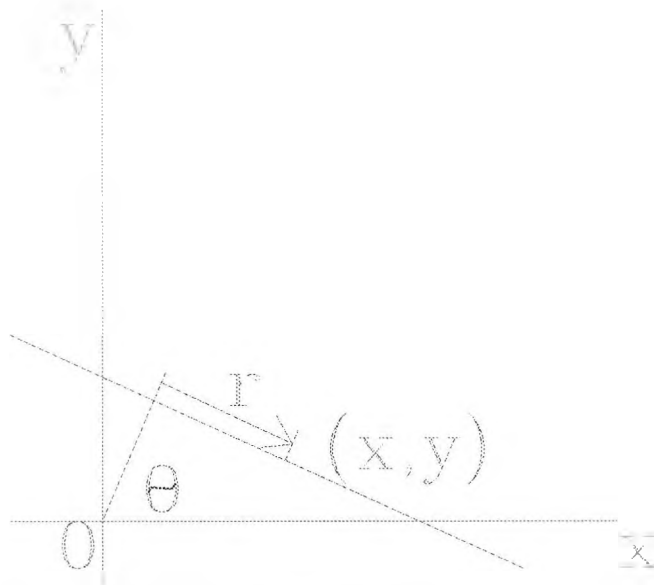
Figure 2 The coordinate transform

we can express the equation as :

$$\phi_i(\varrho,\theta,z)=\int\limits_{\infty}^{-\infty} f(x,y,z)dr \qquad (7)$$

In a 2-D slice reconstruction z will be constant, thus the two-dimensional Fourier transform of equation (above) can be expressed:

$$f(u,v)=\int\limits_{\infty}^{-\infty}\int\limits_{\infty}^{-\infty} f(x,y)\exp[-i2\pi(ux+vy)]dxdy \quad (8)$$

and the inverse transform

$$f(x,y)=\int\limits_{-\infty}^{\infty}\int\limits_{-\infty}^{\infty} F(u,v)\exp[-i2\pi(ux+vy)]dudv \qquad (9)$$

12

If we substitute these expressions into the previous
we have:

$$\phi_i(\varrho,\theta)=\int\limits_{-\infty}^{\infty}\int\limits_{-\infty}^{\infty}\int\limits_{-\infty}^{\infty}F(u,v)\exp\{-i2\pi[r(u\sin\theta-v\cos\theta)+\varrho(u\cos\theta+v\sin\theta)]\}dudvdr$$

(10)

Integrating with respect to r gives a relative
integral part:

$$\int\limits_{-\infty}^{\infty}\exp[i2\pi r(u\sin\theta-v\cos\theta)]dr$$

(11)

When integrating it is apparent, (by the use of De
Moivers theorem), that the solution of the integral is
only non-zero when $u\sin\theta-v\cos\theta=0$, and hence $v=u\tan\theta$.

Substituting into equation 10 we have:

$$\phi_i(\varrho,\theta)=\int\limits_{-\infty}^{\infty}\sec\theta F(u,u\tan\theta)\exp(i2\pi\varrho u/\cos\theta)du$$

(12)

13

The Fourier inverse of the above equation is:

$$f(u, u\tan\theta) = \int_{-\infty}^{\infty} \phi_i(\varrho, \theta)\exp(-i2\pi\varrho u/\cos\theta)d\varrho$$

(13)

From this equation the result know as the Fourier Slice Theorem can be deduce. This may be stated as *the sum of the Fourier transforms of the line integrals through the 2-D field is equivalent to the Fourier transform of the 2-D slice*. Thus a reconstruction process can be based on taking the Fourier transforms of the individual views through a field, summing them to obtain all the Fourier transform of the complete field and performing the inverse Fourier transform to reconstruct the field. This forms the basis of the transform methods of tomographic reconstruction as the field can be deduced from its Fourier transform by taking the inverse transform.

2.1.1 Fourier Reconstruction
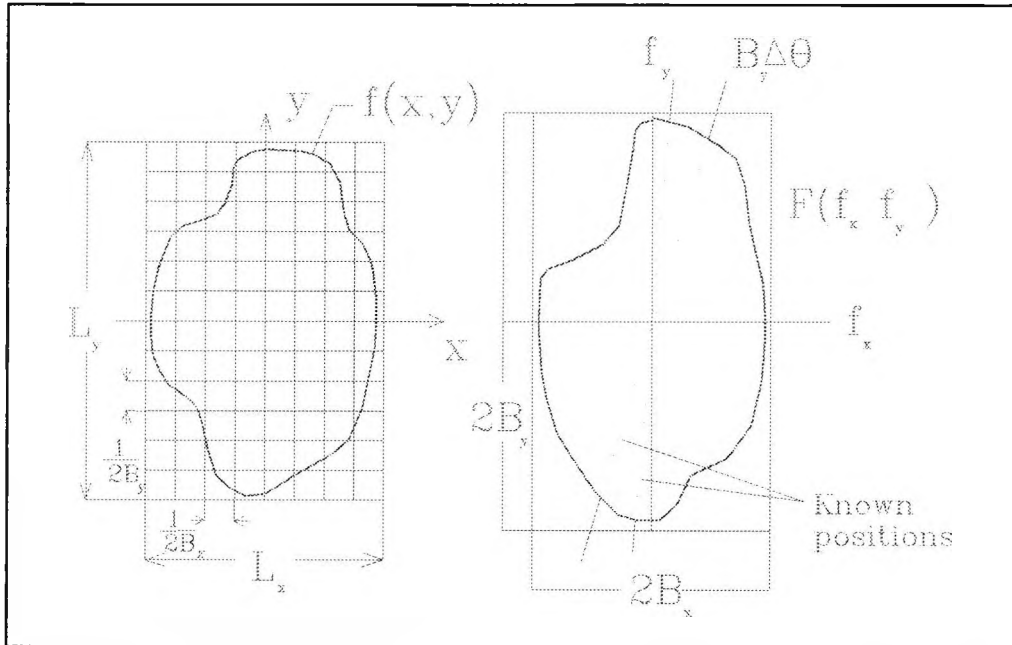
Figure 3 A field and its Fourier space representation

The preceding theorem has to be modified to deal with discrete rather than continuous data and this has been achieved by the following method. Following the derivation used by Sweeney and Vest. We can express the discrete two-dimensional Fourier transform of f(x,y) as:

$$F(\frac{m}{L_x}, \frac{n}{L_y}) = \frac{1}{4B_xB_y}\sum_{t=-\infty}^{+\infty}\sum_{k=-\infty}^{+\infty} f(\frac{l}{2B_x}, \frac{k}{2B_y})\exp[-i2\pi(\frac{ml}{2B_xL_x} + \frac{nk}{2B_xL_y})]$$

(14)

and the discrete two-dimensional transform is:

$$f(\frac{l}{2B_x}, \frac{k}{2B_y}) = \frac{1}{L_x L_y} \sum_{m=-\infty}^{\infty} \sum_{n=-\infty}^{\infty} F(\frac{m}{L_x}, \frac{n}{L_y}) \exp[-i2\pi(\frac{ml}{2B_x l_x} + \frac{nk}{2B_y L_y})]$$

<div align="right">(15)</div>

where L_x and L_y are the spatial limits of the function $f(x,y)$, and B_x and B_y are its bandwidths.
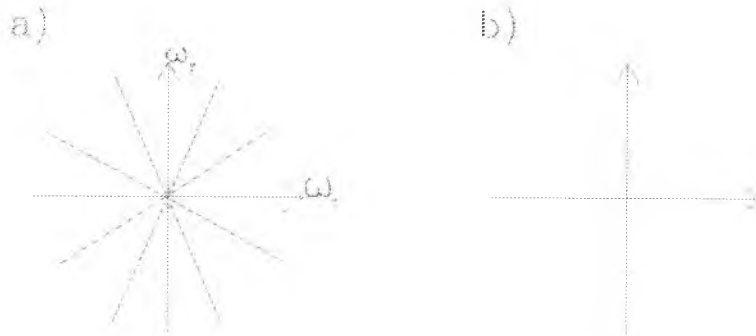
Figure 4 Continuous data (a) and discrete data (b) in the Fourier plane

Continuous data would give radial lines in the Fourier plane, as in figure 4(a). The discrete Fourier inverse can be used to fill out the Fourier plane at sampled points, 4(b). Then using the two-dimensional inverse transform on this the original function, $f(x,y)$, may be extracted. The inverse Fourier transform equation requires data from the Fourier plane over a rectangular array of points. With a well-behaved Fourier transform and sufficient projections it is possible to estimate the required values of $F(\frac{m}{L_x}, \frac{n}{L_x})$ using Fourier domain interpolation. Now these interpolation methods require a well filled frequency plane, as we previously derived $v = u\tan\theta$ and *thus the*

16

*completeness of the spectrum, v, is determined by the
angle of view, θ. This is the key point in rejecting
these methods* for the reconstruction of limited angle
of view problems. As this is the type of problem we
wished to study we did not pursue this method of
reconstruction further.

2.1.2 Series Expansion Methods

Series expansion methods differ fundamentally from
the Fourier transform methods in that they discretise
the field to be solve into a series of elements and
then estimate the values present in each of these
successively. Y. Censor reviewed the finite series
expansion in ref.[1], and discussed the rationale for
using these schemes rather than transform methods. He
concluded that although generating the iterative
solutions is a slower process than using transform
methods they are better able to cope with the
incomplete data sets produced by limited angles of
view, (the prime consideration in our project).

One of the simplest of the series expansion
techniques is the Algebraic Reconstruction Technique,
(ART), ref.[2]. The first EMI scanner in fact used an
algebraic reconstruction technique, although modern
scanners do not use this approach due to its
relatively slow performance in comparison to back
projection. The ART algorithm operates iteratively by
estimating the reconstruction of the field, measuring
the error present, and then updating the estimate to
reduce this error. This algorithm is discussed more
rigorously later in this chapter. The Multiplicative
Algebraic Reconstruction Technique or MART was first
proposed by Gordon, Bender and Herman ref.[2], and
this has been followed by a number of other
formulations of MART type algorithms, by Gordon and
Herman ref.[3], and by Lent ref.[5]. These algorithms

operate in a similar fashion to the ART algorithm, however the error function calculated is used to update the reconstruction estimate by multiplying it with the solution at the previous iteration. Again these are discussed in detail later. This class of solution is widely agreed to be the most suitable for limited angle, limited data problems, (see Verhoven [9]). Hence in consistency with these reviews this is the class of solution that we applied to our problem.

Series expansion methods discretise the reconstruction problem at its start, (in contrast to the transform methods). If we consider the grid of pixels shown in fig. 5 as

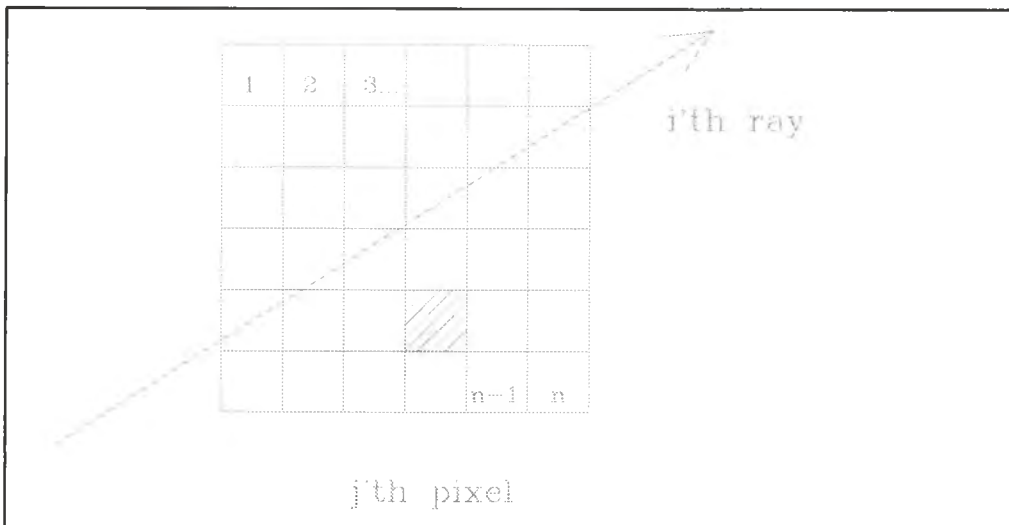**Figure 5** A discretised field

representing the field to be reconstructed with the attenuation in any pixel being uniform within that pixel, the attenuation experienced by a ray passing through this field can be expressed as a function of the distance it has passed through in each pixel along its path. Thus we can express the line integral of attenuation along the rays path as a finite sum as

follows :

$$\sum_{j=1}^{n} x_j \cdot w_{i,j} = y_i, \, i = 1, 2, \ldots, m.$$

(16)

where **w** is the chord length in a pixel crossed by a ray, **y** is the attenuation experienced by the ray, **x** is the attenuation in a pixel, **j** is the pixel number and **i** is the ray number.

Following the description given by Censor, ref.[1], the model can be considered in the following way:

For a set of basis functions

$\{b_j(r,\phi)\}_{j=1}^{n}$, where $b_j(r,\phi) = 1$ if the j'th pixel is crossed or

$b_j(r,\phi) = 0$ if the j'th pixel is not crossed and the digitization of the field is :

$$df(r,\theta) = \sum_{j=1}^{n} x_j b_j(r,\theta)$$

(17)

Where x_j is the attenuation in the j'th pixel. Now if we let $\{R\}_{i=1}^{m}$ be a set of linear and continuous functionals which assign to any picture $f(r,\phi)$ a real number $R_i f$. In this case $R_i f$ is the line integral of $f(r,\phi)$ along the i'th ray. Now y_i is an approximation of $R_i f$ because of the inaccuracy of physical measurements. As R_i is continuous and $\tilde{f}$ is an approximation to f, $R_i f$ is close to $R_i \hat{f}$. Using the linearity of R_i:

$$y_i \approx R_i f \approx R_i \hat{f} = \sum_{j=1}^{n} x_j R_i b_j(r,\phi) = \sum_{j=1}^{n} x_j a_{ij}$$

19

where $a_{i,j}=R_i b_j(r,\theta)$

(19)

The Algebraic Reconstruction Technique, or ART, ref.[29], sets out to solve the problem of the system of equations yielded by discretisation by an iterative process comparing an estimate of the field to the measurements obtained from the field and updating the estimate accordingly. It was discovered independently and applied to image reconstruction by both Gordon et al, ref.[2], and by Hounsfield, ref.[17]. Later it was recognised to be identical to Kaczmarz's algorithm for solving systems of linear equations, [18]. The comparison is between the measured data and the corresponding calculated projection data from the estimated field so that the error is the difference between the two, that is:

$$e=y_i-\sum_{j=1}^{n}a_{ij}x_j^k$$

(20)

where **k** is the number of the current iteration. This error value is then distributed among the pixels along the ray's path.

This leads to the following iterative formula:

$$x^{k+1}=x^k+\sum_j \{y_i-\sum_i^N (w_{i,j}x_{i,j})\}\cdot w_{i,j}/(\sum_i^N w_{ij})^2\}$$

(21)

The formula is applied to each pixel, (or voxel), passed through by a given ray and subsequently to all

other rays in each view in turn.

Modified versions of the ART algorithm have been produced, namely the Averaging Algebraic Reconstruction Technique AVART, ref.[88] and the Approximate Algebraic Reconstruction Technique, AART for limited data problems. The results produced by these have been as yet inconclusive however they are mentioned here as forming subjects for possible further study.

As well as the ART algorithm the MART (Multiplicative Algebraic Reconstruction Technique) algorithms were considered during our trials. There are several different MART algorithms the first of which was proposed by Gordon, Bender and Herman, see [2]. Like the ART algorithms the MART algorithms are iterative methods of solution and as the name suggests they update the preceding estimation by multiplying by an update function. The update function developed was:

$$X^n = X^{n-1} \cdot [R_j / \sum_i^N (w_i \cdot x_i^{n-1})]$$

(21)

where R_j is the measured ray sum, w_{ij} is the chord length of ray R_j in element x_i, X is the elements attenuation and n is the number of iterations. This algorithm was applied to a projection matrix which had only zero or one as possible values.

A modified version of this algorithm was published by Gordon and Herman, ref.[3], which made the update factor proportional to the chord length of the ray present in the element being updated. This is given below.

$$X^n = X^{n-1} \cdot w_{ij} [r_j / \sum_i^n (w_{ij} x_i)]$$

It was this version of the Gordon and Herman MART algorithm which was selected for testing as our projection scheme generated variable chord lengths in individual voxels and hence required algorithms which could cope with this, (the alternative of modifying the projection scheme so that only rays which passed through the centres of elements were considered would have resulted in the rejection of large amounts available data which would have been undesirable). In fact the algorithm finally applied had a slight modification to ensure convergence with our data, the addition of a relaxation factor as suggested by Verhoeven, ref.[4]. This gave the following algorithm:

$$X^n = X^{n-1} \cdot (1 - \lambda(w_{ij}/w_{max}) \cdot [1 - R_j / \sum_i^n w_{ij} x_i])$$

(23)

Where λ is the relaxation factor.

As well applying this algorithm we also considered the MART algorithm produced by Lent ref.[5]. This algorithm has the interesting property of converging to the *maximum entropy solution*, under the appropriate conditions. Maximum entropy tomographic reconstruction has been proposed for several ill-posed problems and is described in detail in section 2.1.4.

2.1.3 Three dimensional projection schemes for use with series expansion techniques

There have been several investigations into direct three-dimensional tomographic reconstruction, where the 3-D field is not decomposed into 2-D elements, using both transform and iterative reconstruction methods, refs.[14]-[16],[60],[76] and [78].

As described previously all iterative

reconstructions methods consider the field to be reconstructed in a discrete form, e.g. as a series of stacked slices composed of 2-D elements. This has a direct effect on the directions from which the data can be gathered for use in the tomography process where a three-dimensional field is decomposed into a series of pixel elements contained in stacked two-dimensional slices, data can only be collected in the plane of these slices. Previous investigations by Colsher, ref.[14], and Schlindwein, ref.[15], and Altshuler ref.[16], into the effect of the directions that the data is allowed to take has indicated that this can have a significant effect on reconstruction accuracy in limited angle tomography, (also ref. 60).

In Colsher's paper he describes applying iterative reconstruction techniques to a projection scheme which was not co-axial for the first time, fig. 6.
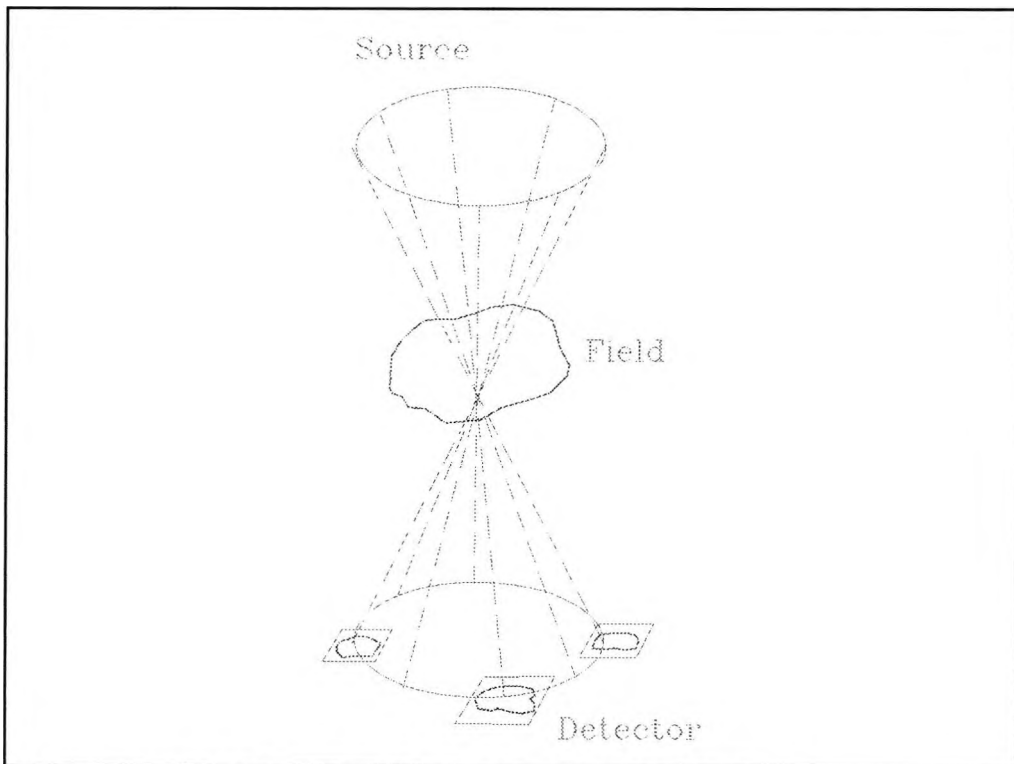

Figure 6 Colsher Conical Projection Scheme.

Colsher defined an allowed set of projection for a given view in order to minimise the complexity of the three-dimension calculations required, having recognised this as the major drawback of the technique. It should be noted however that at the time his work was published, 1977, the computational power available was far more limited than today.

The iterative algorithms implemented by Colsher were the ART, SIRT, and ILST (Iterative Least Squares Technique). Their performance was evaluated by using them to reconstruct computer generated data, and a comparison of 2-D and 3-D reconstruction was made. The error measurement used to compare the reconstructions was defined as follows:

$$\delta(q) = [\sum_i \sum_j \sum_k (D^q(i,j,k) - T(i,j,k))^2 / \sum_i \sum_j \sum_k (T(i,j,k) - \bar{T})^2]^{\frac{1}{2}}$$

(24)

This is the discrepancy as defined by a normalised Euclidian function, where D^q is the reconstruction density at iteration q, T is the density of the test image, and $\bar{T}$ is the mean density of the test image. Reconstructions were then performed on two sets of test data, one of shell surrounded spheres and another of multiple spheres. The discrepancy figures produced comparing the linear and circular projections are given in table 1.

24

Table 1. Discrepancy for linear and circular geometries.

Geometry	Shell-surrounded spheres	Multiple spheres
Linear	0.77	0.75
Circular	0.61	0.65

These values were for 15 iterations of SIRT.

In both cases the circular projection scheme gave lower discrepancy figures. From this Colsher concluded that *direct 3-D reconstruction is superior to serial 2-D reconstructions from co-axial projections when the viewing angle is limited*, a highly significant comment for our later work on this principle.

Schlindwein followed Colsher's general approach and applied a twin-cone beam geometry to x-ray reconstruction, using the ART algorithm. However unlike Closher's limited angle study the projections used formed complete continuous data set. Again he concluded that a 3-D approach was superior to a 2-D projection method. These results persuaded us that a fuller investigation of the 3-D technique was essential, despite the increased complexity.

The drawback to direct three-dimensional reconstruction is the increased number of the calculations required in comparison to the two-dimensional slice approach. Indeed as recently as 1991 Rizo et al, ref.[78], rejects algebraic algorithms for use with three-dimensional cone beam reconstruction because "*they are much too time consuming, even with up-to date technology*". However as the speed of digital computers continues to increase rapidly with the passage of time the problem of increased run time

with this approach would becomes less important over
the three year life time of this project. In fact in
1994 Soller et al, ref.[88] stated their intention to
implement a direct three-dimensional reconstruction
with an iterative reconstruction algorithm to study
holographic interferograms, that is, they decided to
follow the same course as our work.

2.1.4 Maximum Entropy Reconstruction

The application of the theory of Maximum Entropy to
tomographic reconstruction problems is an area which
has stimulated much interest, refs.[7], [10]-[11], and
[26]-[28]. The MART algorithm as described by Lent has
been shown to converge to the maximum entropy solution
under certain conditions and the MENT algorithm by
Gimeno is specifically designed to converge to it,
ref.[10]. The theory of maximum entropy tomographic
reconstruction is described by Newton & Gull in
ref.[7]. The basis of maximum entropy tomography is
the selection of the solution to a tomographic
problem which has the greatest configurational
entropy from the set of possible solutions. The
configuration entropy is defined as:

$$S = -\Sigma p_i \log p_i / m_i$$

(25)

where p_i is the value present in the i'th element of
the field, (for our purposes this corresponds to the
attenuation in a voxel) and m_i is the initial estimate
of intensity in the i'th element. By maximising this
function the resultant reconstruction is the solution
bearing the least information while being consistent
with the measured data. It is argued that this was the
most desirable selection as it reduced the likelihood

26

of generating spurious artifacts in the reconstruction, however it should be noted that an algorithm giving some other consistent solution might in fact arrive at a more accurate reconstruction. The implementation of the maximum entropy solution has been proposed by Lent using a MART type algorithm ref.[5], by Minerbo with a constrained optimation algorithm, the MENT algorithm, ref.[10], and Frieden and Zoltani ref.[11].

The form of the algorithm is as follows:

$$X^n = X^{n-1} \cdot [R_j / \sum_i^n w_{ij} X_i]^{\lambda w_{ij}}$$

(26)

The conditions for this algorithm to converge to the maximum entropy solution are:
1) The system of equations must have a solution.
2) The solution must be non-negative.
3) The elements in the chord length matrix, (w_{ij}), must be less than or equal to one.

It is the first of these requirements which is of possible difficulty in a real situation where measurement errors might result in an inconsistent set of equations defining the field. The operation of this equation under real conditions would thus have to be observed.

2.1.5 Complimentary Field Reconstruction

Another reconstruction technique of interest is the Complimentary Field Method recently proposed by S.Cha and H. Sun, ref.[6]. Although iterative in nature it follows a different principle to the ART and MART algorithms and is thus considered here separately. The

principle behind its operation is the reconstruction of a complementary field which is the difference between the field to be reconstructed and the estimation of this field. This is done in order to allow the easy incorporation of "a priori" information, an aim previously considered by Medoff et al, ref.[86], in their iterative convolution backprojection algorithm which also introduced an intermediate step to the reconstruction process. In a CFM reconstruction process this principle is applied as follows:

1) Make an initial estimate of the object field.

2) Calculate the projection data from this estimate which corresponds to the measured data available.

3) Take the difference between the measured projection data and the calculated projection data from the estimate, to give the projection data of the complementary field.

4) Reconstruct the complementary field. At this stage the projection data may be augmented by any prior constraints.

5) Update the estimate of the object being reconstructed by adding the complementary field to the previous estimated field.

This process is continued until the desired termination criteria are reached. It should be noted that the reconstruction of the complementary field may be performed by any number of tomographic processes, (Cha and Sun using convolution backprojection in their initial tests).

The advantages of this technique are its suitability

when applied to ill-posed problems and the ease of incorporation of "a priori" information. The C.F.M. also produces a stable convergent solution, with the complementary field tending to zero with increasing iterations. Its suitability for incomplete data set reconstruction stems from the ease of incorporating prior information into the reconstruction process, thereby compensating for the missing information. This "a priori" information can be introduced at step (1) and any known constraints may also be considered at step (4).

A subsequent modification to this technique by Zhang and Ruff ref.[8] has made it more suited to the problem of processing data from holographic interferograms. They considered the problem of fringe ordering for holograms of practical fields where a zero order fringe was not available due to limitations in viewing and produced the Modified Complimentary Field Method to overcome this. This is described in detail in section 2.2.5 on tomographic techniques specifically developed for use with holographic interferograms.

Our implementation of the CFM combined the process with an iterative algorithm to generate the difference field, unlike the version demonstrated by Cha et al which relied on a convolution back projection. Some tests were performed with dummy data but as a priori data was not available for practical data sets a full evaluation of this technique was not possible.

2.1.6 Maximum A Posteriori

Another approach to tomographic reconstruction problems has been considered by Watt, ref.21, Hansen, ref. 22, Smith et al, ref. 23, and Geman and Geman, ref. 24. Rather than using know facts about the field as *a priori* information this data is used in an *a*

posteriori reconstruction technique. In this type of solution in addition to physical constraints, for example non-negativity of the solution, the statistics of the source function and measurement noise may be incorporated into the reconstruction. If the statistics of these are know the reconstruction produced is called the Maximum *A Posteriori* (MAP) solution. The MAP solution can be generated by linear methods or by relaxation techniques, (e.g. simulated annealing). The advantage of this technique, especially from fluid flow studies, is that data from point measurements can be used to generate statistical information about fields.

2.1.7 Neural network tomography

A recent a novel approach for solving tomographic problems in aerodynamic studies with neural networks has been demonstrated by Decker, ref. [33], as well as being applied to some other tomographic problems ref. [57] and ref. [58]. Neural networks "learn" to solve tomographic problems by making estimates of reconstructed fields from the projection data of know fields. These estimates are then corrected in the so called training process. The neural networks guess is improved until it can obtain a relatively accurate reconstruction estimate of the known fields. Hopefully when a trained network is used to reconstruct an unknown field it will produce an accurate reconstruction. This technique is in an early stage of development, as neural networks are still an emerging field of study, and as yet unproven.

2.2 Holographic interferometry

2.2.1 Holography

Holography was invented by Gabor, ref.[30] in 1948. His work on improving the quality of electron microscopes led him to propose a technique he called wavefront reconstruction, in which the phases as well as the intensities of a wavefront are recorded so that they may be reproduced later. This basic principle has come to be known as holography. In optical holography this is achieved by combining the information bearing light which we want to store with a reference beam. Provided these two are coherent they will interfere and this interference pattern can be captured on a photographic medium. The coherence condition can be achieved by using light from a laser source and this was proposed by Leith and Upatnieks, ref.[31]-[32] along with practical layouts for optical holography. The off-axis holography they developed is the type which interests us as it is used to produce the holographic interferograms which we wish to study. The term off-axis comes from the fact that the image and object beams follow separate paths, with the reference beam passing off the axis of the object beam and propagating in a different angular direction. This causes the waves produced by diffraction in the reconstruction process to be spatially separate, an advantage over the Gabor type holograms where overlapping causes a noisy low-contrast image.

The theory of off axis hologram formation can be expressed as below, (following the derivation of Vest, ref.[40]):

At the film plate where the hologram is recorded the object wave's complex amplitude is:

$$U_0(x,y) = a_0(x,y)\exp[-i\phi_0(x,y)]$$

(27)

and the reference wave is:

$$U_R(x,y) = a_R\exp(i2\pi f_y y)$$

(28)

where $f_y = \sin\theta_R/\lambda$ is the spatial frequency of the reference wave. Thus the irradiance will be

$$I(x,y) = |U_0 + a_R\exp(i2\pi f_y y)|^2$$

(29)

$$I(x,y) = |U_0|^2 + a^2{}_R + a_R U_0\exp(-i2\pi f_y y) + a_R U^*{}_0\exp(i2\pi f_y y)$$

(30)

A film exposed to this irradiance pattern and developed would have an amplitude transmittance given by :

$$t(x,y) = t_b + \beta[|U_0|^2 + a_R U_0\exp(-i2\pi f_y y) + a_R U_0^*\exp(i2\pi f_y y)]$$

(31)

If we now substitute for U_0 and combine the exponential terms:

32

$$t(x,y) = t_b + \beta a_0^2(x,y) + 2\beta a_R a_0 \cos[2\pi f_y y - \phi(x,y)]$$

(32)

From this equation we can deduce that the holograms contain carrier fringes of spatial frequency f_y which are modulated in amplitude by $a_0(x,y)$ and in phase by $\phi(x,y)$.

When the hologram is reconstructed, by illuminating it with a plane wave, given by $U_c(x,y) = a_c \exp(i2\pi f_y y)$, in the same direction as the original reference beam, the resultant transmission is given by:

$$U_I(x,y) = (t_b + \beta|U_0|^2)a_c\exp(i2\pi f_y y) + \beta a_c a_R U_0 + \beta a_c a_R U_0^* \exp(i4\pi f_y y)$$

(33)

Examining the right hand side of above equation terms by term we have; the first term gives a transmission wave through the hologram, attenuated and modulated in irradiance, the second gives a diffraction wave which is identical to the original object wave, the third gives a wave which is the conjugate of the original object wave. These two terms can each give a reconstruction of the object, however as the conjugate wave propagates at an angle $-\sin^{-1}(2\theta)$ to the z-axis diffraction effects in the hologram recording medium usually suppress the conjugate wave. Thus usually only the transmitted wave and the object wave are obtained on reconstruction. This is the basis of the off-axis holographic process that is used, in modified form, to produce the holographic interferograms which we wished to study.

2.2.2 Holographic Interferometry

Holographic interferometry is the comparison of two or more waves, at least one of which is a hologram, by interferometry. It was first suggested in 1965 by Horman, ref. [41], in a scheme where a hologram would be used in place of a test section in a Mach-Zehnder interferometer. Powell and Stetson described the application of holographic interferometry to vibration studies, ref. [42], also in 1965, and double exposure and real time holography were reported later that year, refs. [43]-[47].

In double exposure holographic interferometry a holographic plate, (or other recording medium), is subjected to more than one exposure and the developed. This results in the formation of fringes where there has been a change in the wavefront arriving on the plate between exposures. For example a holographic interferogram of a solid surface experiencing bending between the two exposures would show fringes where the surface had been displaced. Mathematically the process can be described as follows.

If two holographic exposures $U_1(x,y)$ and $U_2(x,y)$ are made, at times t_1 and t_2 with the same reference beam $U_R(x,y)$, when the hologram containing this information is reconstructed it's complex amplitude will be proportional to:

$$[U_1(x,y) + U_2(x,y)]$$

(34)

and it's irradiance will be proportional to:

$$I(x,y) = |U_1(x,y) + U_2(x,y)|^2$$

(35)

34

Now as both exposures will be of the same object with a small change which will mainly effect the phase of the second exposure, we can express $U_1(x,y)$ and $U_2(x,y)$ as $a(x,y)\exp[-i\phi(x,y)]$ and $a(x,y)\exp\{-i[\phi(x,y) + \Delta\phi(x,y)]\}$ respectively. Substituting these into the irradiance expression we have:

$$I(x,y) = |a(x,y)\exp[-i\phi(x,y)] + a(x,y)\exp\{-i[\phi(x,y) + \Delta\phi(x,y)]\}|^2$$

(36)

$$= 2a^2(x,y)\{1 + \cos[\Delta\phi(x,y)]\}$$

(37)

Examining this equation it is apparent that the fringe pattern is produced by the $\{1 + \cos[\Delta\phi(x,y)]\}$ term modulating the irradiance. Thus bright fringes are formed where $\Delta\phi$ is $0, 2\pi, 4\pi, ..n\pi$, where n is an even integer, and dark fringes where $\Delta\phi = \pi, 3\pi, 5\pi, ...(n+1)\pi$. Hence by examining a fringe pattern physical changes in the object producing phase changes in the object beam between the exposures can be detected.

2.2.2.1 Holographic Interferograms of Transparent Objects

Holographic interferograms of transparent, (or phase), objects may be formed giving a valuable means of viewing refractive index variations in these fields.

The refractive index of a medium governs the speed of propagation of light through a field, defined by :

$$n = c_0 / c$$

<div align="right">(38)</div>

where c_0 is the speed of light in free space.

The *optical pathlength* of a ray through a medium is dependent on the refractive index as :

$$\Phi = \int n \, ds$$

<div align="right">(39)</div>

If the refraction of the ray on passing through a medium is negligible, (it should be noted this is not usually the case), the path can be made parallel to the z axis and hence we can rewrite the equation as:

$$\Phi(x, y) = \int n(x, y, z) \, dz$$

<div align="right">(40)</div>

Transparent objects with negligible refraction are referred to as *phase objects*. The formation of a holographic interferogram in a phase object can be mathematically described as follows:

If we consider two exposures of a holographic recording material with differing field refractive index distributions, (Φ_1, Φ_2), for each exposure the two holograms formed upon reconstruction can be expressed as:

$$U_{o1} = a_1(x, y) \exp\left[i \frac{2\pi}{\lambda} \Phi_1(x, y)\right]$$

<div align="right">(41)</div>

and

$$U_{o2} = a_2(x,y)\exp[i\frac{2\pi}{\lambda}\Phi_2(x,y)]$$

(42)

The irradiance sum of these holograms when they are reconstructed simultaneously in the image plane gives the fringe pattern. Assuming a_1 and a_2 are uniform unit amplitudes the irradiance can expressed as follows:

$$I(x,y) = 2\{1+\cos\frac{2\pi}{\lambda}[\Phi_2(x,y)-\Phi_1(x,y)]\}$$

(43)

In applications where the initial field is where one exposure is uniform, (e.g. the first exposure taken with a null field), this can be re-expressed as:

$$I(x,y) = 2[1+\cos(\frac{2\pi}{\lambda}\Delta\Phi(x,y))]$$

(44)

where

$$\Delta\Phi(x,y) = \int[n(x,y,z)-n_0]dz$$

(45)

The equation of a bright fringe can now be expressed as:

$$\Delta\Phi(x,y) = \int[n(x,y,z)-n_0]dz = N\lambda$$

(46)

37

Where **N** is an integer.

For the formation of dark fringes the same equation with values of **N** = 0.5, 1.5, 2.5, and so on.

The optical path difference at any point can be expressed :

$$\Delta\Phi = N\lambda$$

(47)

2.2.3 Fringe Interpretation in Practical Measurements

The preceding derivation illustrates how the fringes apparent in phase object holographic interferograms of are formed, and this principle has been applied to many aerodynamic studies,(for example, Heflinger ref.[37], Chau and Mullaney ref.[38], and Wuerker et al ref.[39]). The use of holographic interferograms and the fringe processing techniques required to handle their data for use with tomographic reconstruction techniques has been reviewed by Trolinger and Hsu in ref.[20]. In handling data from such experiments the principle problem is how to convert the fringe data into density information.
The density of a gas is related to it's refractive index by the *Gladstone-Dale* equation:

$$n - 1 = K\rho$$

(48)

Where **K** is a property of the gas called the Gladstone-Dale constant. Its value is slightly affected by the wavelength of the light propagating through the gas and almost independent of temperature and pressure.

For a simple case where the refractive index variation through the field can be expressed as $f(r) = n(r) - n_o$, with n_o being the ambient refractive

38

index, the density distribution would be

$$\rho(r) = \rho_o + \frac{f(r)}{K}$$

<div align="right">(49)</div>

where ρ_o is the ambient density.

In terms of fringe order **N** we can then write:

$$N(x,y) = \frac{K}{\lambda}L \,\Delta\rho \,(x,y)$$

<div align="right">(50)</div>

where **L** is the path length of a ray. From this it can be seen that the density change $\Delta\rho$ at a point gives a change at the corresponding point in the image plane hologram. In a normal double exposure hologram this gives rise to a map of the absolute change between ambient and flow conditions, and in rapid double exposure holograms it gives a map of the local rate of density change.

2.2.4 The Rolls Royce Compressor Fan Holograms

Holographic interferograms for use in compressor flow visualisation have been extensively investigated and developed for research purposes at Roll Royce plc. The work and facilities are described in a series of papers by Parker et al, refs.[34]-[36] and also by others, refs.[49]-[52]. The specific hologram type that the development of our tomographic system was geared to was that used for shockwave location in the front fan of gas turbine engines. In this type of rotating transonic flow field the rotation of the flow field relative to the optical equipment provides a time-varying phase field superimposed on the light transmitted through the field.

<div align="right">39</div>

Considering the equations for a rotating flow field case, (i.e. the compressor fan of a gas turbine engine), the phase change produced is:

$$\Delta\theta = \frac{2\pi K}{\lambda}\int[\rho(R,\theta,z) - \rho(R,\theta + \omega\Delta t,z)]dr$$

(51)

where (R,θ,z) are the circular coordinates with R being the axis parallel to the blades directions, z parallel to the shaft of the engine and θ is the angular rotation about the shaft, ω is the angular velocity, λ is the wavelength of light.

For a shock causing a step density change $\Delta\rho$ at a position (R, θ, z), with no other significant density gradient along the viewing direction, the fringe order at that point can be expressed as:

$$N = \frac{C \Delta\rho R \omega \Delta t}{\lambda \cos(\alpha)}$$

(52)

where α is the angle between the normal to the shock surface and the viewing direction.

This type of investigation was first undertaken by Wuerker, ref.[39], with a direct transmission optical system which required two large windows having a direct line of sight on opposite sides of the fan. The results of this approach suffered from poor feature localisation in the transmission field. A different optical arrangement was adopted by Rolls-Royce using a reflecting system. This is shown in the fig.7.
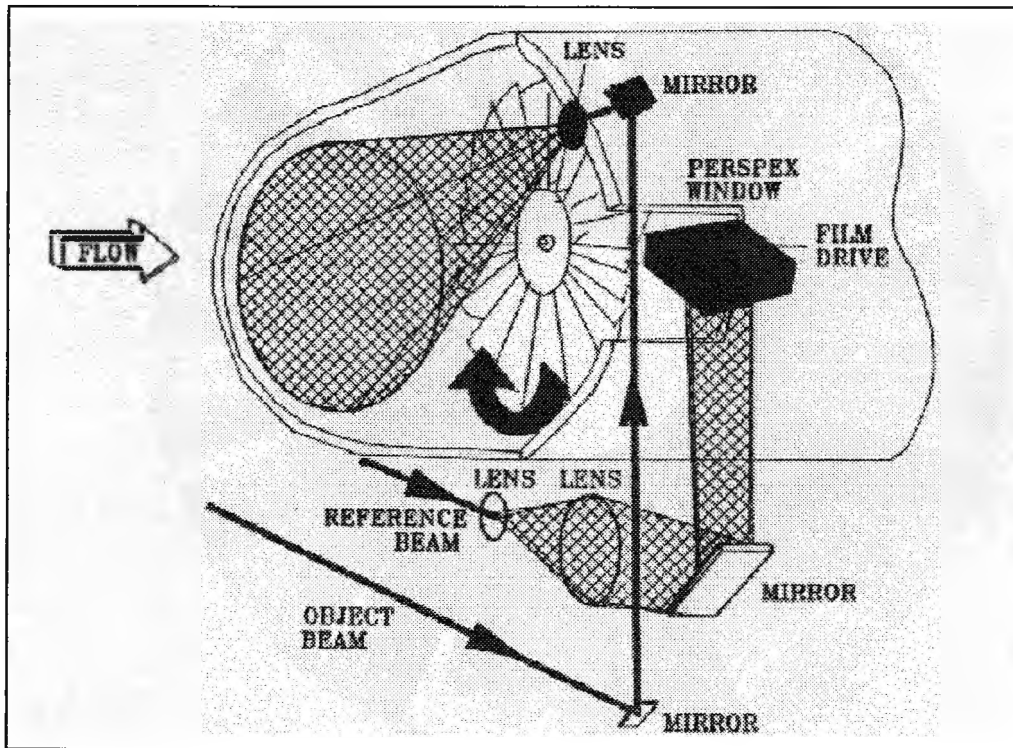
Figure 7 The Rolls Royce optical configuration

The system used a bright diffuse surface to reflect the light, the diffuse nature of the background giving multiple optical paths in the reflected beam. These multiple paths gave an enhanced three dimensionality to the holographic image, making possible the accurate measurement of the position of shocks and other flow features. The laser source used to produce the holograms was a double-pulsed ruby laser. These pulses freeze the rotation of the fan in each exposure, as well as providing the two exposures to form the interferogram. The object beam enters upstream of the fan and is reflected by the far wall of the compressor casing, this surface having been prepared with a highly reflecting diffusing coating. This beam then exits through a window, in the casing over the blade tips, to the holographic film where it combines with the reference beam.

In the resultant holograms the blades appeared as

41

3-D silhouettes against a bright background. Short
pulse separation ensures that the movement of the
blades between the two exposures is small, 1-3μs
giving 0.5-1.5mm movement at the tips. The change in
density during the two pulses causes the fringe
pattern seen in the hologram and is effected by the
rotation of the strong density gradients present in
the field. The greatest effect is seen for shockwaves
where a pressure discontinuity is displaced, this
causing a dark fringe to localise on the shock. As
explained in the section 2.0 it was the location of
flow features in this type of hologram which provided
the initial stimulus for this project.

2.2.5 Tomographic Methods Developed Specifically for use with Holographic Interferograms

Tomographic methods designed specifically for use
with data from holographic interferograms have been
published, usually to circumvent one of the principle
problems associated with the technique.

2.2.5.1 Ray Bending

Cha and Vest, [48], have considered the problem of
ray bending in strongly refracting fields. As the
light rays recording a holographic interferogram
passes through a refracting field not only do they
experience a phase change due to refractive index
variations but also undergo bending. If the refraction
is great enough to produce significant ray bending,
then when the hologram inteferogram's data is
reconstructed by tomographic methods errors can be
made. This is because the assumption is usually made
that straight probing rays propagate through the
field. Cha and Vests method of overcoming this was to
include an iterative loop in the reconstruction
process where the amount of ray-bending produce by the

field was estimated. The field was then updated using these new ray-paths in the reconstruction. The process is repeated until the field changes converge.

Mathematically the iterative process is as follows: A deviation function is given by

$$D(\rho,\theta) = \Delta\Phi_M(\rho,\theta) - \Delta\Phi_F(\rho,\theta)$$

(53)

where $\Delta\Phi_M(\rho,\theta)$ is the measured data from the fringe pattern and $\Delta\Phi_F(\rho,\theta)$ is the refractive index data that would be apparent without ray bending in the field.

If an initial estimate is made of the deviation function we can write the initial estimate of the line integral transfer of the field as :

$$\Delta\Phi_{F(i)}(\rho,\theta) = \Delta\Phi_M(\rho,\theta) - D_{(i)}(\rho,\theta)$$

(54)

Where **i** is the iteration number, and is zero for this first estimate.

Reconstructing the approximate field from the "bent" ray data:

$$n_i(r,\phi) - n_0 = IR(\Delta\Phi_i)$$

(55)

where **IR** is the inverse radon transform.

Now using computational ray tracing the path length transform of this estimate can be calculated as:

$$\Delta\Phi_{M(i)}(\rho,\theta) = PT[n_i(r,\phi)]$$

where **PT** is the pathlength transform.

An updated estimate of the deviation function can now be made:

$$D_i(\rho,\theta) = \Delta\Phi_{M(i)} - \Delta\Phi_{F(i)}$$

This process is then repeated using this updated deviation function until some predetermined convergence criterion is met, (e.g. the difference between two successive reconstructed fields is sufficiently small).

2.2.5.2 Unknown Fringe Order

Zhang and Ruff considered the problem of fringe ordering for holograms of practical fields where a zero order fringe was not available due to limitations in viewing. They produced the Modified Complementary Field Method, section 2.1.5, to overcome this. The MCFM process is as follows:

Steps (1) and (2) are as for the CFM.

(3) As no zero order reference fringe is available the assigned fringe number is shifted by N_s, where N_s is a function of the viewing angle θ. Thus:

$$g(\rho,\theta) = [\overline{N}(\rho,\theta) + N_s(\theta)]\lambda/2$$

where λ is the wavelength of the reconstructing light, and **N** is an odd integer for dark fringes and an even integer for bright fringes. Now as **N** cannot be determined where a zero fringe is not visible the

expression can be rewritten in terms of relative fringe number as:

$$\overline{g}(\rho,\theta) = N(\rho,\theta)\lambda/2 \qquad (59)$$

Using the projection data and the measured fringe data, $\overline{N}$, N_s may be calculate for the i'th ray using:

$$N_{s,i} = [2g_e(\rho_i,\theta_i)/\lambda] - \overline{N}_t$$

$$(60)$$

The value of N_s must be the same must be identical for each set of data from a single view. Now as only an estimated field is used to obtain $g_e(\rho_i,\theta_i)$ the values of $N_{s,i}$ will vary over a relatively large range, hence an average phase shift is calculated for each set of data from a single view. At this point Zhang and Ruff introduced the expression below to calculate the average phase shift:

$$N_s = \{\frac{1}{n}\sum_{i=1}^{n} N_{s,i}\}\beta$$

$$(61)$$

Where n is the total number of optical rays evaluated and β is the phase-shift control number defined as :

$$\beta = abs(\sum_{i=1}^{n} N_{s,i})/\sum_{i=1}^{n} abs(N_{s,i})$$

$$(62)$$

A simple algebraic average of the phase difference between measured and estimated field could not be used because it does not yield consistent values for N_s, especially on the first step of the iteration. In

contrast Zhang and Ruff's method is designed to give a consistent progression toward a convergent solution, (it should be noted that other averaging schemes could also be used, a point made by the authors). The parameter β takes a value of one if the $N_{s,j}$ are either all positive or negative. For the case where some $N_{s,i}$ are positive and others negative, (i.e. if the initial estimate is poor and toward the end of a iteration), the value of β tends toward zero, with a smaller fraction of the phase shift being applied.

(6) The average value of N_s is added to the measured data to form $g_e(\rho,\theta)$ as follows:

$$g(\rho,\theta)=(N_s+\overline{N})\lambda/2$$

(63)

The following steps in the MCFM are the same as in the original CFM.

(7) Determine the difference between the projection data and the estimated field, to give the projection data for the complementary field:

$$g_c(\rho,\theta)=g(\rho,\theta)-g_e(\rho,\theta)$$

(64)

(8) The complementary field is then reconstructed:

$$f_c(x,y)=R\{g_c(\rho,\theta)\}$$

(65)

Where **R** is the reconstruction operator.

(9) The complimentary field is then used to update the object field estimate,

$$f_r(x,y) = f_e(x,y) + \alpha f_c(x,y)$$

<div align="right">

(66)

</div>

where α is a relaxation factor to prevent the solution overshooting.

(10) Any "a priori" constraints are now applied to the solution and the process is returned to step 2 using the reconstruction as the starting estimate.

The significance of this approach is its ability to handle data from situations where the views of a field are partially obscured. This leads to only relative fringe data being available and is the case in many practical situations. For instance in wind tunnels the view of an air flow is obscured by the tunnel walls.

3.0 The implementation of a direct three dimensional projection scheme

As we have seen conventional tomographic schemes simplify the reconstruction problem by considering the three dimensional field as a series of two dimensional slices stacked on top of each other. Then solutions are made for each slice, fig. 8.
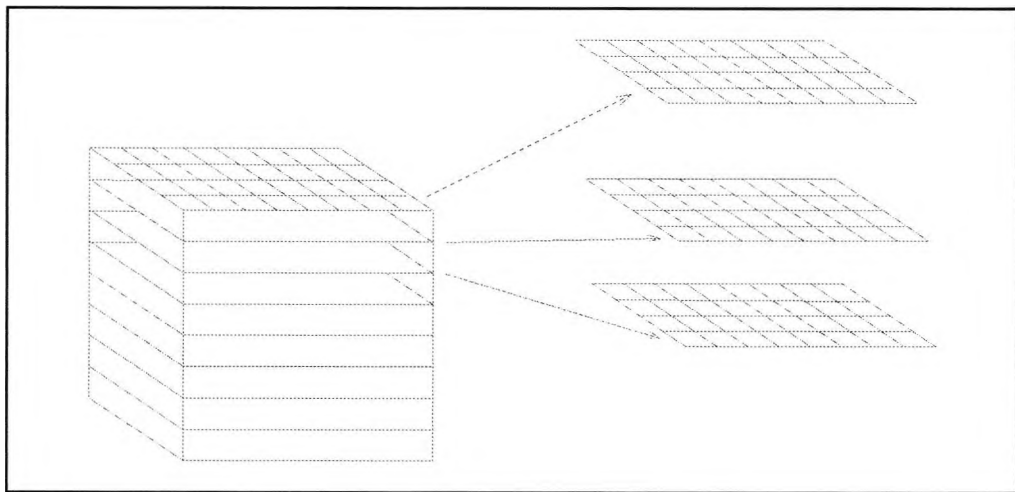
Figure 8 Decomposing a 3-D field into 2-D slices.

While this greatly reduces the amount of calculation required it limits the usable data to that collected in the plane of the slices. This rejection of out of plane data does not present a serious problem when the field to be reconstructed can be viewed about 360 degrees, (or close to a full field of view), However for where views, (and thus available data), are severely limited it is desirable to maximise the utilisation of data. Thus it was decided to investigate the effect of using a direct three dimension reconstruction algorithm. Previous work by J.G. Colsher, ref. [14], had demonstrated this principle using a *cone of views* in the reconstruction of model data. To test the feasibility of this method for our case a completely new computer program had to

49

be written to perform the direct reconstruction, as no three dimension reconstruction software of this type was available.

In a direct three dimensional reconstruction program the generation of the geometric data required by the algorithm is a much more involved problem than in the slice methods. The iterative reconstruction algorithms require the chord length of each ray in every voxel, as it passes through and thus the rays must be traced through a three dimension field and each individual length calculated. The geometry chosen to reconstruct the field with was a cube which was decomposed into cubic volume elements, this lending itself to the generally rectangular volumes being reconstructed, fig.9.
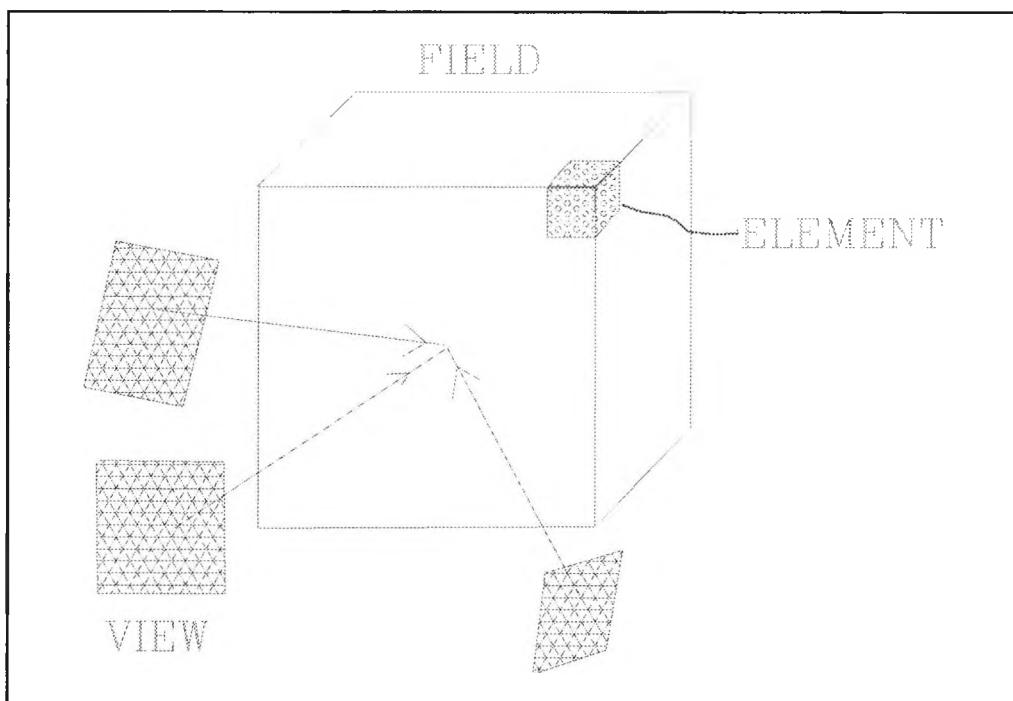
Figure 9 Views about the 3-D field.

Views are taken facing into one side of the field

and the direction of these views are varied in the vertical and horizontal axes. The parameters of the rays passing through the field are calculated as follows :

The initial position and direction of a ray can be defined relative to the field by measurement and thus its position upon reaching the front face of the field. In fig.10 the ray's path is shown as it enters the field and reaches a second plane parallel to the front face, or x-plane, in the field.
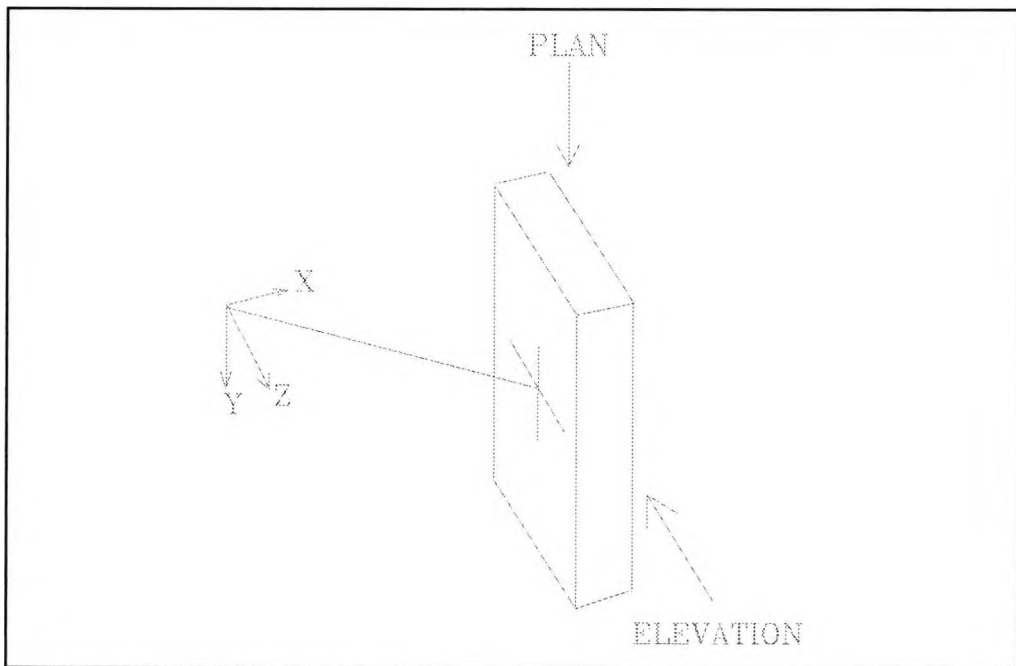
Figure 10 A ray passing between two planes in the field

By making the distance between the two x-planes equal to the length of the side of a voxel we can calculate the distance travelled by the ray between these two planes. Resolving in the x and y directions as in fig. 10 the ray length in the plan view is:

$$distance = X/\cos\alpha$$

(67)

and in the elevation:

$$distance = X/\cos\beta$$

Where **X** is the length of side of a voxel.

The ray tracing program works by using this geometry to set the voxel x-coordinate and then stepping through the field incrementing the x-coordinate by one unit at a time. By calculating the length changes in the y and z directions at each step and incrementing the existing coordinates with these the new coordinates for y and z are generated. With the y and z coordinates known for a given x coordinate the ray's path may be marked in the voxels it passes through. It is important to note that a ray may pass through more than one voxel between any given single pair of x-planes. Hence a series of tests was written in the program to check for rays entering through one voxel and exiting through another. The problem is illustrated in fig.11 below.
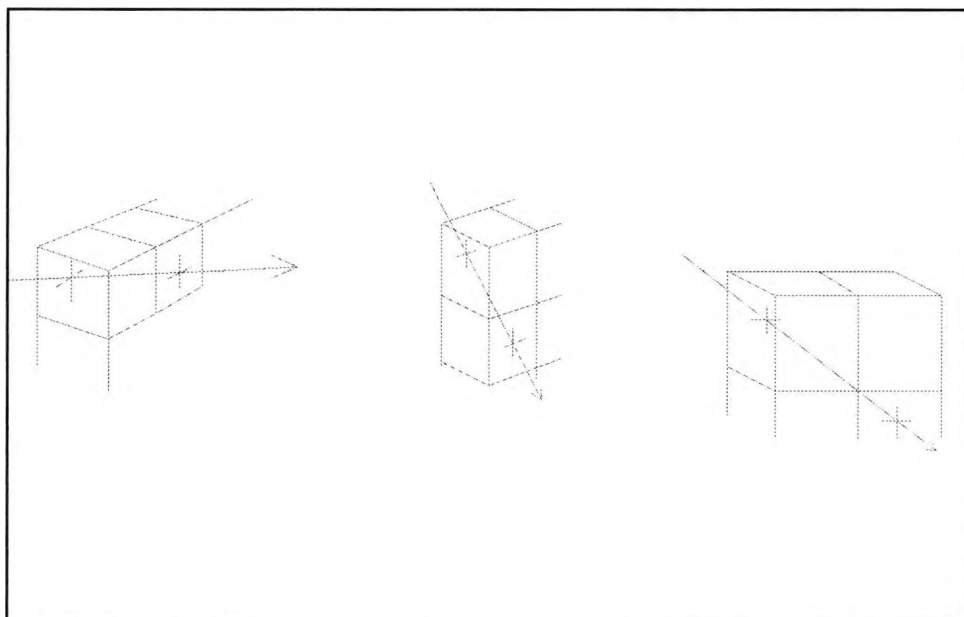
Figure 11 Three examples of possible ray paths

At this point the limitations of viewing angle must be considered as these determine the range of possible entry angles and therefore entry and exit conditions for a ray passing through a x-plane pair. Now as this work is aimed at reconstructing information from holographic interferograms with very limited viewing angles it can be assumed that the maximum values of both angles alpha and beta will be less than 45 degrees, (in fact for the interferograms under consideration they are typically less than 15 degrees). Considering the limiting case therefore were a ray is inclined at the maximum to both axes, it would pass through three voxels at most , see fig. 12.
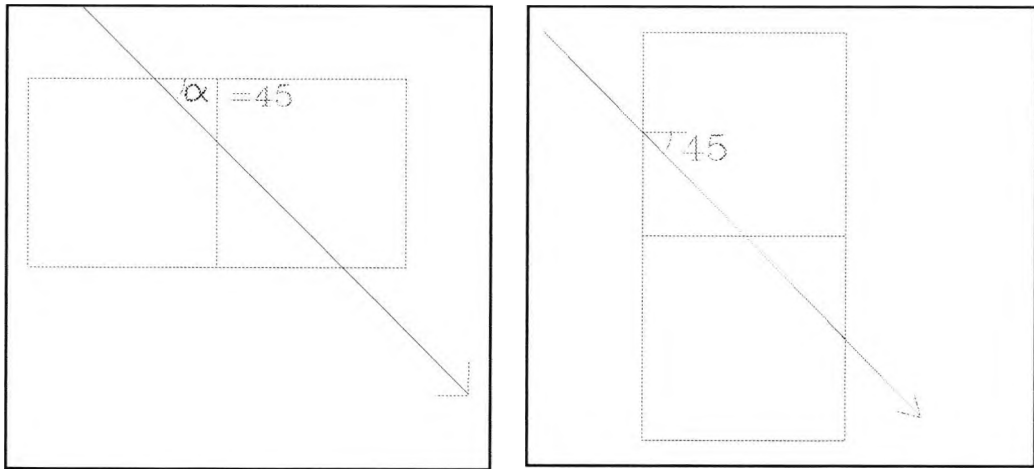
Figure 12. The plan and elevation view of a ray inclined at 45 degrees to both horizontal and vertical axes

Where a ray passes through three voxels between a single increment in the x-axis all three must be accurately identified as they will all make a contribution to the final attenuation experienced by the ray. However while it is relatively easy to mark the voxels where a ray enters and exits at x-planes some intermediate voxels passes through may not be located by this method. Hence a method had to be devised to detect these cases. This was achieved by testing the value of the z-coordinate of the ray when its y-coordinate is set at the division between the upper and lower voxels. When the coordinates of the ray at a given depth in the x direction had been found the voxels passed through for this depth increment were marked with a value corresponding to specific marker for the ray, these marked voxels were stored in a array in the tomography program so that a complete ray path could be built by stepping through the whole

54

field. This process could be repeated for all the rays from a single view so that the array would hold the paths of all these rays, and could then be interrogated to enable the processing of a single view.

While finding the ray's path the program also had to find the ray's corresponding cord lengths in the voxels passed through. Rather than take the coordinate values of the rays entry and exit points for each voxel and use Pythagoras theorem to calculate these values as method using ratios of lengths was devised. This was simpler and did not require the calculation of square roots as the Pythagoras method would have. As shown in fig.12 the length of a ray between two x-planes is given by:

$$raylength = X/(\cos\alpha . \cos\beta)$$

(69)

this value will be constant for all rays from this view point and for each pair of x-planes. Hence this length can be calculated once and subdivided into the voxels as appropriate to give the required chord lengths applying the following rules:

1) If a ray passes through one voxel only between an x-plane pair the whole ray length value is assigned to this voxel.

2) If a ray is present in two voxels, fig.13 the ratio of lengths w1:w2 is equal to z1:z2.
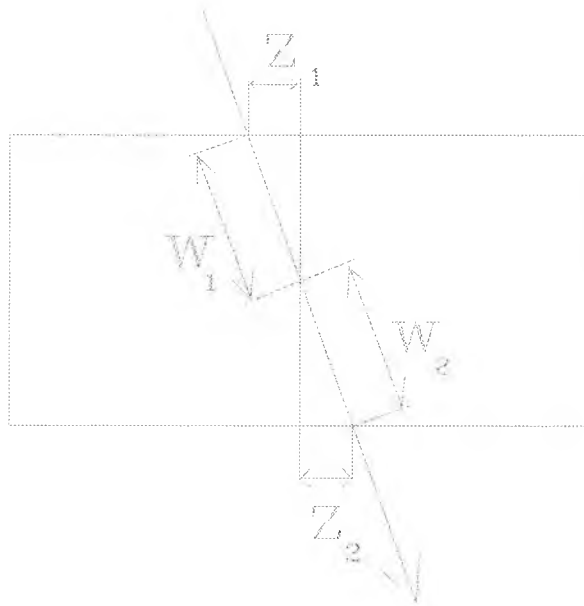
Figure 13 The plan view of a ray that passes through two voxels

3) If a ray is present in three voxels, as in figs. 14 and 15.

$w1 = w.z1/(z1+z2)$; $w2= w'.z3/(z2)$; $w3 = w'.(z2-z3)/z2$

where the z values are the distances in the z direction and $w' = w - w1$.
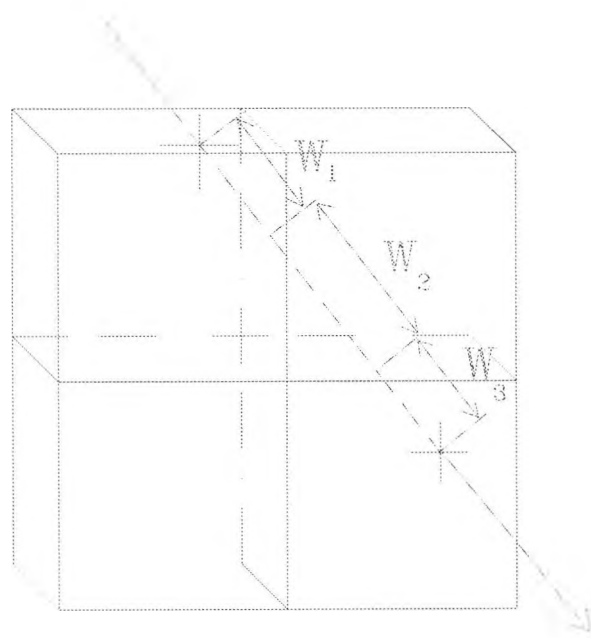
Figure 14 A front elevation view of a passing through three voxels.

Thus by calculating these **z** distances and performing the necessary arithmetic, the chord lengths could be found and the process repeated until a complete set of rays had been processed. These values are stored in a data array so the tomographic algorithm can access
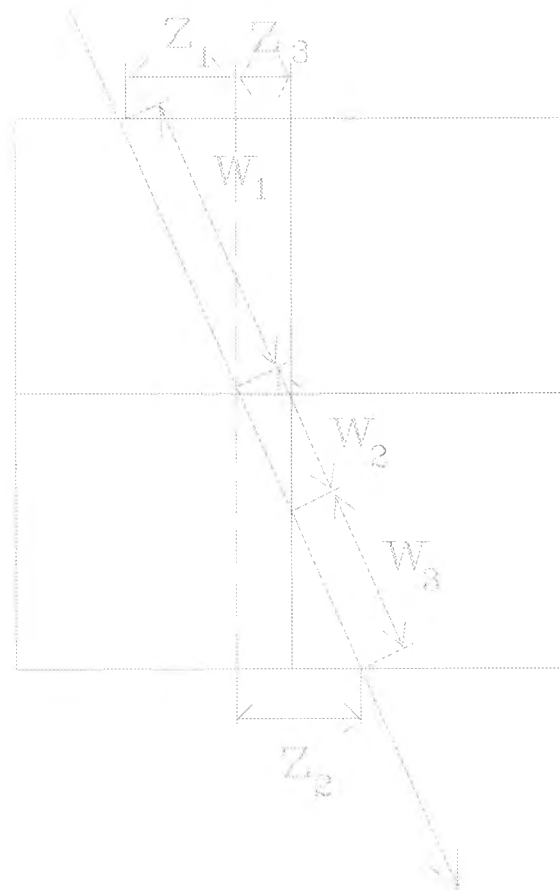
Figure 15 A plan view of a ray passing through three voxels

them. Once a view has been processed by the algorithm the next set of rays is considered in the same way.

3.1 The Tomographic Software

A new program had to be written to implement the complete tomographic process, with the three dimensional projection scheme. This was written in the C programming language as it combines efficient compilation generating fast running codes, with the ease of programming associated with high level languages. The overall aim of the program implementation was to enable easy modification of the program and maximise its flexibility. These points were considered to be of paramount importance, as it was foreseen that the details of the problem to be solved and the optimum method of solution would almost certainly be modified with greater experience of applying the tomographic techniques.

A flow chart of the process is shown in fig. 16.
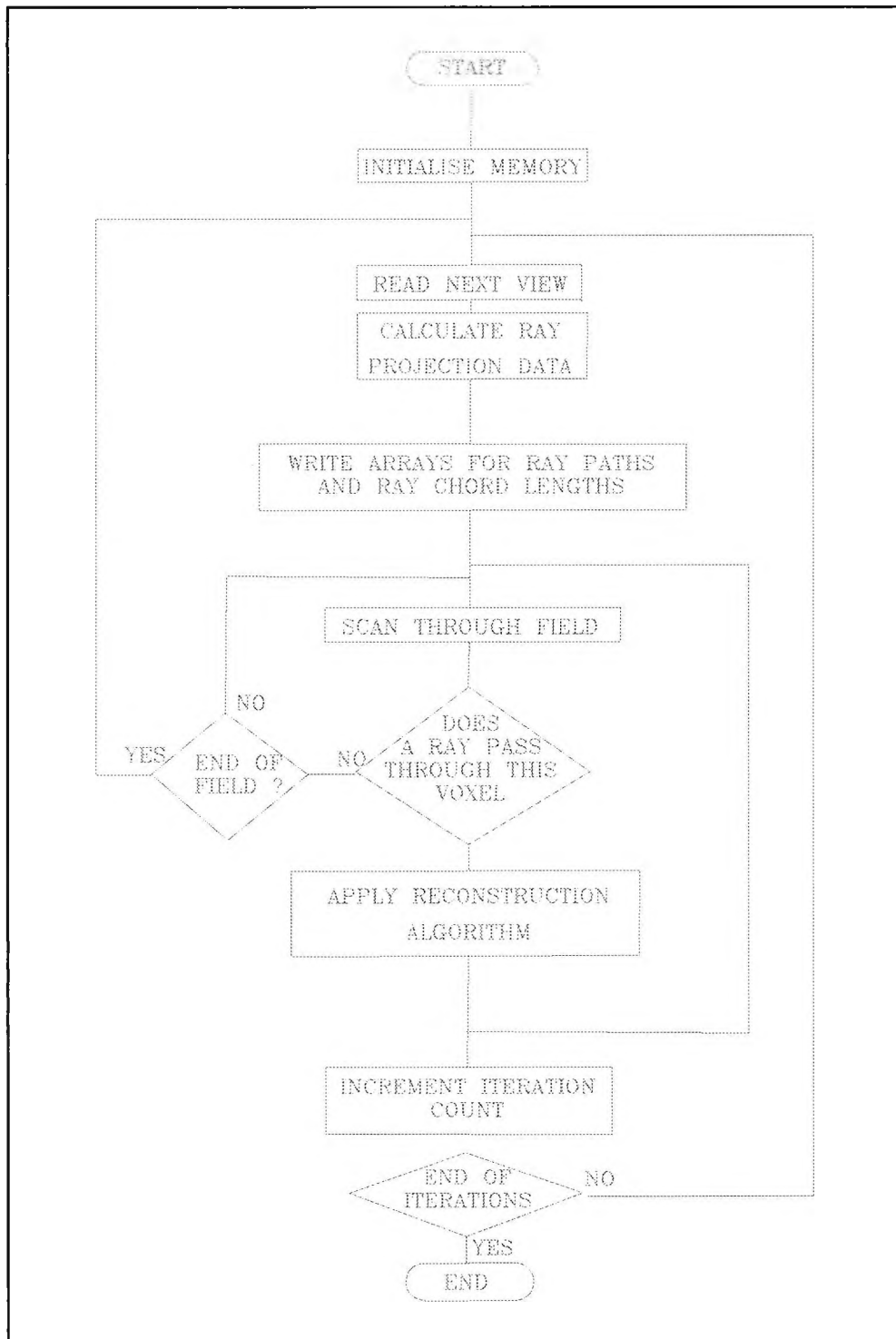
Figure 16 The tomographic reconstruction program flow chart.

The first step in the program is the allocation of the memory required by various data sets. The principle areas are the arrays for the storage of the reconstructed field, the individual ray lengths in

each of the voxels, (both 100 x 100 x 100 array of floating point numbers in the final form of the program), and the array used to store the ray paths through the field from a single view, (a 100 x 100 x 100 array of integers).

Once the memory has been allocated and the variables declared the main operation of the program can begin. Each view is read from disk by its own module in the program which contains the instructions for the handling of that particular view, i.e. the angles of inclination of the view and its relative position to the field. Having separate modules for each view allowed the greatest flexibility when inputting data to the program.

The positional and angular data for each view is passed to the appropriate geometry generating sub program where the ray paths for the view are traced and the individual chord lengths are calculated for each voxel. This data is then passed to the individual view module where the tomographic reconstruction algorithm is applied to each voxel in the reconstructed field. When the data for a particular view has been considered the program moves to the module for the next view and repeats the process.

After all the views have been considered in turn the program notes that a single iteration of the tomographic reconstruction process has been completed and the whole process can start again from the first view depending on how many iterations have been specified.

Finally when all the iterations have been completed the reconstructed array is written to the hard disk.

The structure of the program was such that the alternative algorithms used required only minor changes so that it was possible to implement the ART, the Lent MART, and the Gordon and Herman MART algorithms with only minor changes. Having calculated

the appropriate geometry data the algorithms core calculations required on a few lines of program at the centre of several program loops. This approach proved satisfactory through out the testing of the tomography system.

4.0 Comparative tests of the iterative algorithms

In the theory section it was explained that there are several algorithms that can be applied to limited angle tomographic reconstruction problems and there is considerable doubt as to the best possible approach in any given situation. This being the case it was decided that to determine the most suitable one for our purposes we should experiment with several different algorithms.

Of the algorithms previously described, the ART, the Gordon and Herman MART and the Lent MART algorithms were selected for trial implementation. They were applied to both model data and real data in a series of comparative tests. The reasoning behind this choice was that the ART algorithm would provide a well proven standard to test any other algorithms against, the Lent MART algorithm could provided experience of maximum entropy type algorithms, and the Gordon and Herman MART algorithm should give good performance, having been cited as the best performing MART algorithm in a recent review, ref.[4].

Before comparing the results produced by the individual algorithms the basis for selecting a particular output from a series of iterative solutions produced by a given algorithm must be considered. As these are all iterative schemes a decision must be made as to the point when they should be terminated. This can be on the basis of the reconstruction having reached some stopping criterion, or having performed a certain number of iterations, or the time a program has run for. As the initial tests were carried out on an IBM PC compatible computer, where the run time of the program could reach several hours when reconstructing a 30x30x30 field using the 3-D

projection scheme, a limited number of iterations had to be used. However when reconstructing with the Silicon Graphics computer the speed of the workstation allowed more iterations and thus the stopping criterion used was the minimisation of the solutions error.

For the reconstruction of a known test field there are a number of different performance criterion which can be applied to tomographic reconstructions produced. The simplest is to take the sum of the differences between the value of each voxel in the reconstruction and the corresponding voxel in the test field and the divide by the number of voxels. This gives the average difference in each voxel, or the absolute error.

$$\textit{Performance Figure } 1 = \sum_{0}^{i}\sum_{0}^{j}\sum_{0}^{k}[\,|(x_c-x_r)|/\Sigma(i).\Sigma(j).\Sigma(k)]$$

(70)

where x_c is the calculated voxel value and x_r is the voxel value from the reconstruction.

The drawback to using this parameter for the evaluation of error is that when reconstructing sparse fields small back ground errors may swamp the more significant errors in the reconstructions features. For example in our 100x100x100 field the cross feature is present in 5000 voxels, therefore the background has 995,000 voxels and if these have an average error value only 0.05% that present in the cross reconstruction they will still contribute equally to the value of this performance figure. Because of this

the value of absolute error was also calculated in the immediate area surrounding the test object as well as across the whole field and the results of these are given.

A second performance parameter was devised which calculates a R.M.S. value for error across the field.

$$Performance\ Figure2 = \sqrt{\sum_0^i \sum_0^j \sum_0^k [(x_c - x_r)^2 / \Sigma i . \Sigma j . \Sigma k]}$$

(71)

This value gives much higher weighting to errors in reconstructing higher density features, i.e. those which are important for feature recognition. Hence performance figure two is the appropriate guide for sparse fields and performance figure is useful for dense evenly populated fields. Together they can provide a useful indication for the performance of the reconstruction in terms of both general field accuracy and specific feature reconstruction.

In Verhoeven's review of the various MART algorithms he used four error factors; the average error, (equation 70), the normalised r.m.s. error, (equation 71), the normalised absolute error, (equation 73), and the maximum error.

$$PerformanceFigure3 = \sum_0^i \sum_0^j \sum_0^k [x_r - x_c] / \sum_0^i \sum_0^j \sum_0^k [x_r]$$

(73)

Verhoeven defined the maximum error as the largest difference between the reconstruction and the test model. He also note that the normalised absolute error emphasized the effect of many small errors.

65

As the calculation of these parameters takes relatively little time compared to the actual reconstruction process, all four of the performance factors were calculated for each reconstruction. In practice it was found that the data produced by error values given by Performance Figures 1 and 2 were sufficient to evaluate the performance of the tomographic processes as Performance Figure 3 did not produce any useful values.

4.1 The test object

The test object we devised was a pair of thin planes set at 90 degrees to each other in a cube of lower density. This was in order to evaluate the effect of the tomographic process on a three dimensional object that had some structural similarity to the Rolls Royce holograms. As the holograms principle feature is a shockwave that is roughly planar this seem a suitable choice. The complete test field comprised the two square planes of 50x50 units and density value 100 set in a 50x50x50 cube of density 10, surrounded by a background null field of 100x100x100.

A simulated series of views of this object was generated by writing the models data in a computer program and using a modified version of our projection program. This calculated the attenuation that a ray from a given direction would experience when passing through the field by tracing the ray's path through the field, identifying the voxels it passed through, calculating the contribution of each voxel by the product of the ray length passing through the voxel and the attenuation present, and finally summing these values along the whole path of the ray. In practice the program to produce this data was incorporated in the tomography program so that the data for each view

was generated when the program was run.

4.2 The effect of different relaxation factors on convergence

In order to perform comparative tests between the different algorithms it was necessary to select the relaxation factors to be used with the MART algorithms. This was to ensure that the optimum results from each reconstruction technique would be compared. Because of this we carried out tests on the effects of various relaxation factors. Once these had been carried out it was possible to select the most appropriate value of relaxation factor for use with the algorithm in the comparative tests.

The effect of different relaxation factors on the convergence of the MART algorithms is illustrated in the following graphs, figures 17 and 18.
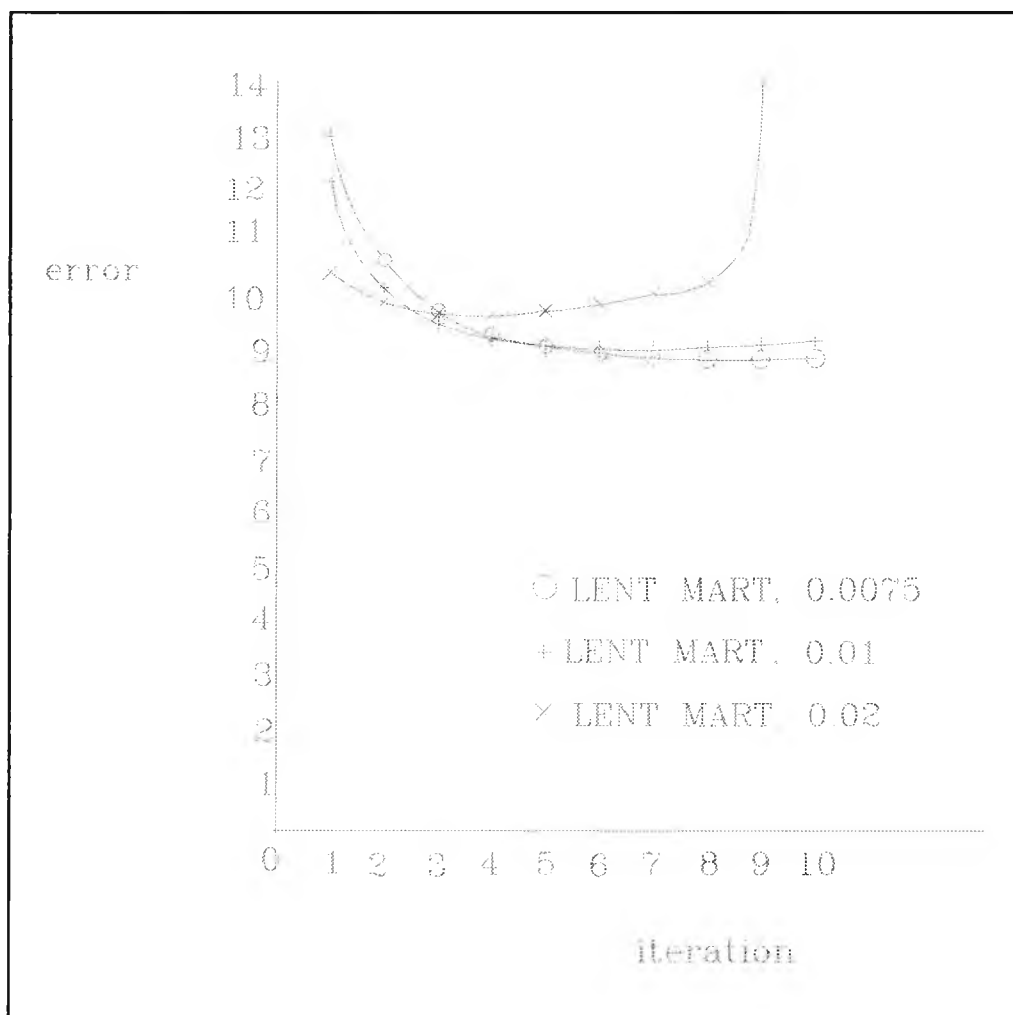
Figure 17 The variation in absolute error in a 50x50x50 area about a the test object for different relaxation factors.
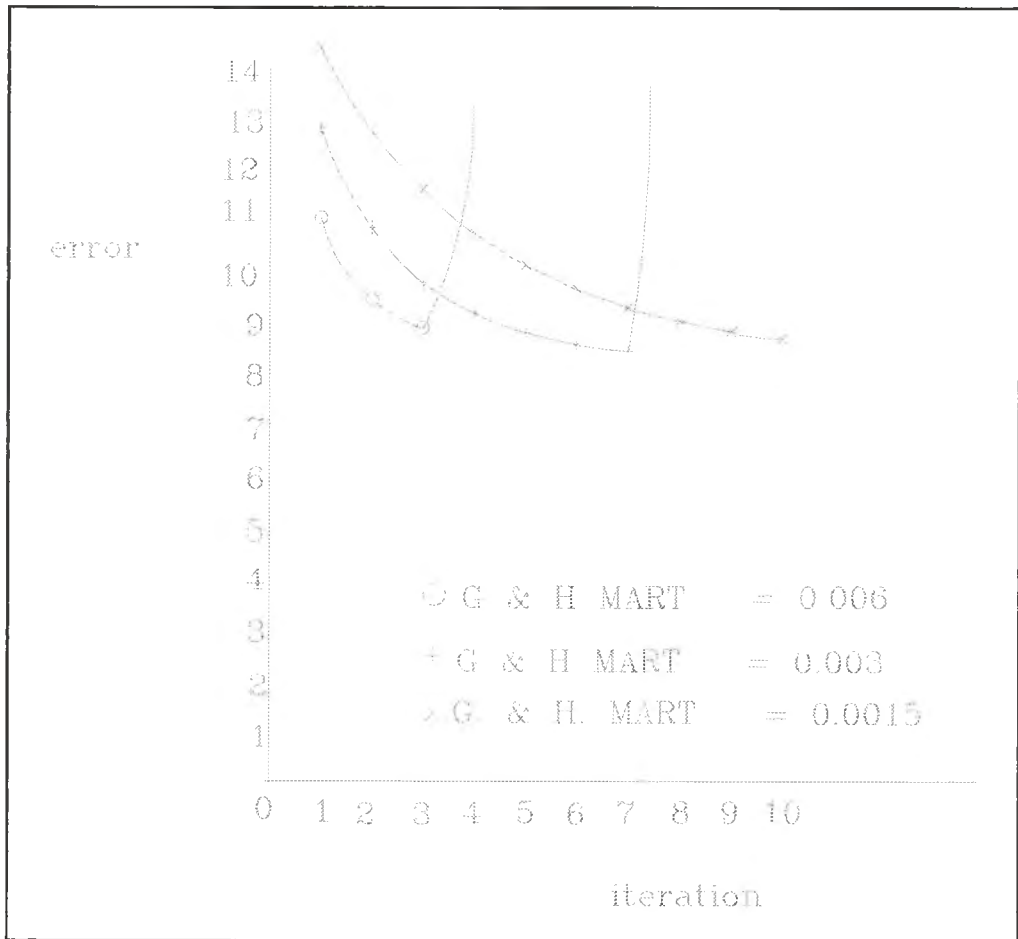
Figure 18 The error in a 50x50x50 cube about the test object, for three different relaxation factors.

It can be seen in these both these graphs that reducing the relaxation factor gives a slower reduction in error initially, but as the number of iterations increases a more stable convergence. This behaviour is entirely consistent with previous investigations described in the theory section.

From these tests the relaxation factors which gave the lowest error values for 10 iterations were chosen and the reconstructions they produced were used to represent the MART solutions in our comparisons. For the Lent MART algorithm the relaxation factor value used was 0.0075 and for the Gordon and Herman MART 0.0015 was used. Having determined the appropriate relaxation factors for the MART algorithms we could

proceed to compare the different types.

4.3 Comparative results for different algorithms

The comparative results of the different algorithms performance are illustrated in a series of graphs of error verses number of iterations. The first graph, figure 19, shows the average absolute error present in the immediate area of the test object, (a 50x50x50 cube about the two planes), for the three algorithms. The error for the ART reconstruction shows a steady reduction converging to fixed value as the tenth iteration is approached. In contrast the Lent MART curve shows a steep drop for the first few iterations, then a flat bottom to the curve as the error reaches a minimum, followed by a steep increase in error as the reconstruction becomes unstable. The error value for Gordon and Herman reconstruction is the highest initially then declines steadily to be the lowest of the three after ten iterations, 8.48 against 9.45 and 9.14 for the ART and Lent MART respectively. The lowest error value for the Lent reconstruction actually occurs at the seventh iteration at 8.98, still lower than the Gordon and Herman MART.
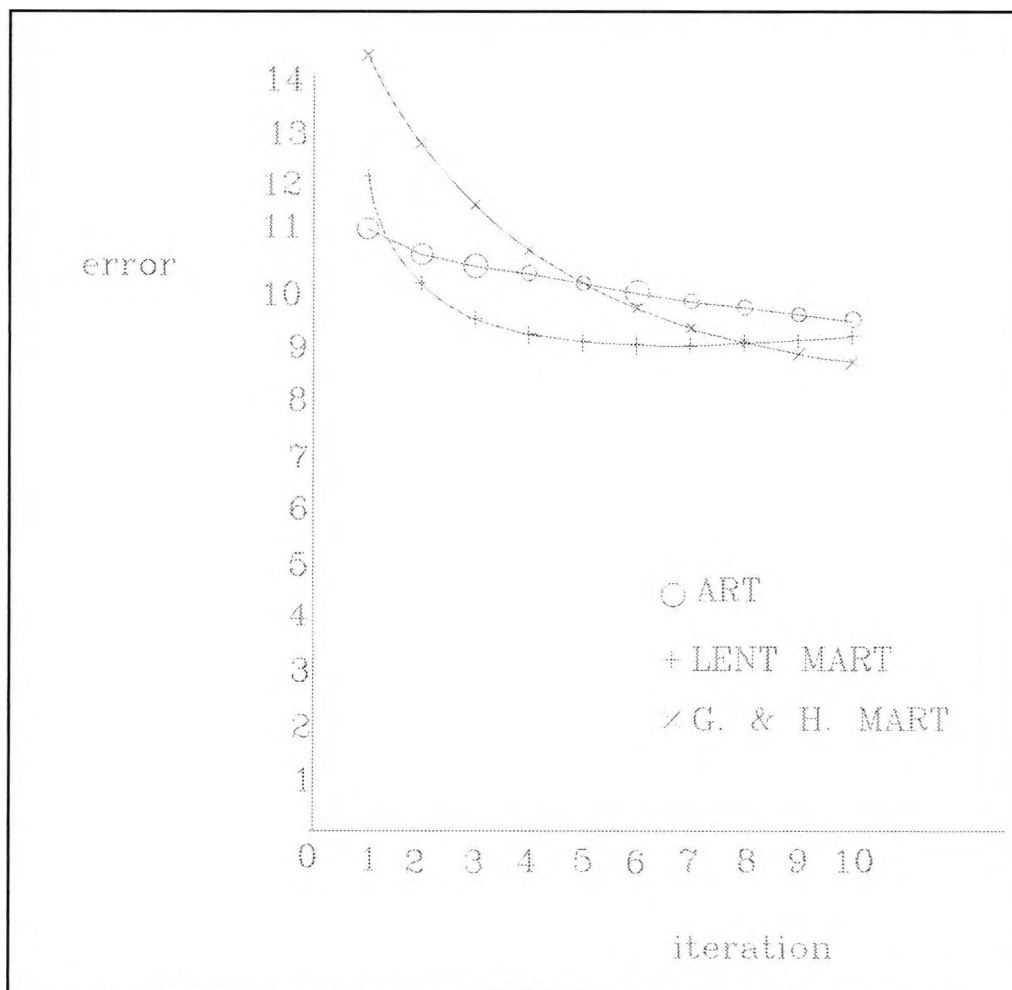
Figure 19 The absolute error in a 50x50x50 area around the test object.

The absolute error produced across the whole 100x100x100 field by the different algorithms is shown in fig.20. This graph shows the MART algorithms giving a lower error value than ART. We can also see that the Lent MART shows a sudden increase in error after four iterations .However as this occurs while the error in the 50x50x50 area is still falling. From this discrepancy between the reduction in error produced close to the object and the error in the complete field it can be deduced that the Lent MART produces "noisy" reconstructions, with spurious features introduced in the background field. Again this

behaviour has been reported by previous investigators.
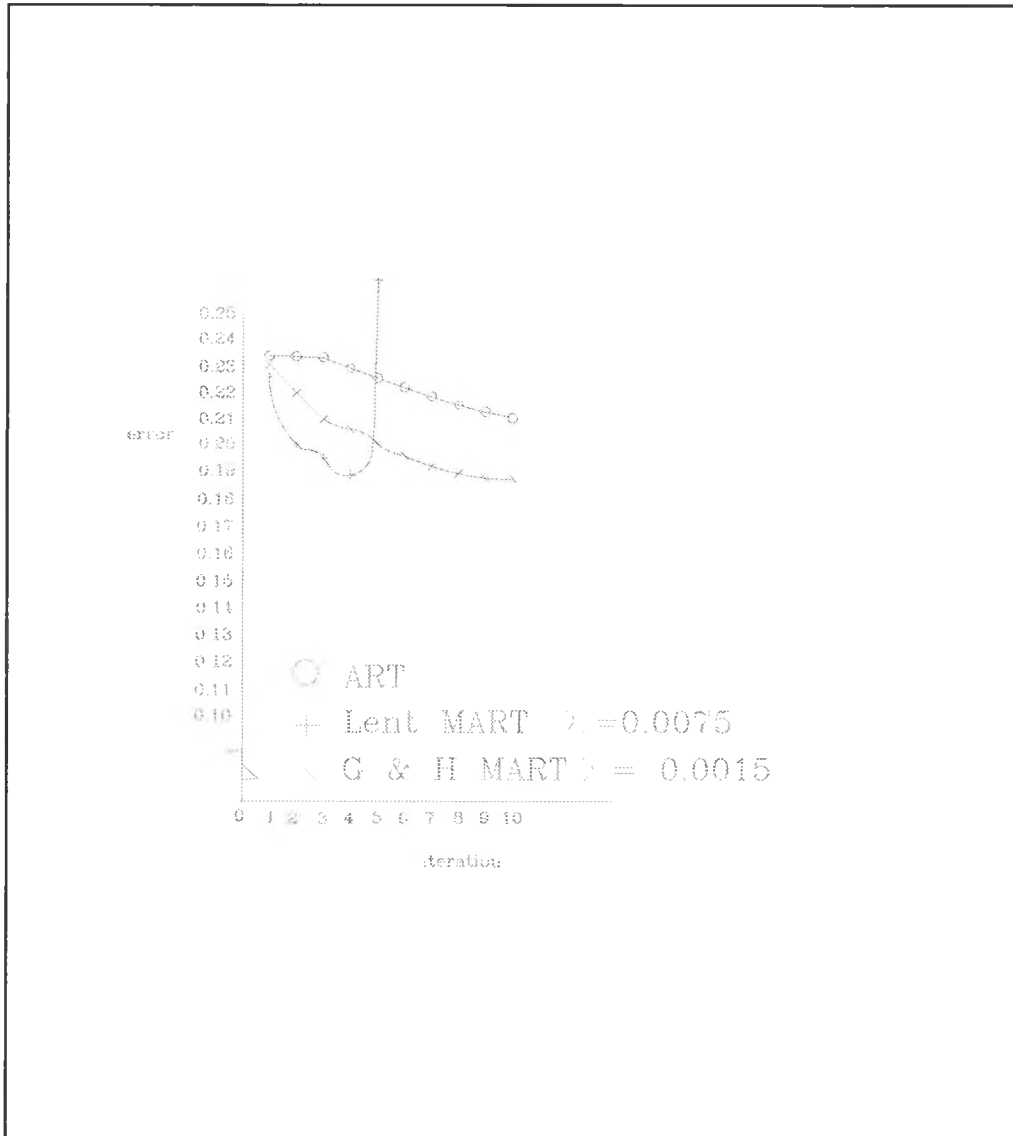
Figure 20 The absolute error across the 100x100x100 field for the three algorithms.

In contrast the Gordon and Herman MART produces similar curves for absolute error in both the 100x100x100 and the 50x50x50 field, with a steady reduction in error seen in both. It also has a clear superiority over the ART with lower error values

across the range of iterations for the whole field case and from the fifth iteration onward for the immediate object field. The lowest error for each occurs at the tenth iteration, 0.180 verses 0.211 for the Gordon and Herman MART and ART solutions respectively. The Lent MART reaches it's error value at iteration 3 with a value of 0.190, before it rapidly increases to an out of range value by the tenth iteration.

4.3.1 Visualisation of the reconstructed objects

The resultant reconstructions produced by the Lent and Gordon and Herman MART after 10 iterations were used for visual presentation, however the ART algorithm required 20 iterations to produce clear results and thus the ART images shown are after 20 iterations these tests. The views of these three reconstructions are shown in fig. 21 to 32. The cross reconstructions are shown as an iso-surfaces (with the level set to 50% of the value of the test pattern) and as a series of orthographic slices, (coloured from red to violet with red representing zero and violet 100 units). The orthographic slices are taken in three orthogonal directions through the field, cut through the centre of the field.
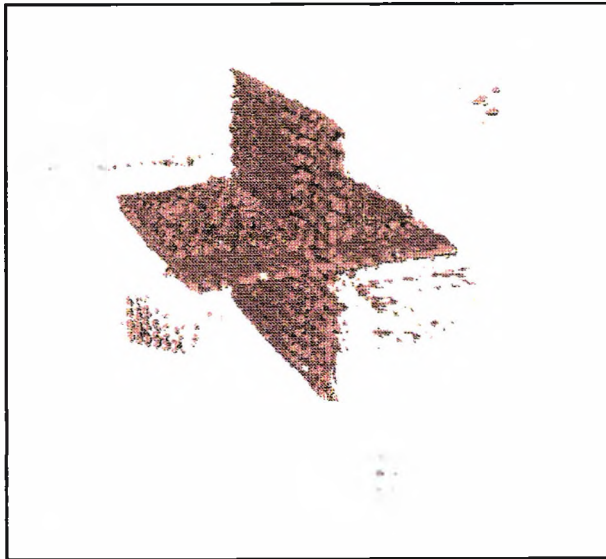
Figure 21
The iso-surface
of the ART
reconstruction
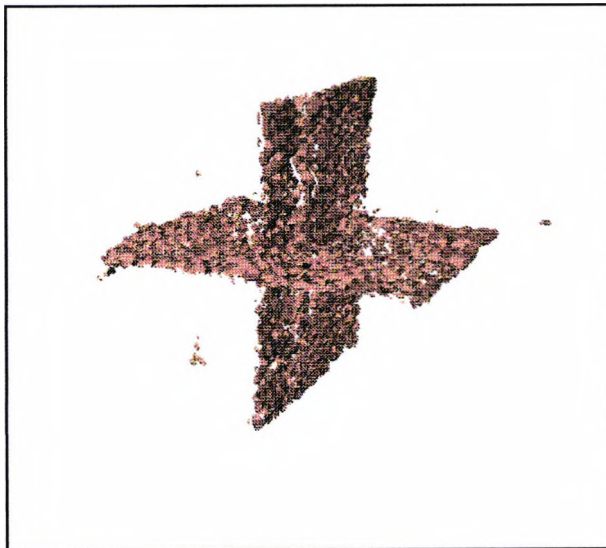
Figure 22
The Gordon and
Herman cross
recostuction
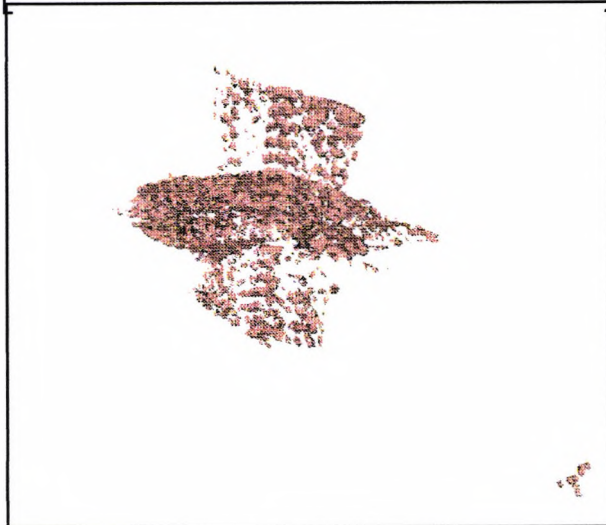
Figure 23
The Lent Cross
reconstruction

Figure 24
The ART
reconstruction
sectioned
perpendicular to
the viewing
direction
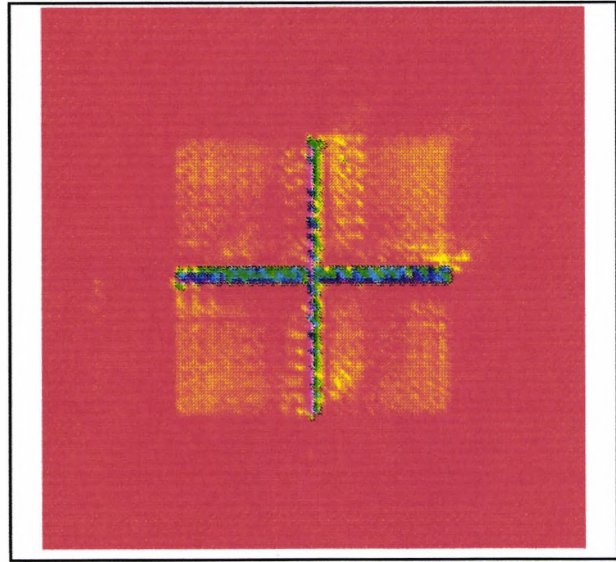
Figure 25
The Gordon & Herman
MART reconstruction
section
perpendicular to
the viewing
direction
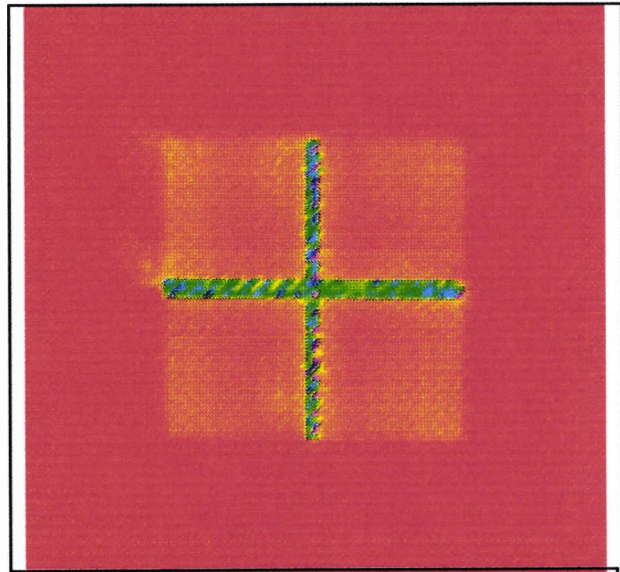
Figure 26
The Lent MART
sectioned
perpendicular to
the viewing
direction
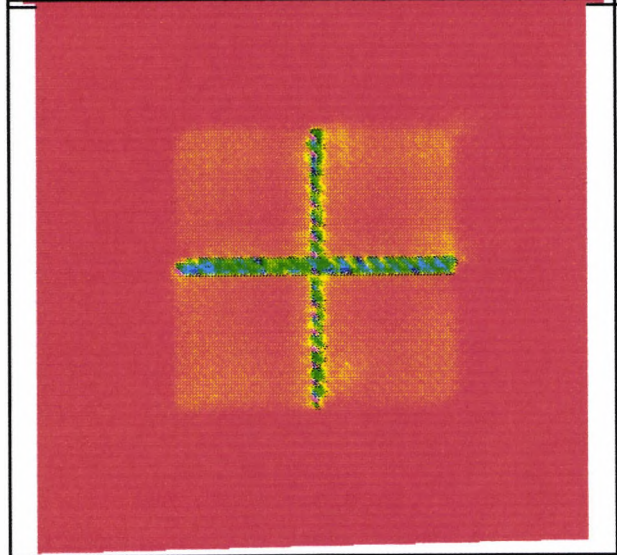
Figure 27
The ART cross
sectioned through
the vertical plane
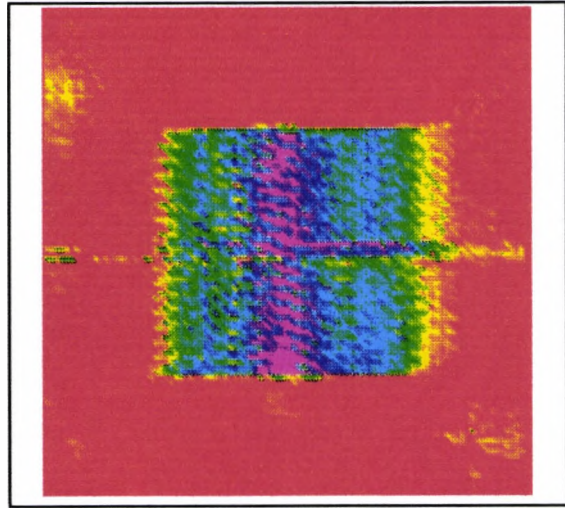
Figure 28
The Gordon and
Herman MART cross
sectioned through
the vertical
plane
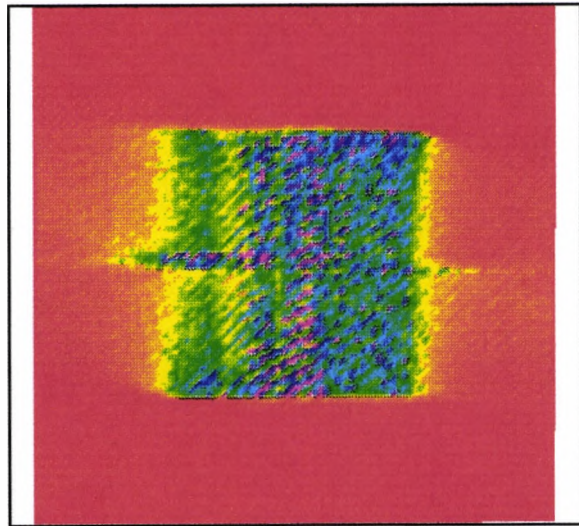
Figure 29
The Lent MART
cross sectioned
through the
vertical plane
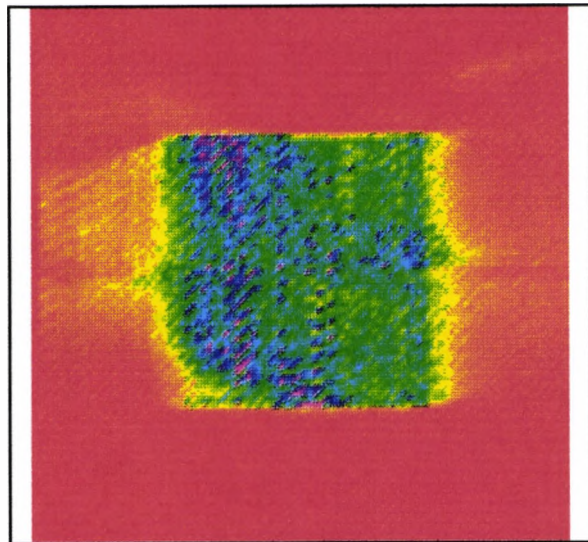
Figure 30

The ART cross section through the horizontal plane
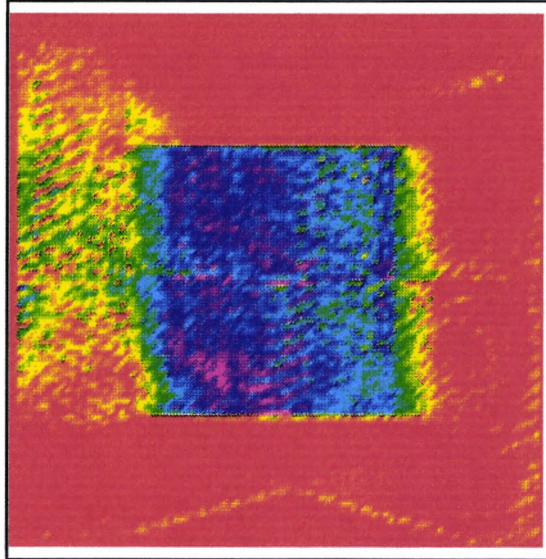
Figure 31

The Gordon and Herman MART cross section through the horizontal plane
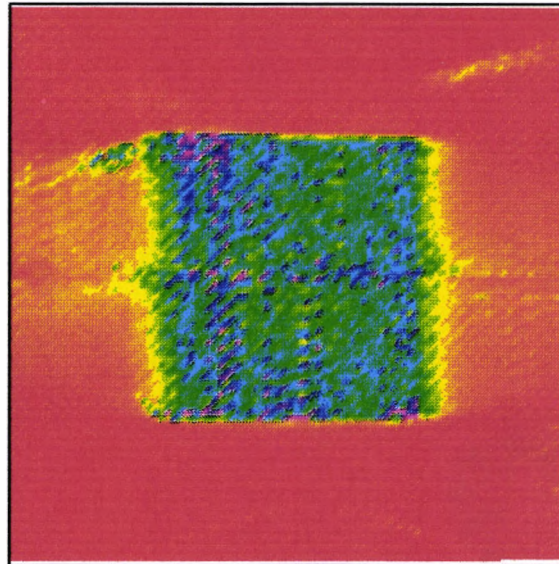
Figure 32

The Lent MART cross section through the horizontal plane
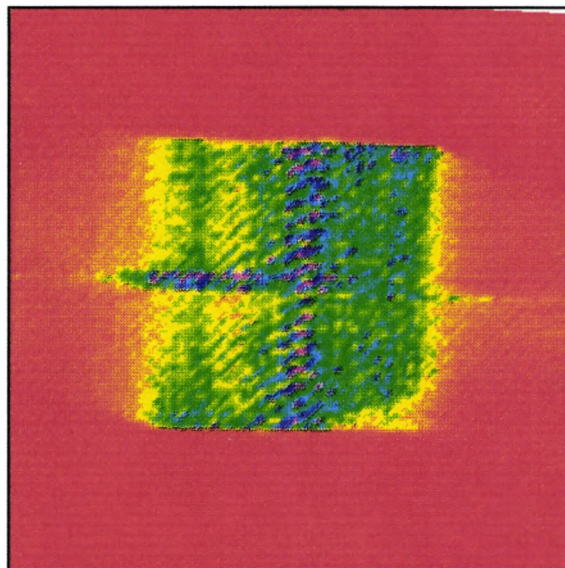
If we compare the iso-surfaces generated from each of the reconstructions some general traits can be decerned. The figure produced from the ART reconstruction clearly shows the shape of the cross with the surfaces of the object appearing smoother than either of the other iso-surfaced images. There are however some noticeable artifacts in the image that have been introduced during reconstruction. The Lent MART figure contrasts strongly with this by giving an extremely speckled appearance to the crosses surface, making it appear to be made up of discrete points rather than continuous plane and giving a poor representation of the objects original shape. The iso-surface of the Gordon and Herman MART reconstruction shows a sharp cross outline with the general object shape well preserved. The surface of the figure is not as smooth as the ART version but there are not the large number of artifacts found with the ART. Comparing the sectional views we can see some important differences in the behaviour of the algorithms. The sections perpendicular to the axis of the cone of views all show the two planes with their axes at 90 degrees to each other, thus no noticeable geometric distortion was produced by during reconstruction. However the surrounding cube field in the ART reconstruction shows a large distortion in it's shape compared to the other algorithms with the area near the cross figure failing to reach the level of the outer areas of the cube. An explanation for this would be the algorithm erroneously attributing the data indicating density in this areas to the nearby cross object. The variation in the cube field is less noticeable in either of the other sections although a similar dip in cube density near the cross can be decerned. A feature's colour in these views indicated it's density value and it should be noted

that the MART reconstructions have approached the correct density value for the cross and cube after 10 iterations where as the ART algorithm required 20 iterations. These density distributions are apparent in the sections through the centres of the planes. The ART reconstructions density increases noticeable toward the middle of the cross in the vertical plane whereas the Gordon and Herman MART has a much more uniform density across the whole plane. The Lent MART is similar but shows more individual density peak values in the plane and has a rounding off of the trailing edge of this plane. In terms of feature confinement the MART algorithms perform better than ART which shows the horizontal plane of the cross noticeably extending along the direction of the viewing cone. From these observations it was deduced that the Gordon and Herman MART algorithm had produced the reconstruction that was the most faithful to the original test field after 10 iterations and was still superior overall to the ART algorithm when that was used over 20 iterations.

4.3.2 Distinguishing objects from the background field

Placing the cross object in a cube of lower density had allowed us to investigate the ability of the tomographic process to extract features from background field density and the outline of the cross test feature was clearly visible when the cross feature was surrounded by a cube with a density of 10% of the crosses. A further test was carried out with the background cube value increased to 50% of the cross feature density. The iso-surfaced cross and orthographic slices shown in figures 33 to 35 illustrate the results of this test.

Looking at the iso-surface of the cross we can see that the pattern is now more broken up with artifacts appearing from the background cube. When the level
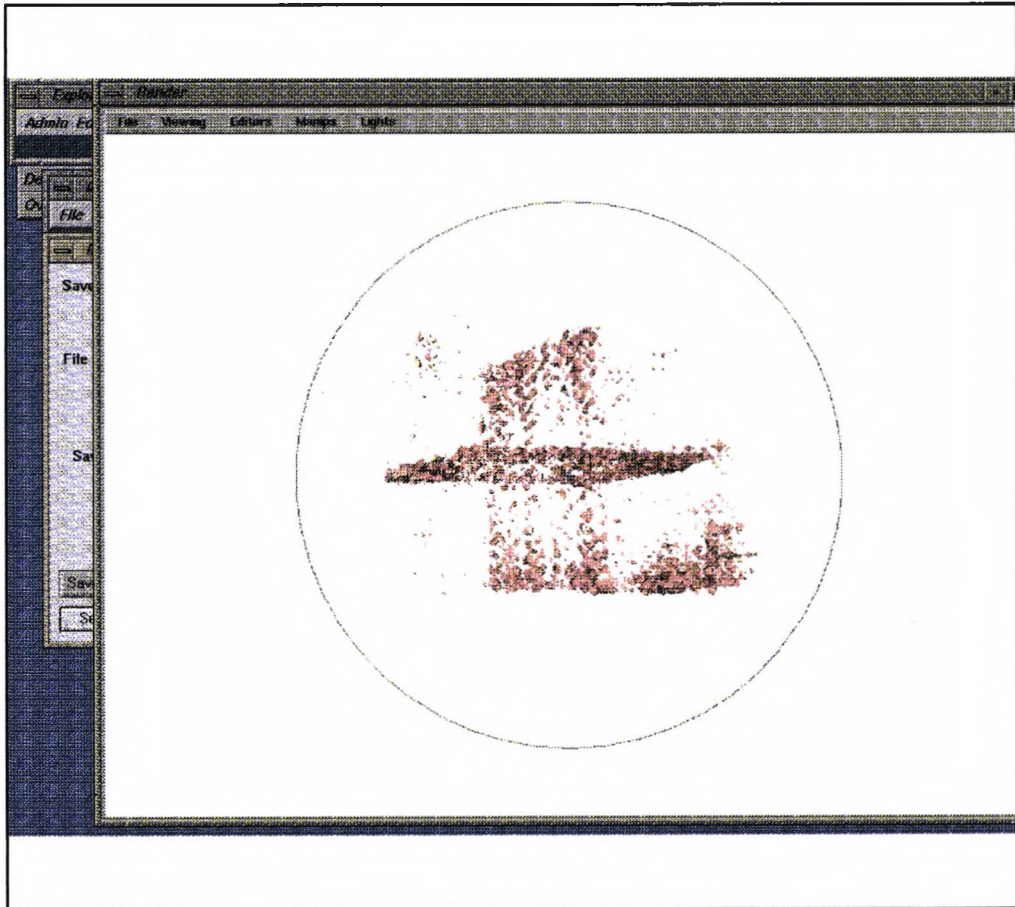
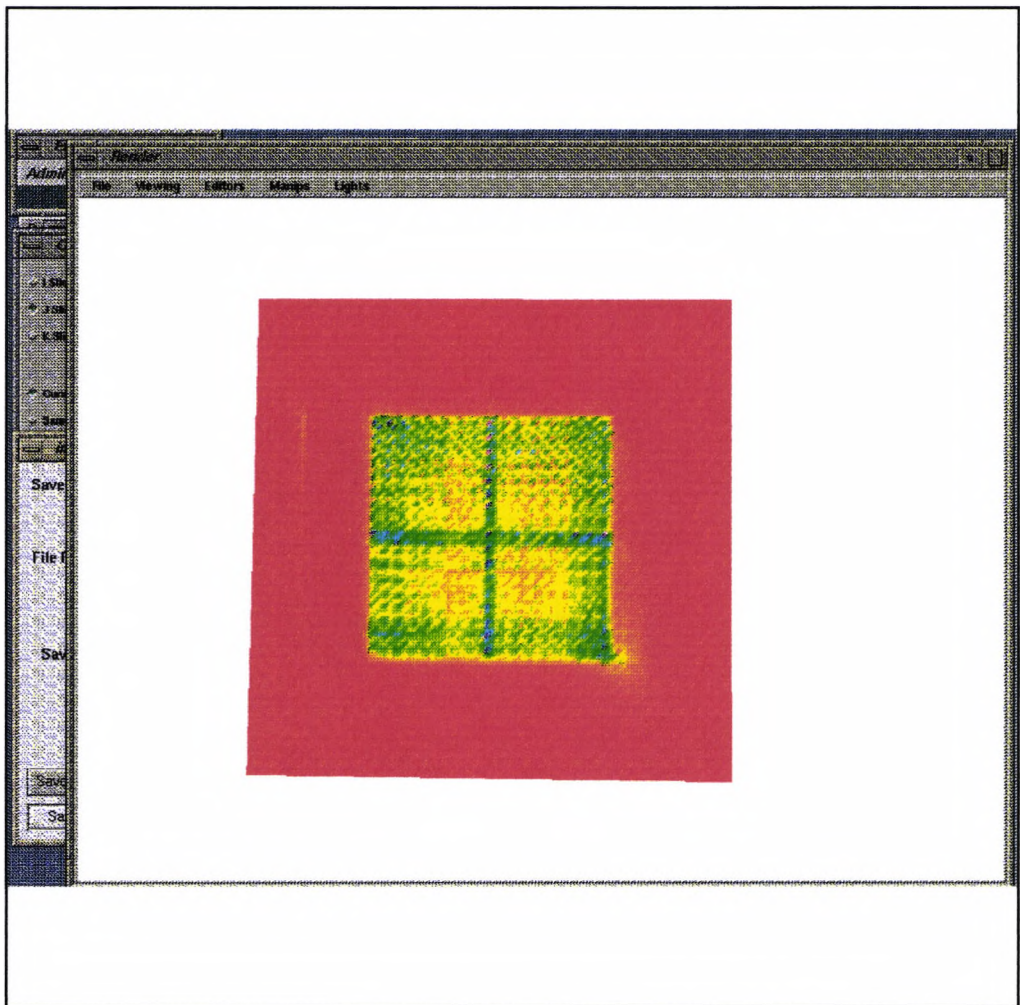**Figure 33** The iso-surface of the cross in a 50% background

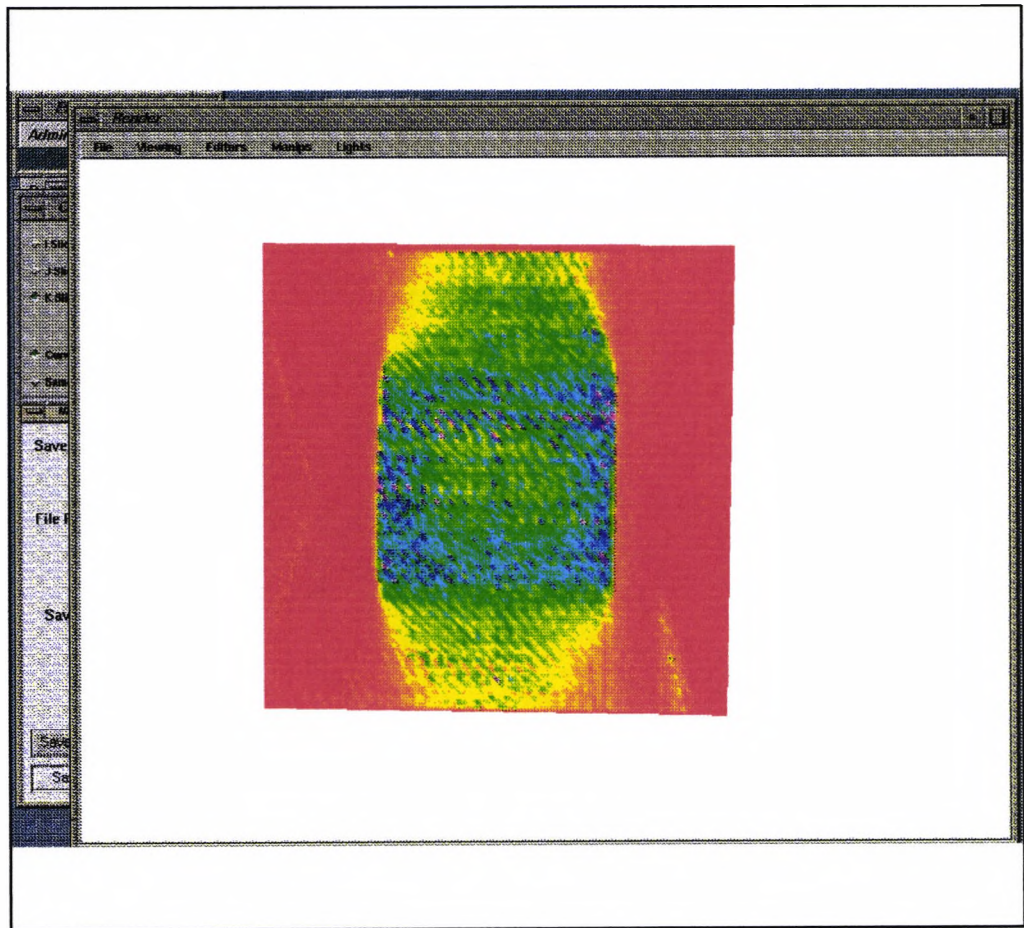**Figure 34** The section through the cross perpendicular to the viewing direction

Figure 35 The cross section through the vertical plane

for generating the iso-surface was increased so that a more continuous surface might be produced for the cross the result was this feature became indistinguishable from the background. As we would expect the separation of the object from the background field had become more difficult. This point was also illustrated by the sectional views, as although the planes that make up the cross are still visible they are much closer to the background density. This reduction in contrast between the cross and the background field is as we would of course expect with the increased field density. However it was still possible to distinguish the cross from the field and hence our tomographic approach was still viable under these conditions. When a further test was attempted with the cube's density value set to 90% of that of the cross object no pattern could be decerned in the reconstruction. This gives us a useful guideline for the minimum contrast required for reconstructing thin objects in density fields when relying on limited angle data, that is, an object may be resolved when it's density is twice that of a field surrounding it.

4.3.3 Spherical shell test pattern

To determine the effect of the tomographic process on more complex shapes a hollow sphere was programmed as a test object. This would test the reconstruction processes ability to cope with both curved surfaces and hollow objects. It's symmetry in all axes passing through it's centre made it particularly suitable for investigate the effect different angles for the cone of view when the cone's apex was coincided with the spheres centre. That is as the cones angle changed no fundamentally different features appeared in the ray data, only their angular displacement was altered and this effect only gives rise to changes in the

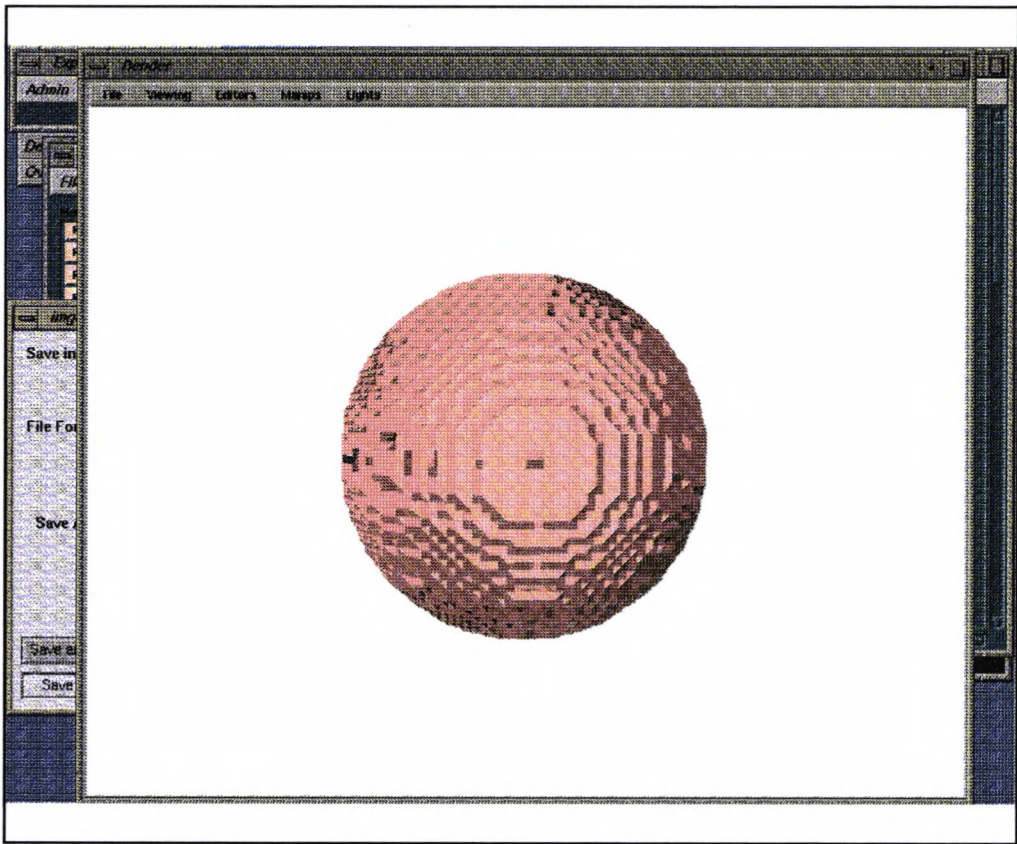reconstruction. The sphere test object is shown in figure 36.

Figure 36 The spherical test object

The sphere was 50 units in diameter and it's shell thickness was one unit. It was located centrally in the field. The first reconstruction was performed over a range of angles of +0.3 and -0.3 radians in the vertical and horizontal axes using the Gordon and Herman MART. The resultant reconstruction is illustrated in figures 37 to 40.
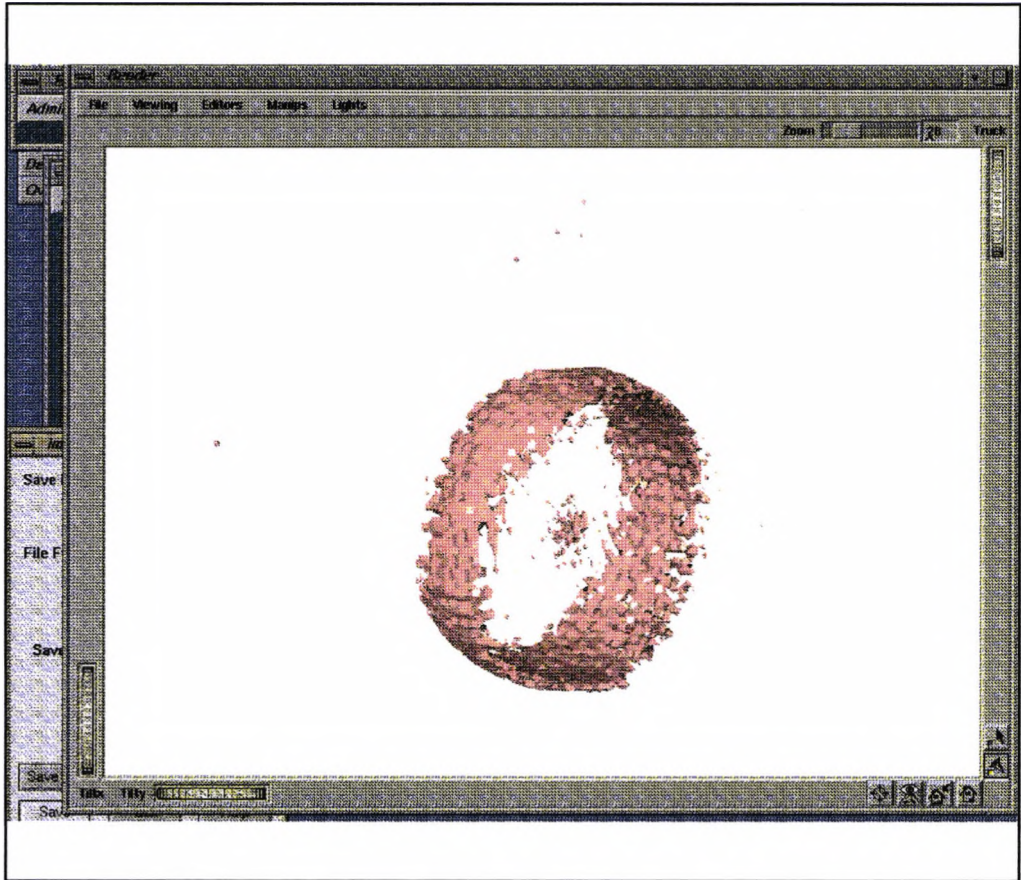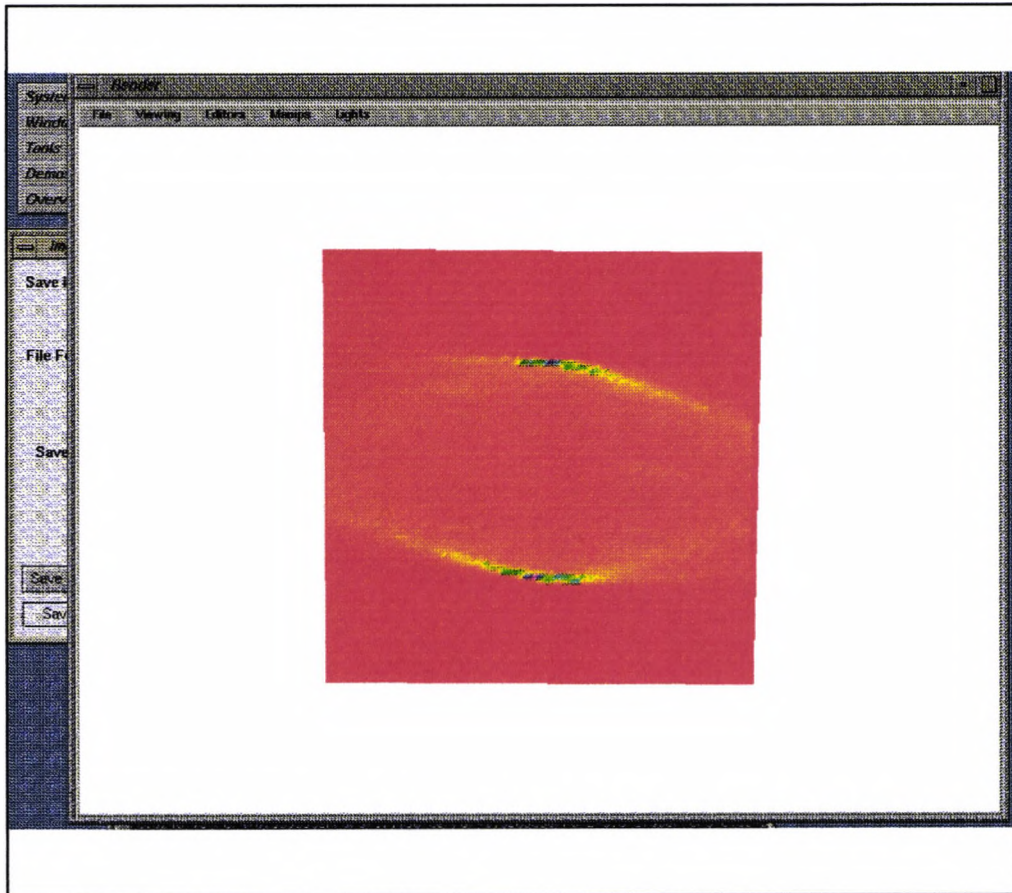
Figure 37. The iso-surface of the shell sphere reconstruction.

Figure 38 A sectional view through the hollow sphere cut along the direction of view in the vertical plane
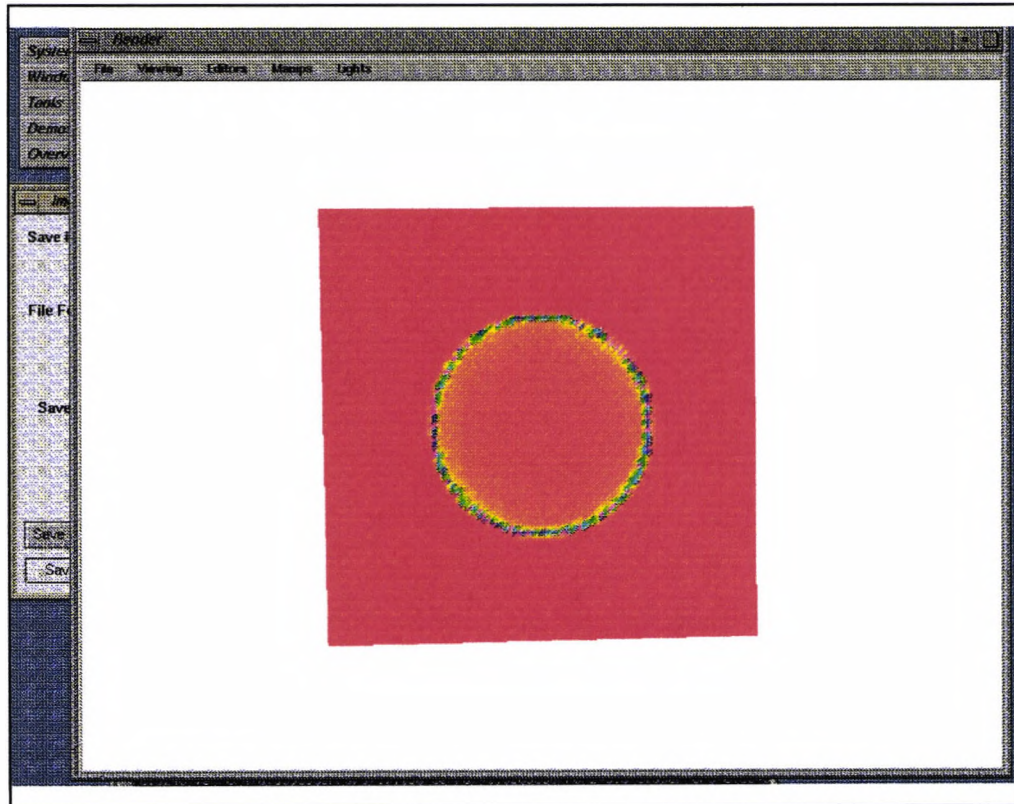
Figure 39 A section cut through the mid-point of the sphere perpendicular to the viewing direction.
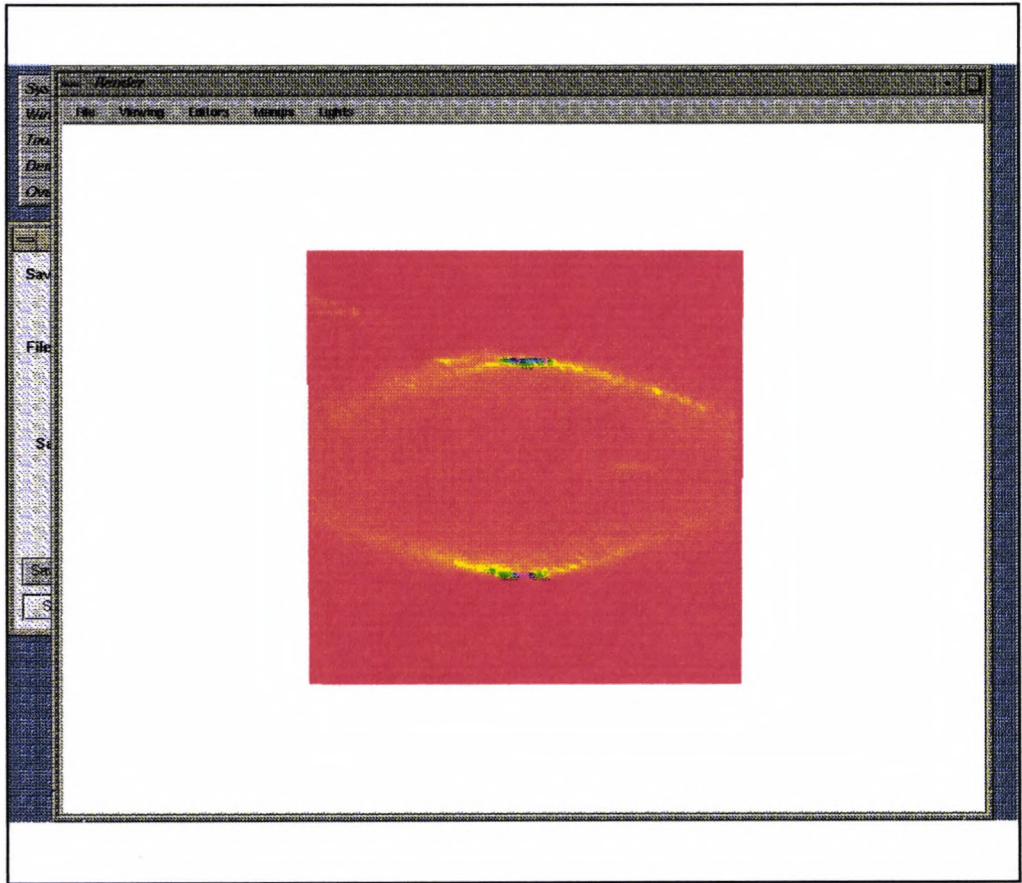
Figure 40 A horizontal section through the centre of the sphere

The first most noticeable feature of this iso-
surface is that the front and rear of the sphere,
(relative to the direction of view), have been lost in
reconstruction. This gives the "ring" like structure
were the wall of the sphere was at it's steepest
incidence to the viewing direction. To explain this
loss of the front and rear of the sphere we should
consider the difference in the information captured by
the rays passing through these areas. For the sides of
the sphere sampling rays pass through these areas as
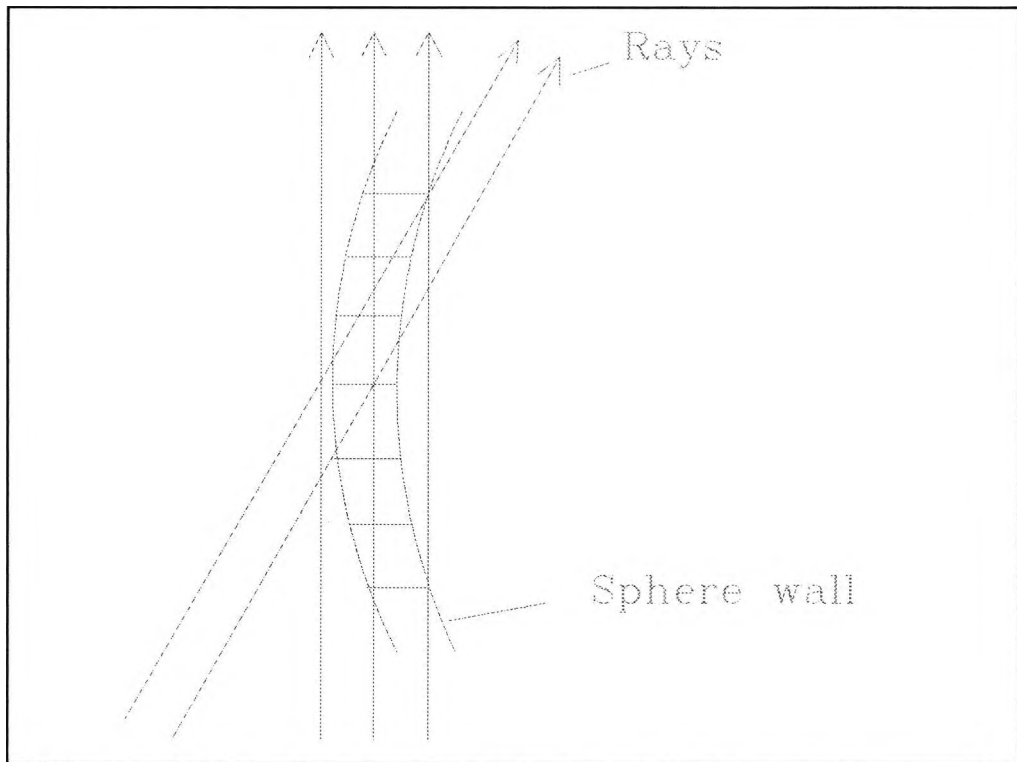shown in figure 41.

Figure 41 The rays passing through the side of the
hollow sphere.

The rays that pass through these areas can pass
through the middle of the sphere wall and come into
contact with many voxels, pass through just a single
voxel if sufficiently inclined to the sphere face, or
pass through no sphere voxels. That is three quite
different   cases   with   consequentially   different

information. However for the front and rear of the sphere rays pass through single voxels, as in figure 42, and thus rays contain a similar type of information.
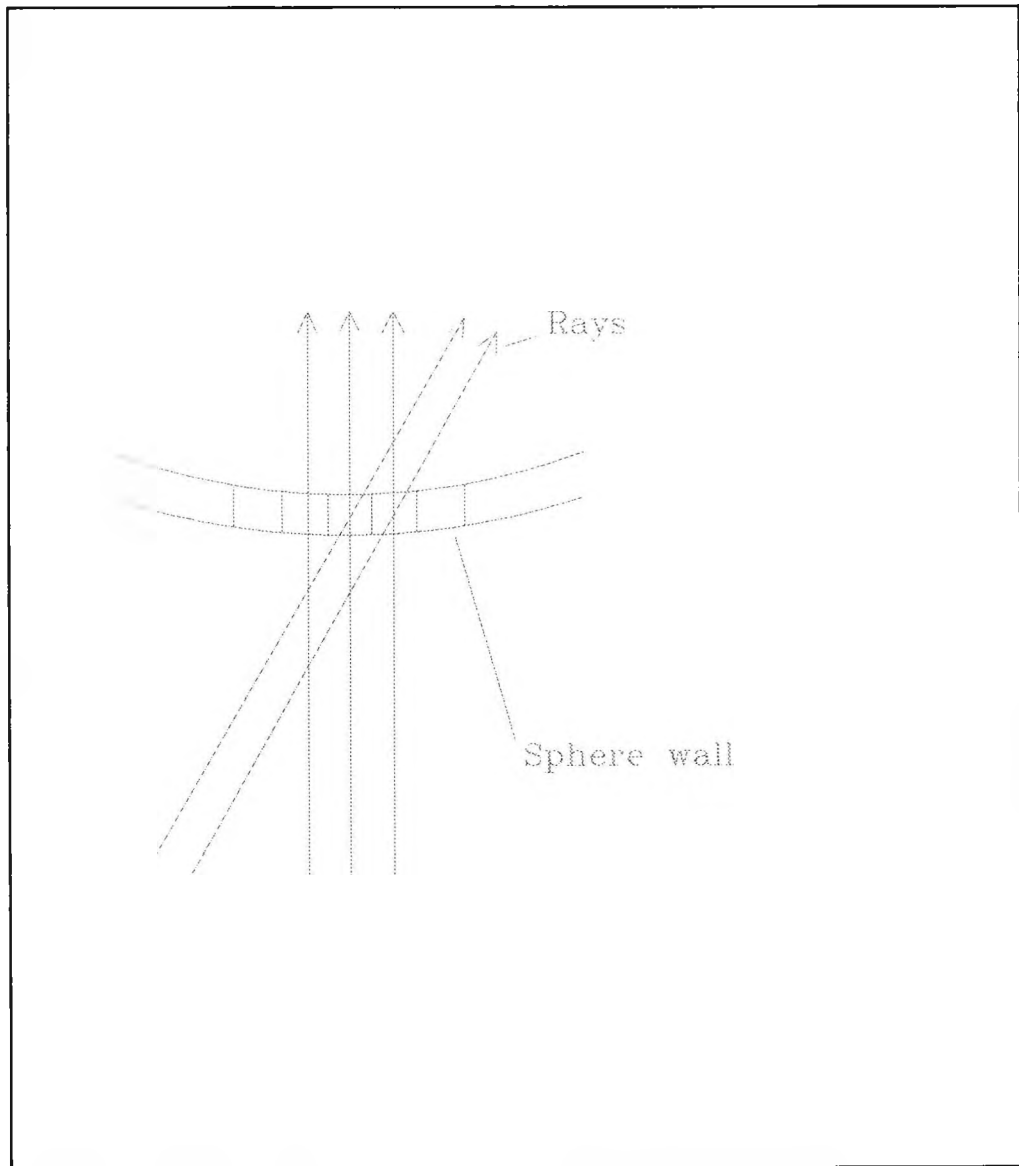

Figure 42 The rays passing through the centre of the sphere

It is this reduction in the variation of the information presented to the reconstruction algorithms

that leads to the loss of accuracy. It should be noted that the central section has accurately reconstructed the circular cross-section of the sphere, showing no geometric distortion.

The test figure was then reconstructed using a wider viewing angle of 0.45 radians. The results from this are shown in figures 43 to 46.
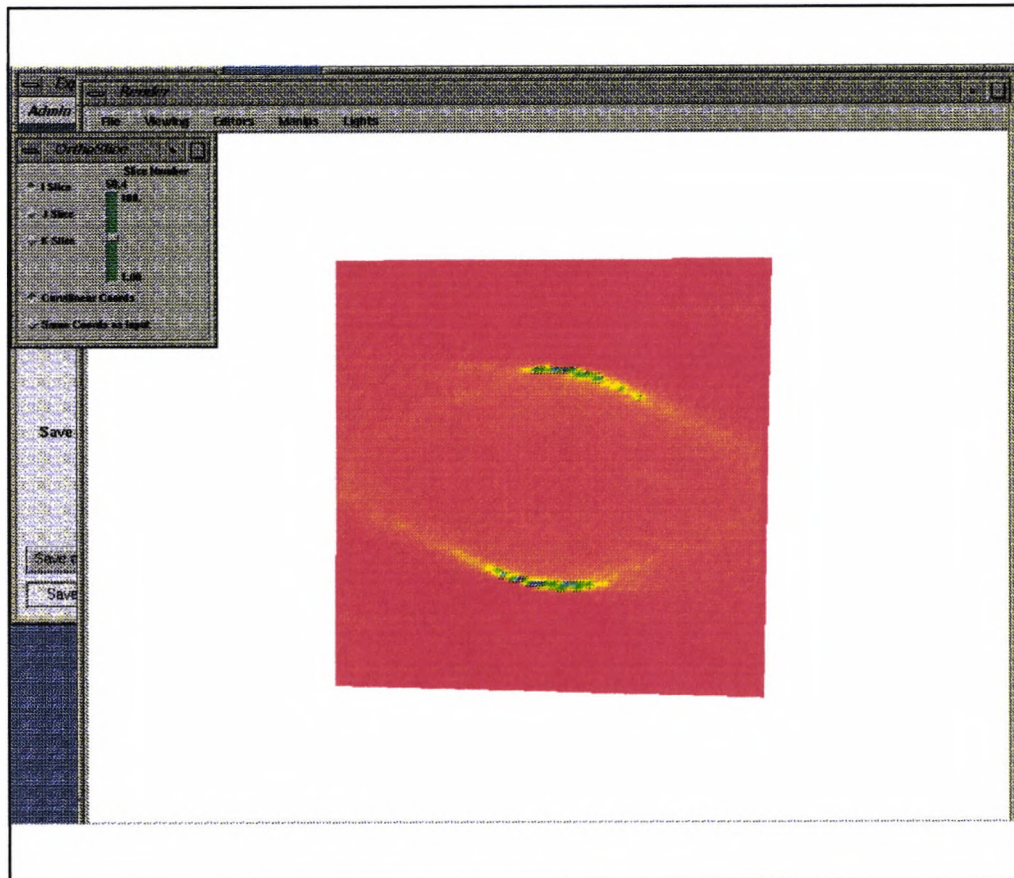
Figure 43 A vertical section parallel to the viewing direction through the sphere reconstructed from the 0.45 radian views
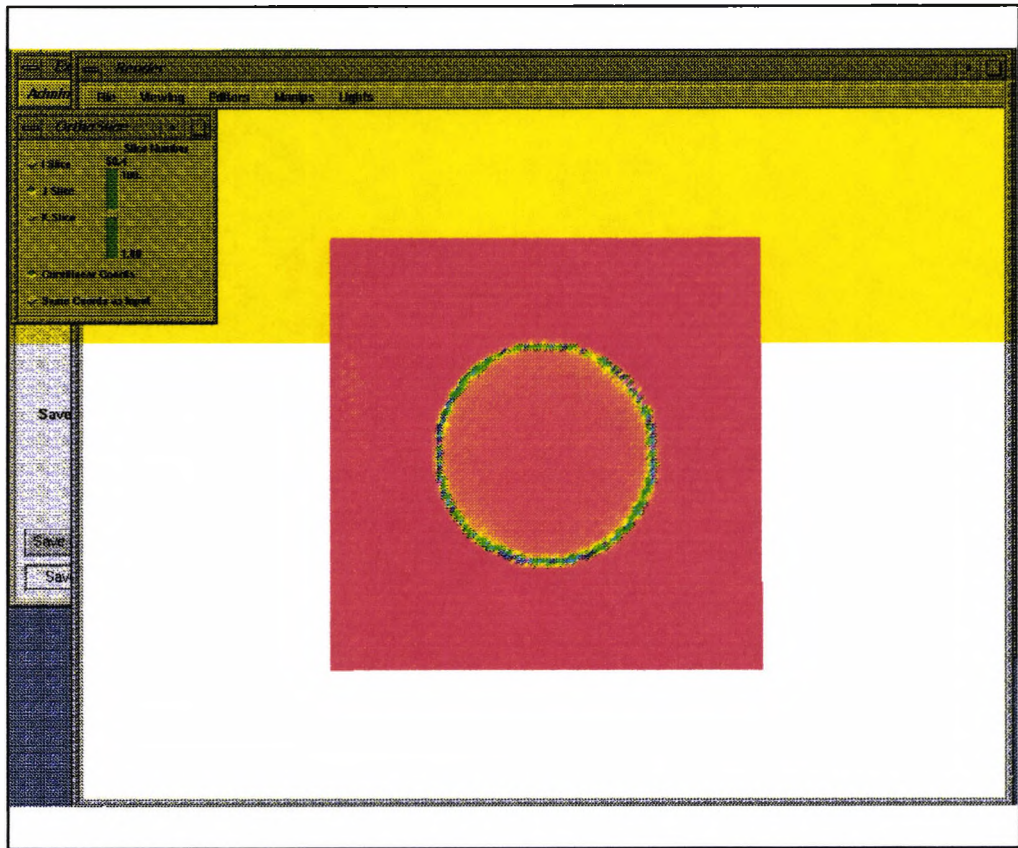
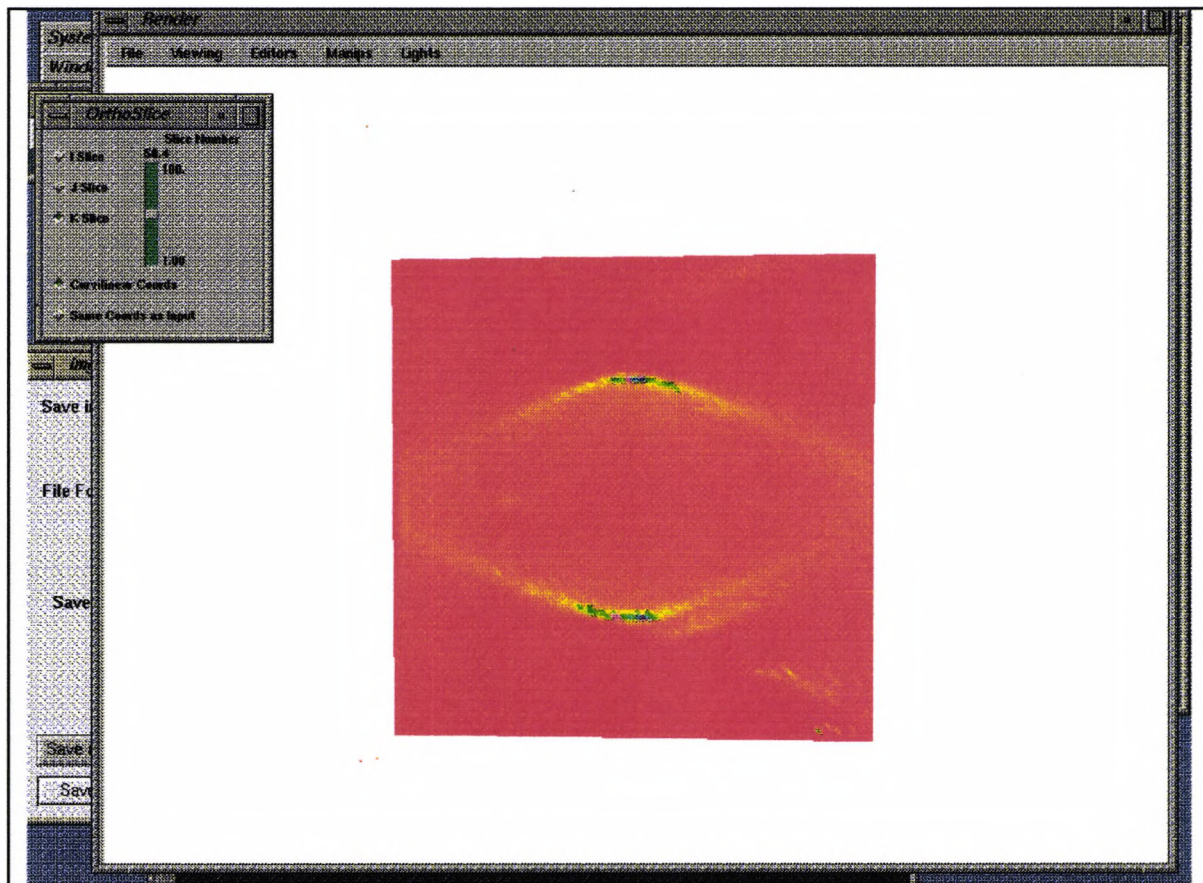**Figure 44** A vertical section perpendicular to the viewing direction

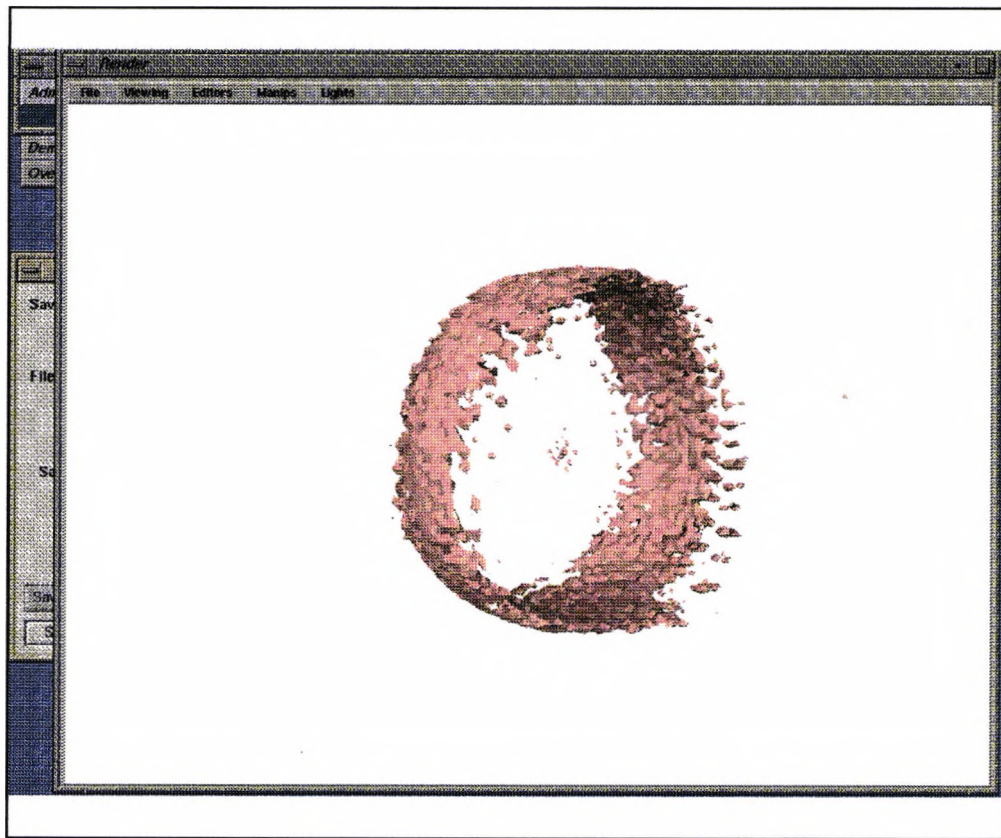**Figure 45** A horizontal section through the centre of the sphere

Figure 46 The iso-surface of the sphere reconstructed with a wider range of views.

Clearly the reconstruction is improved, as would be expected with a wider spaced data set. The front and rear of the sphere, (relative to the viewing direction), are still distorted due to the limited nature of the data, but the area where the reconstructed shell resembles the test object is increased. This can be seen in the iso-surfaced image where the shape of the reconstruction now resembles a sphere with front and end faces removed rather than a ring shape as previously. Similarly the orthographic slice parallel to the viewing direction shows a greater curvature at the top and bottom of the reconstruction fitting the test more closely. The stretching distortion in the viewing axis is reduced with the front and rear faces of the sphere closing toward each other at a steeper angle.

95

4.3.4 Sphere test object with variable internal density.

In order to test the effectiveness of our reconstruction techniques on three dimensional objects that have a variable internal density a spherical test object was produced that had an increasing density toward it's centre. In effect this test object was made up of a series of increasing value spherical shells, the outer shell having a density of 1 and a radius of 25 units, then a shell of density 4 units and radius 24 units, until the inner most having a density a 100 and radius 1 unit.

This test object was then reconstructed using both the ART and Gordon and Herman MART algorithm. As previously with the shell sphere test object tests were carried out using different sets of views of the object, one limited to views of up to 0.3 radians and one of up to 0.45 radians. By doing this the effect of increasing the angular range of allowed views could be studied.

4.3.5 Error comparison for the solid sphere reconstructions

As with our previous reconstructions the value of Performance Figure 1 at each iteration was recorded. Graphs of the variation of error against number of iterations were produced for the reconstructions and are shown in figures 47 to 50.

Considering the results for error across the whole field plotted against number of iterations in figures 49 and 50, the 0.45 radian data set gave similar shaped curves for both algorithms, with a steady reduction in error as the number of iterations increases. There is a significant difference in the

error level from the first iteration onward with the MART producing a significantly lower value. The final errors for the two are 1.39 for MART and 1.917 for ART. In contrast the 0.3 radian data sets produced an unexpected pattern for the change in the value of error as this initially rises with increasing iterations. The ART algorithm shows an increase in error between the first and second iteration before a gradual reduction for the following iterations. The MART algorithm shows a more accentuated form of this behaviour with the error level increasing until the seventh iteration, where it levels off and then starts to fall. This increase in error as the number of iterations increases would seem to be in contradiction to the reconstruction idea of improving each estimate of the field to be reconstructed at each iteration. It can be explained if we consider distortion present in the reconstructed object, which causes the reconstructed sphere to appear elliptical in cross section and occupy a significant amount of extra space in the solution field. Thus as the solution builds up over the iterations the density values lying in these incorrect locations increase, (at least for an initial number of iterations). This is especially pronounced for the 0.3 radian data set giving a rising error value.

Figures 47 and 48 look at the error levels in a 50x50x50 cube, which for this test figure is the volume that just surrounds the sphere. Figure 48 shows the convergence of the two ART reconstruction. The error for both of these starts at approximately the same level despite the wider viewing range for the 0.45 radian data set. However as the number of iterations increases the 0.45 radian reconstruction converges to a lower error value. The convergence of both reconstructions is stable and occurs after the

same number of iterations. Thus while the rate of solution is independent of the allowed viewing angle for this test the quality of the result is reliant on it.

Figure 47 shows the convergence of the Gordon and Herman MART solutions. Once again the error levels for both data sets start at similar values and as the number of iterations increase the error value for the 0.45 data set drops to a lower value. Comparing the results for both algorithms while the MART algorithm give a lower final value of 7.49 verses 7.95, for the 0.45 radian views. However the converse is true for the 0.3 radian solutions with final error values of 9.28 verses 9.03. Studying these graphs we can see that there is a reduction in reconstruction error when the wider view data is used as opposed to the more limited data set, as we would expect. The MART algorithm also performs better than the ART for the 0.4 radian data set, again as we would expect, giving lower error values for both error factors. However when the 0.3 radian data set is used while the ART algorithm performs better than MART.
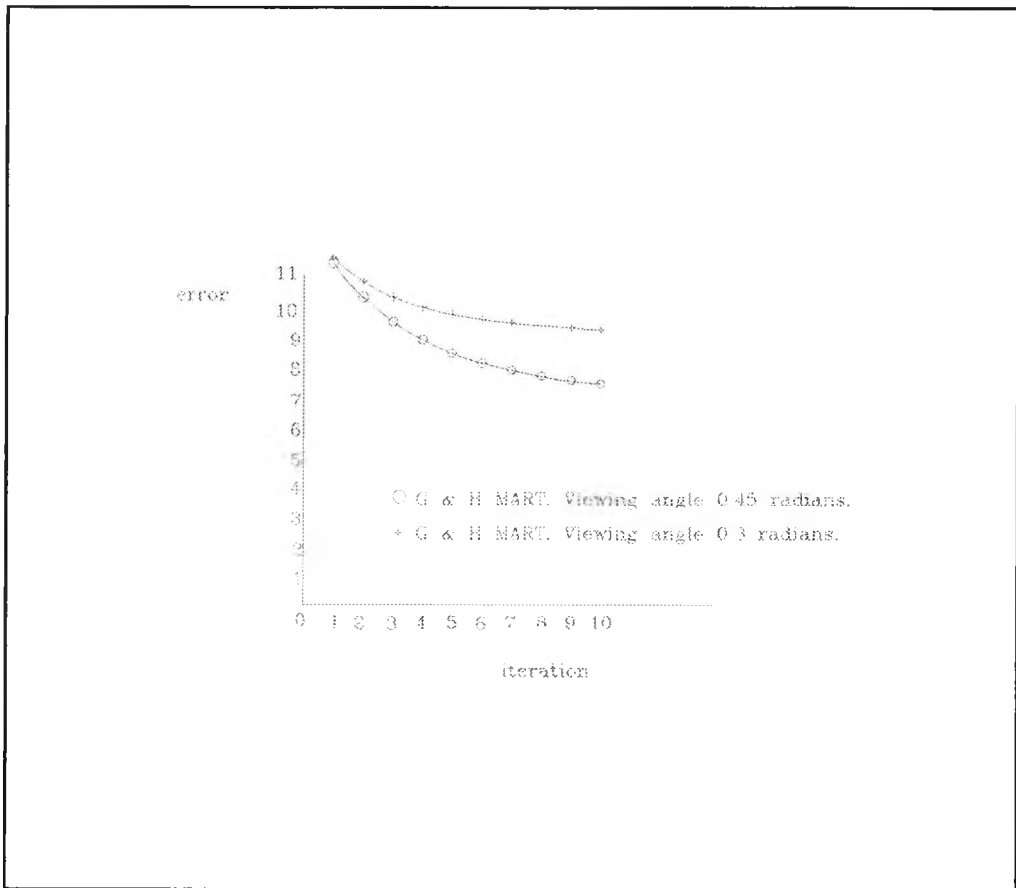
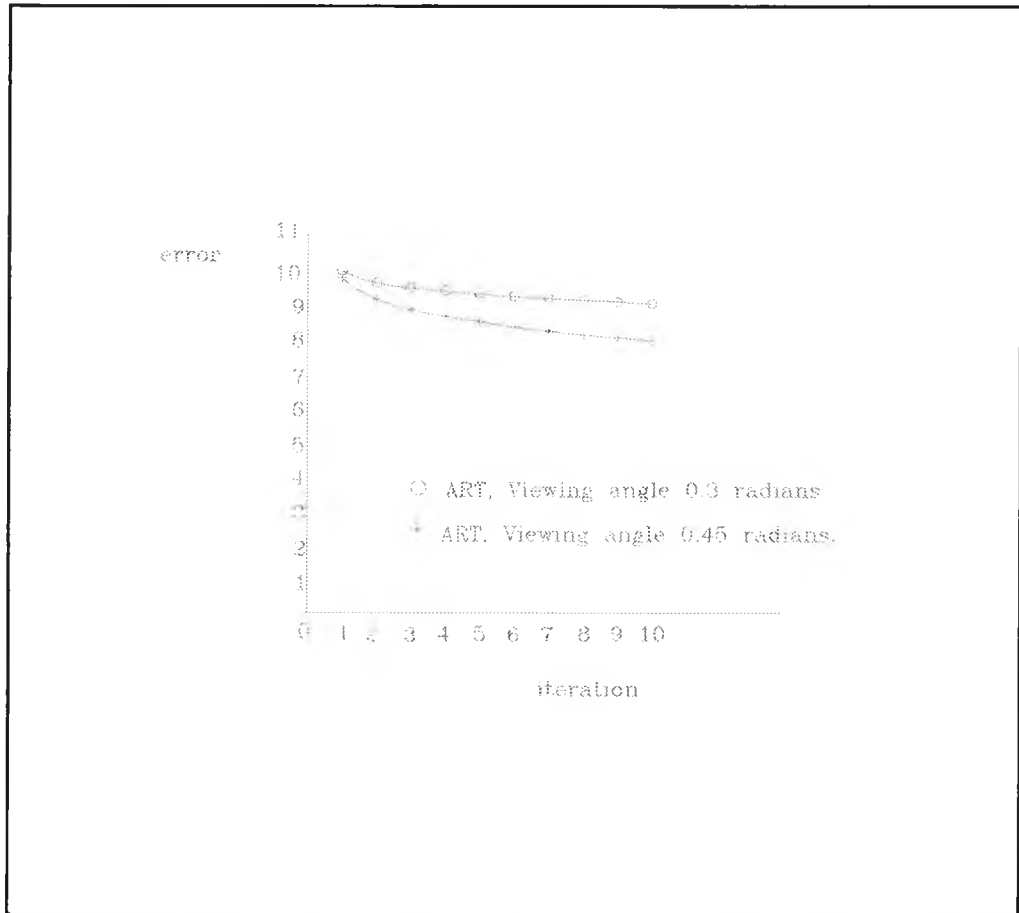**Figure 47.** The error curves for a 50x50x50 area produced by the 0.45 and 0.3 radian MART reconstructions.

Figure 48 The ART error curves in a 50x50x50 volume for 0.45 and 0.3 radian views.
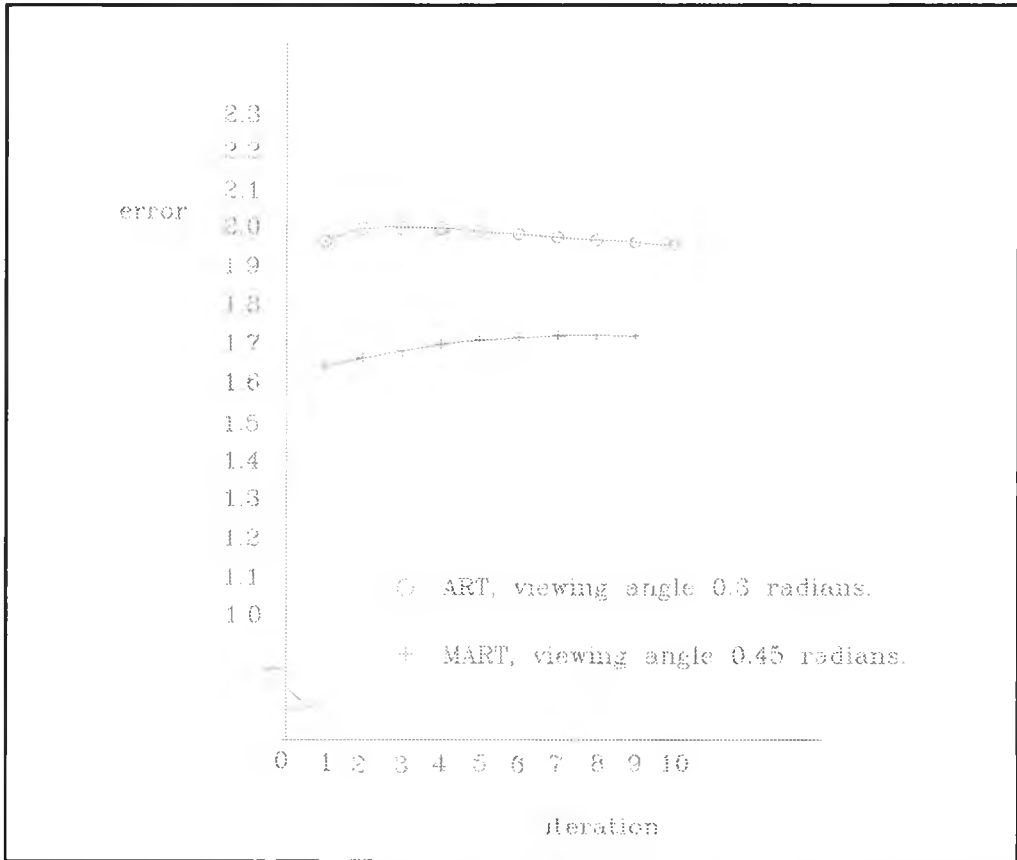
Figure 49   Error in the whole field when MART and ART are used with a viewing angle of 0.3 radians.
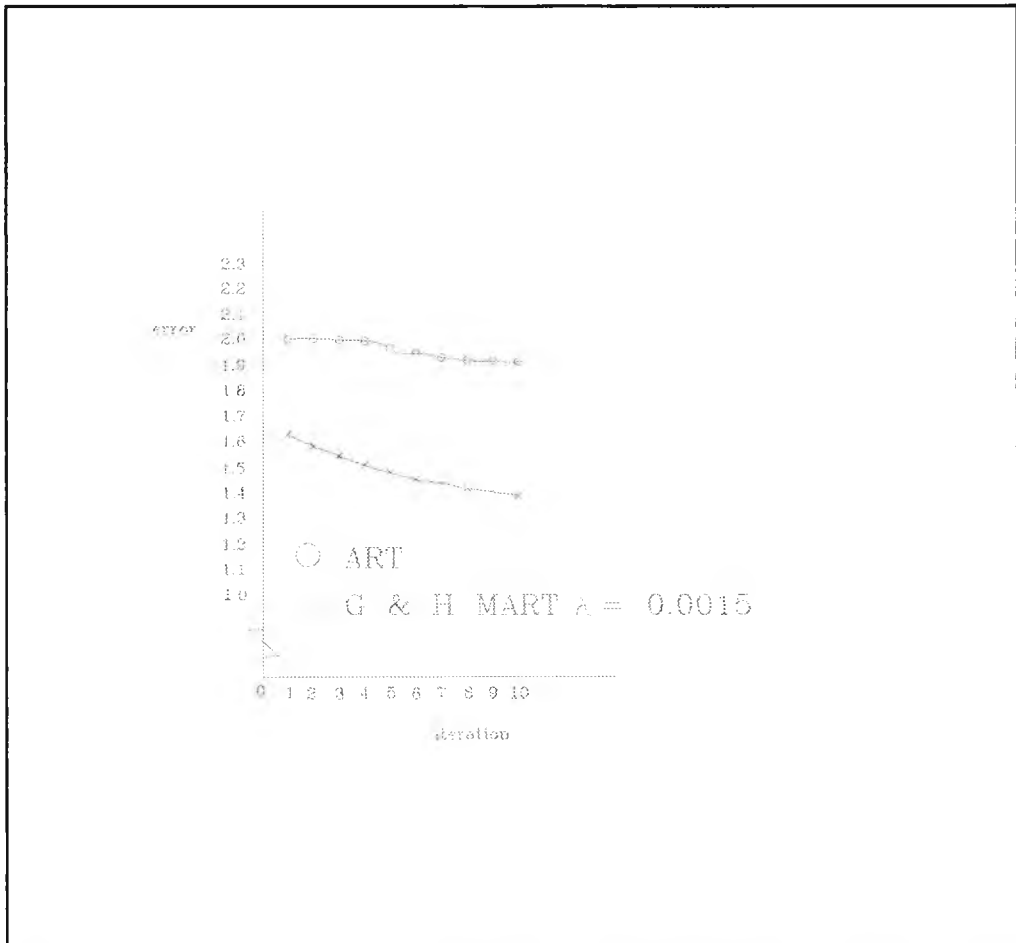
Figure 50. Error across the whole field for reconstructions using views of 0.45 radians.

4.3.6 Sectional views of the reconstructions

A series of sectional views of the solid sphere reconstructions were produced to enable the shape of the reconstructed field to be studied. These are shown in figures 51 to 62.

4.3.6.1 Variable density solid sphere reconstructed using the ART algorithm

The reconstruction was performed first on the variable density sphere used ART with viewing angles of + 0.45 and - 0.45 radians. Three cross sectional views of this were generated, each passing through the centre of the sphere in the x, y, and z axes. It can clearly be decerned from these that the reconstruction is distorted with an elongation of the sphere's shape along the viewing direction giving a oval shape. The cross sectional view perpendicular to the viewing axis show the sphere's circular cross section has been perserved. Another feature of this reconstruction is the appearence of spreading from the sphere at the extremes of viewing angle giving an "x" shape to the sectional views parallel to the viewing angle. The density of the reconstruction can be seen to increase towards it's centre.
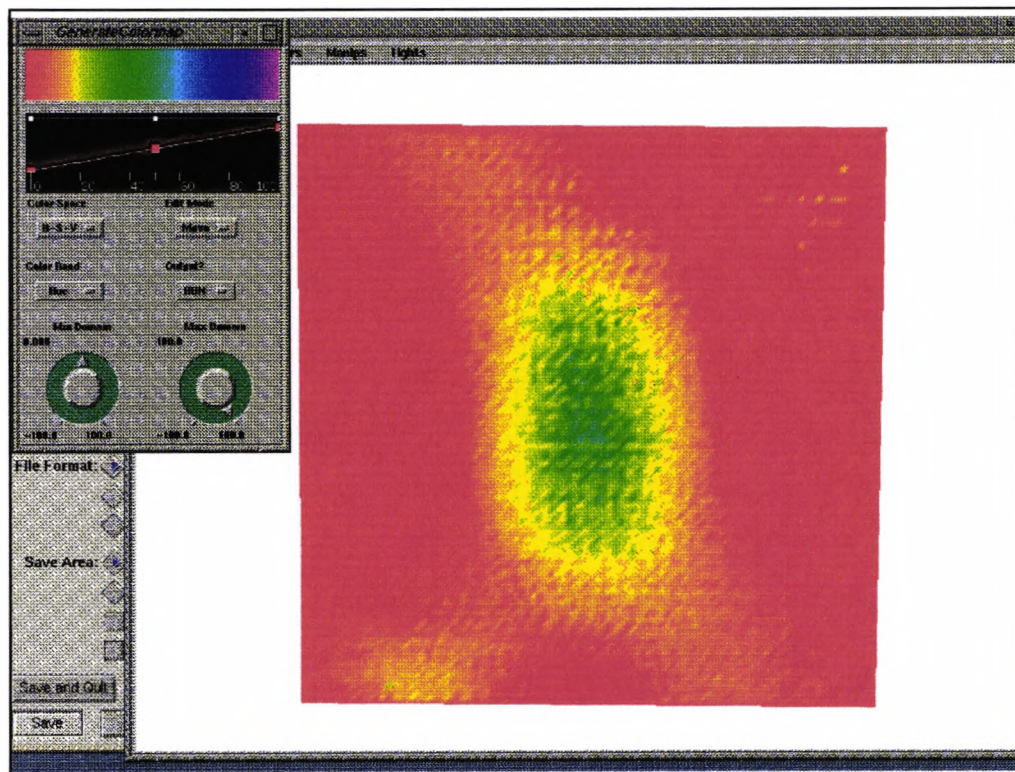

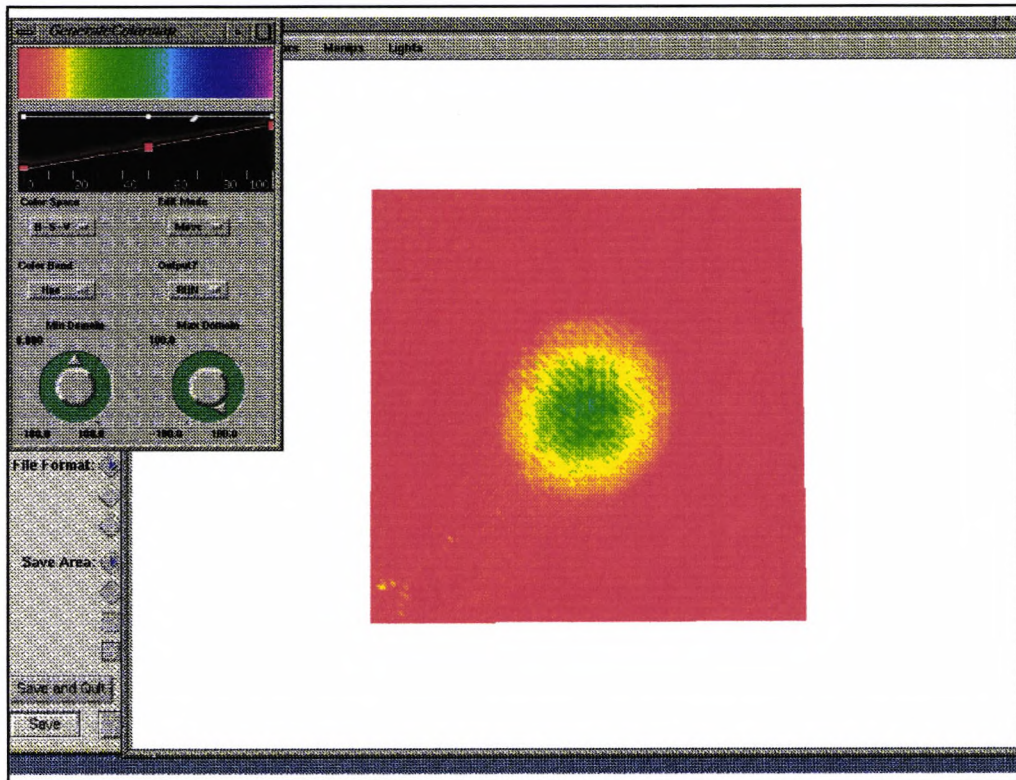**Figure 51** A section in the horizontal plane parallel to the viewing direction

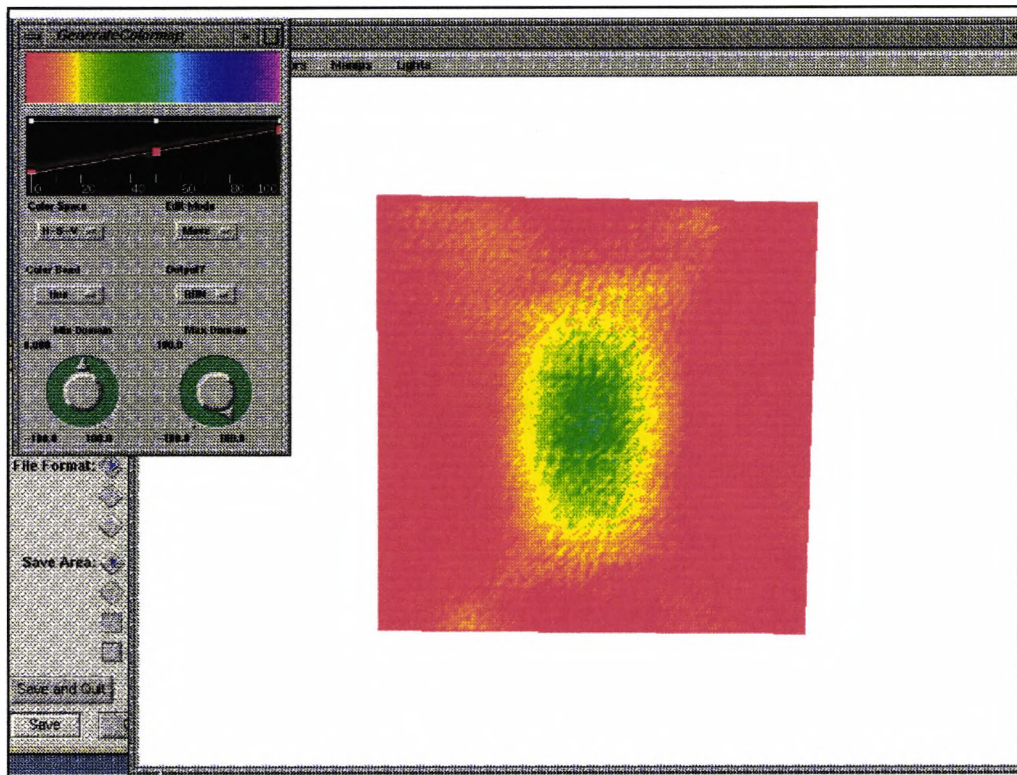**Figure 52** A section in the vertical plane perpendicular to the viewing direction

Figure 53 A section in the vertical plane parallel to the viewing direction

4.3.6.2 The MART reconstruction of the variable density sphere with viewing angle range +0.45 to −0.45 radians

In these three cross sections the feature spreading again gives an oval shape to the sections parallel to the viewing direction, but it is less noticeable than in the corresponding ART reconstruction. The density at the centre of the reconstruction has also reached higher values that are closer to thoses of the test object.
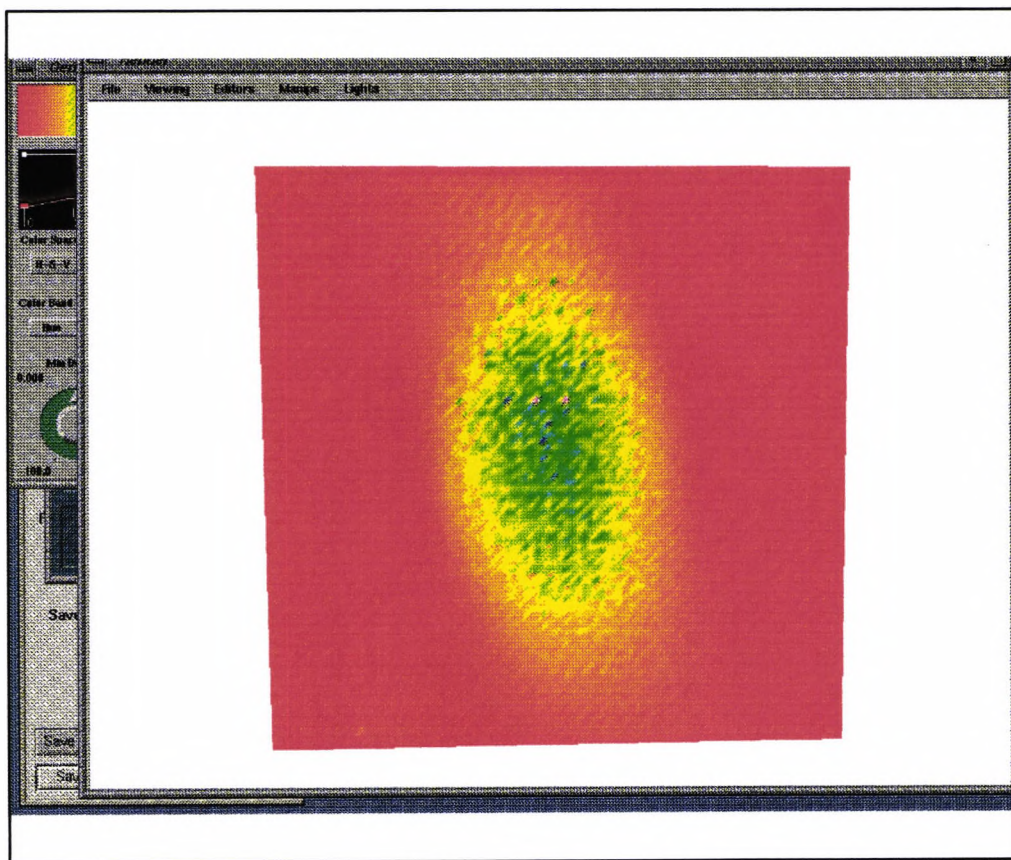

Figure 54 Vertical section parallel to reconstruction viewing direction
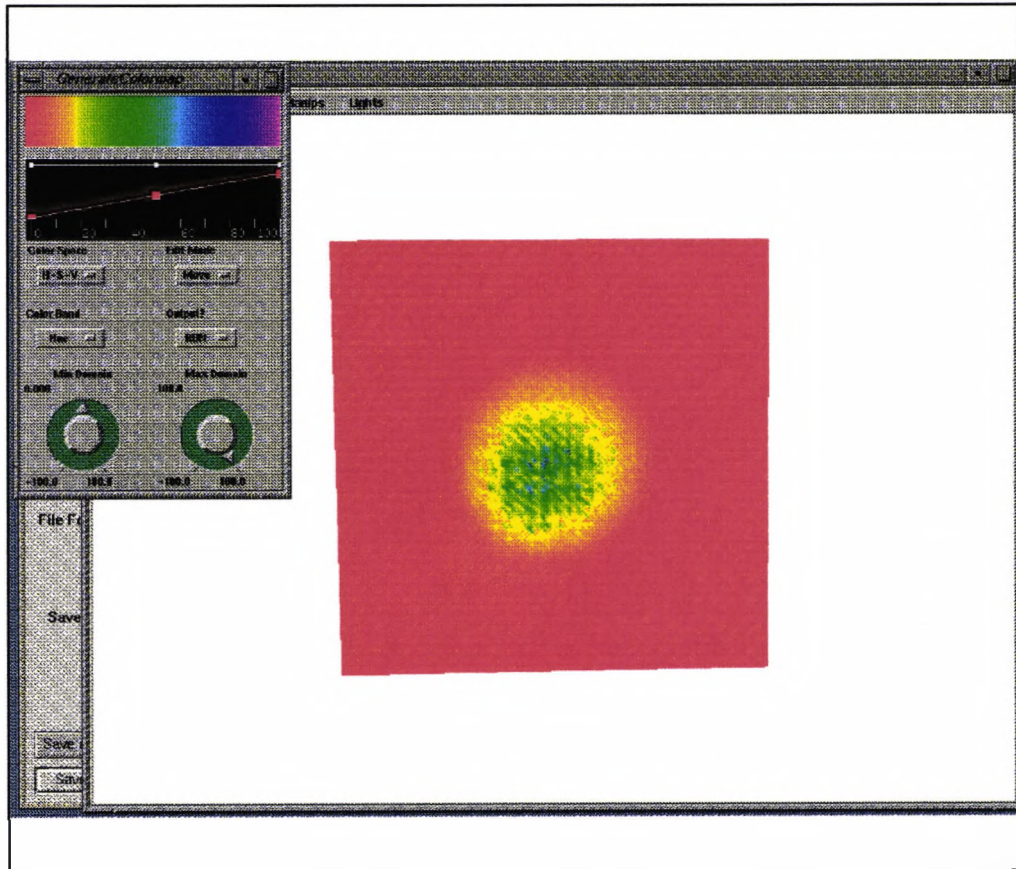
Figure 55 A section perpendicular to the viewing direction
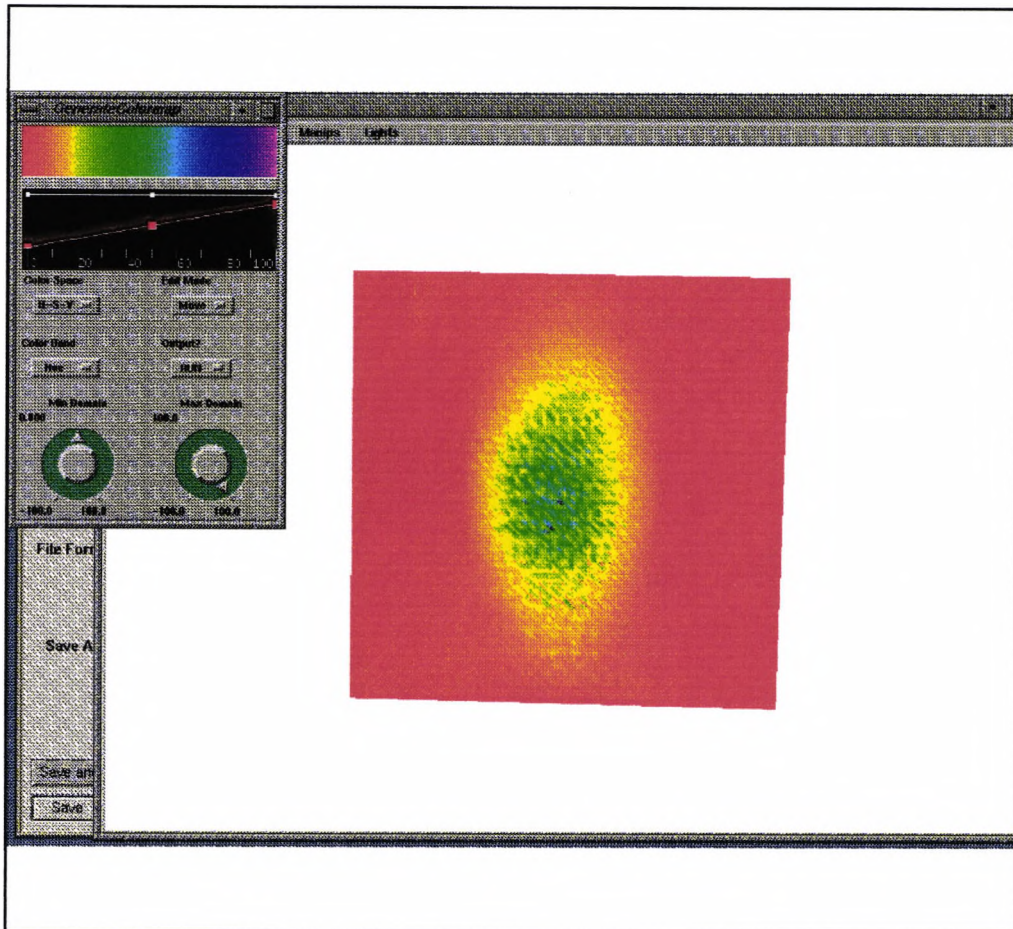
Figure 56 A horizontal section through the reconstruction

4.3.6.3 The ART algorithm reconstruction of the variable density sphere with viewing angle range +0.3 radians to –0.3 radians

Once again the reconstruction follows the same pattern as the previous one but as the viewing angle is reduced the feature distortion is more prenounced. The elongation of the sphere is increased to almost the length of the test field. It's circular cross-section is preserved in the viewing direction however.
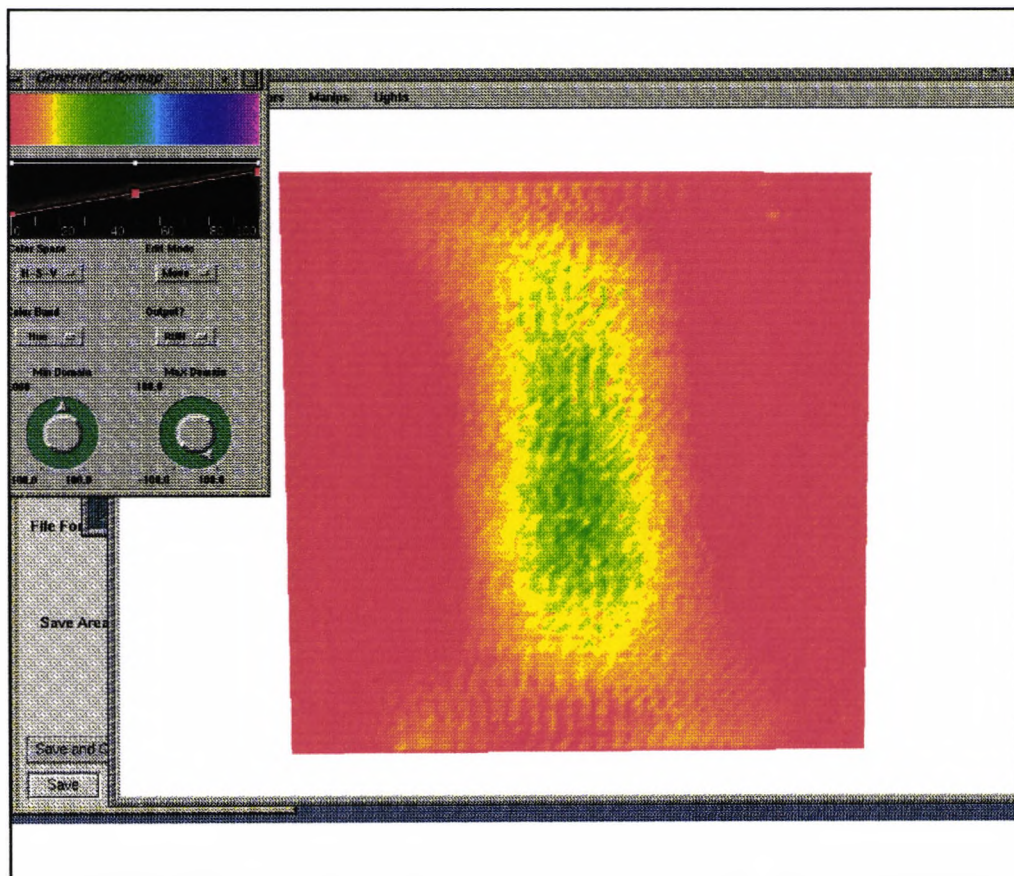
Figure 57 The vertical section through the centre of the sphere.
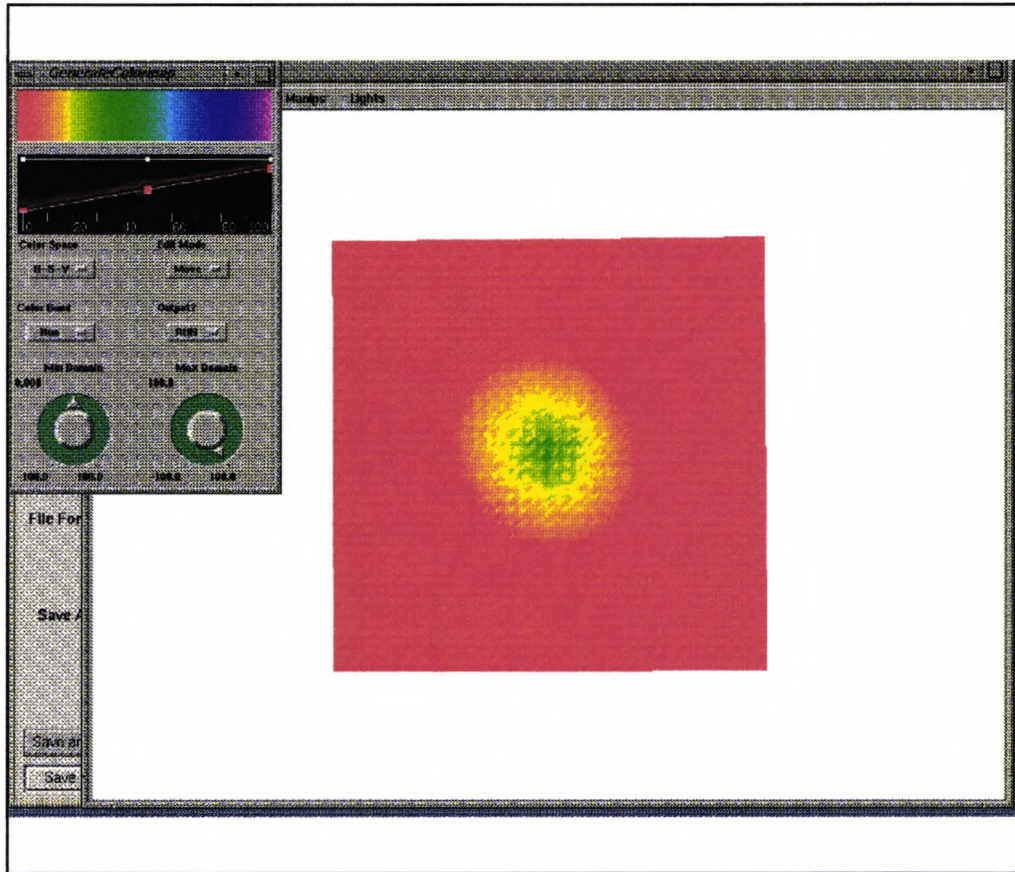
Figure 58 A section perpendicular to the view axis through the centre of the sphere.
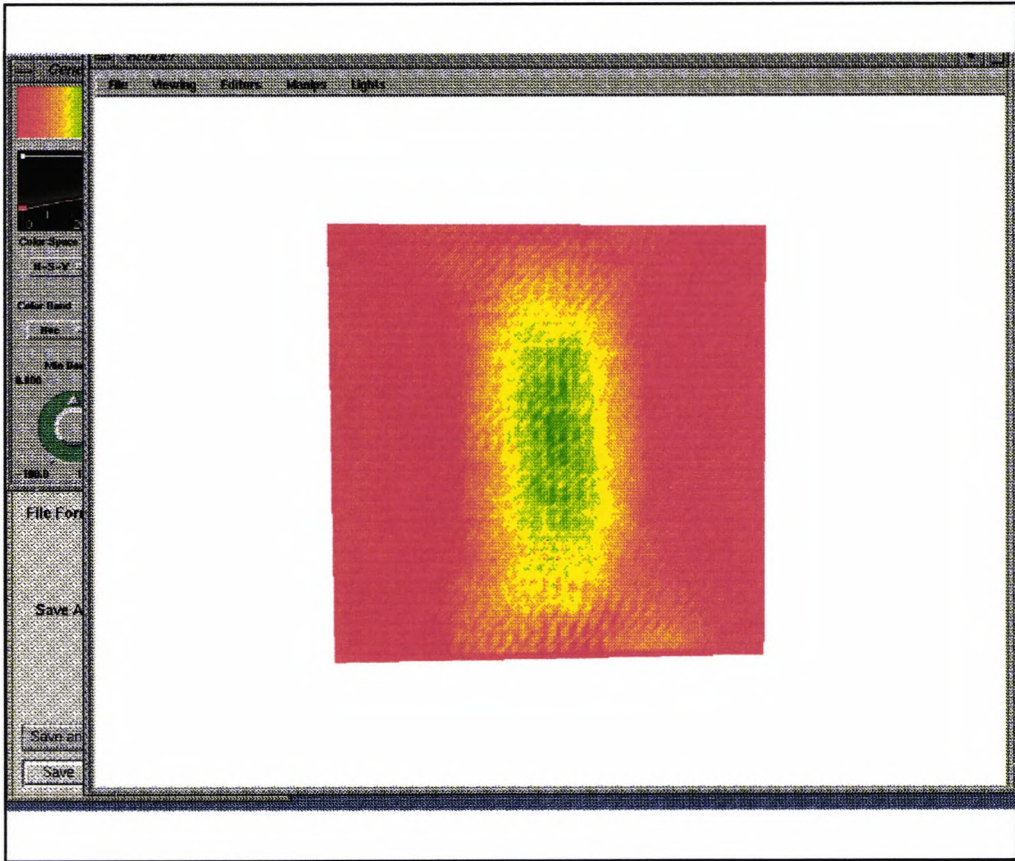
Figure 59 A horizontal section through the centre of the reconstruction

4.3.6.4 MART reconstruction of the variable density sphere for viewing angle +0.3 to -0.3 degrees

This reconstruction of the test object is clearly inferior to that produced by the MART algorithm using the wider viewing angle data set. The erroneous elongation of the field is greater as we can see in the figures 60 and 62. The circular cross section of the sphere for the section perpendicular to the viewing direction is however still preserved as in figure 61.

Figure 60 Vertical section along the recontruction direction.

Figure 61 A vertical slice perpendicular to the viewing direction.

Figure 62 A vertical slice parallel to the viewing direction.

In all of these views we see fields density increases toward the centre of the object, correctly reproducing this feature of the object. The ART reconstruction has less convergence to the correct central density than the MART version and thus again MART has proved more effective. In terms of the reproduction of the spheres shape both algorithms accurately reproduced the circular cross section of the sphere in the perpendicular direction to the viewing cone. The noticeable elongation along the central axis,
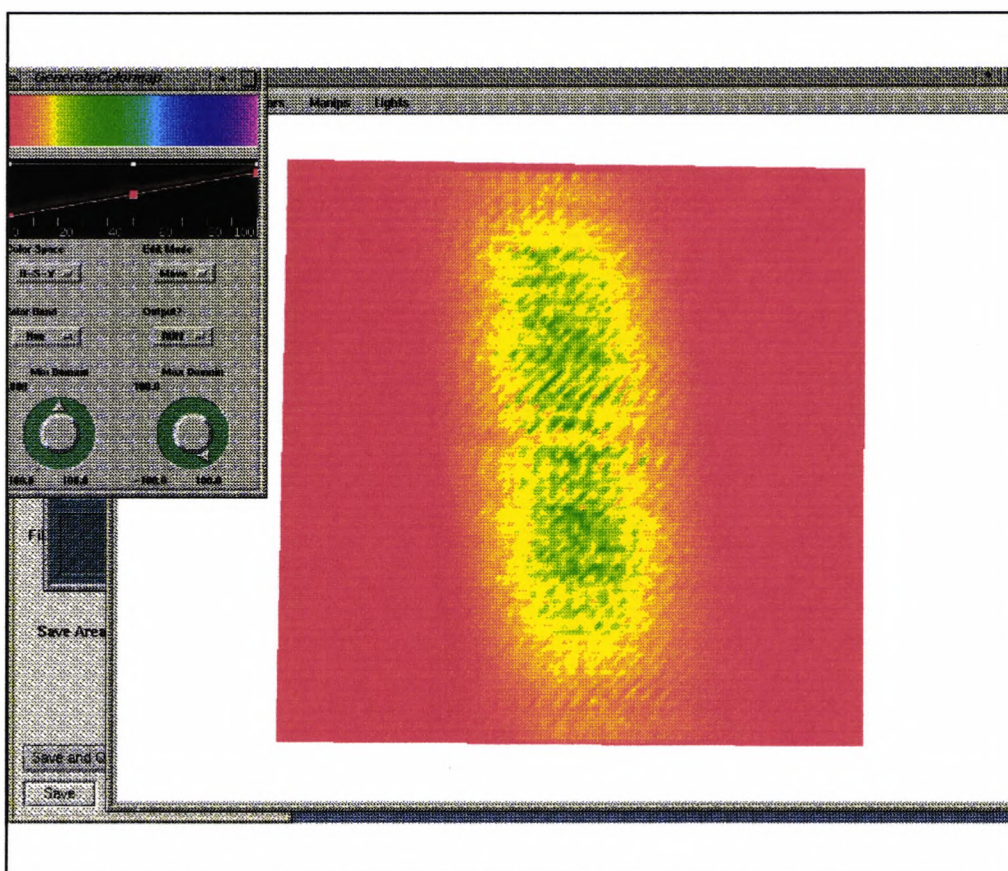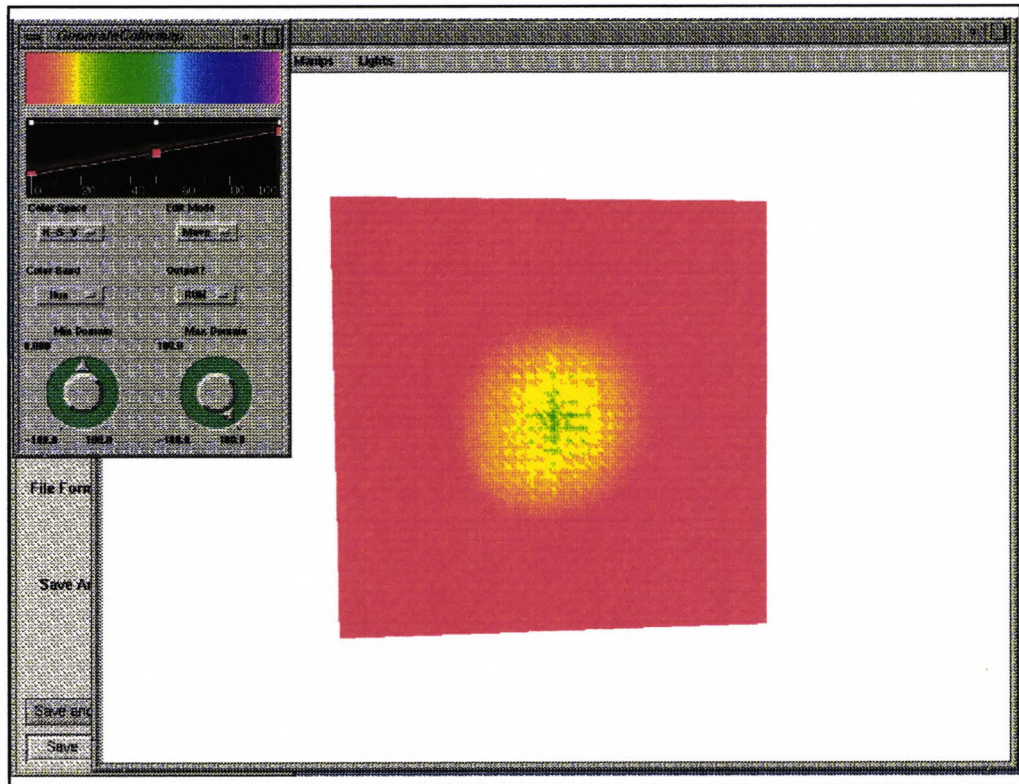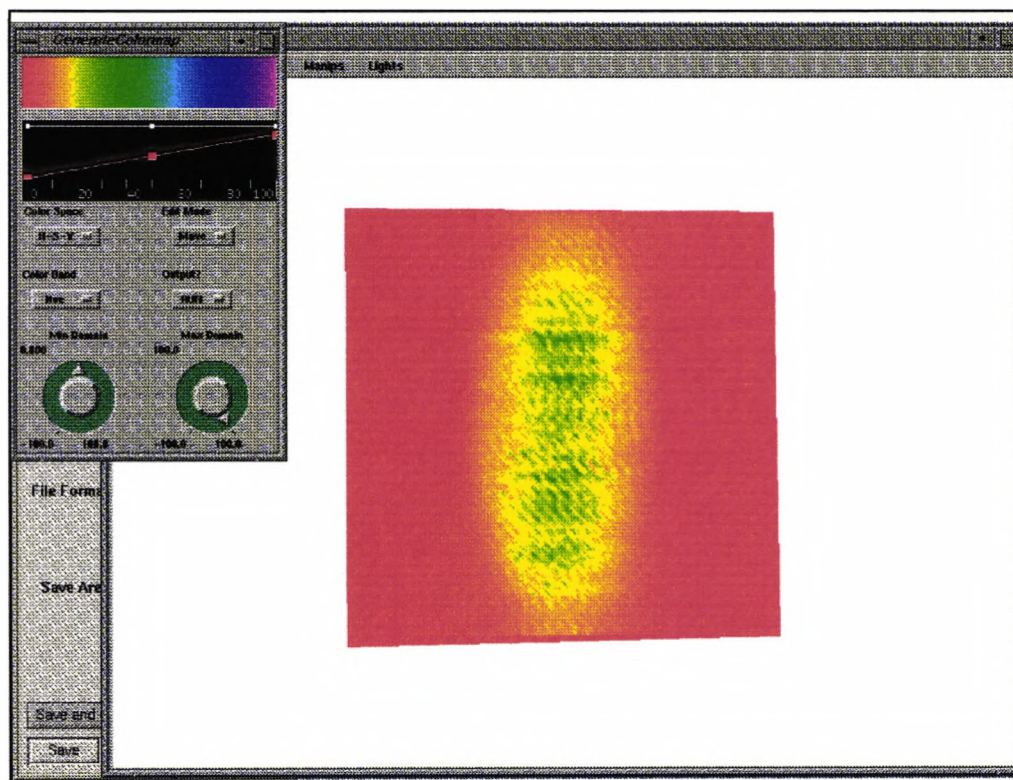parallel to the viewing direction, is caused by the lack of information from the direction perpendicular to the axis to confine this spread. This effect is reduced in the sections from the wider viewing data sets, as of course we would expect.

4.4 Summary of algorithm comparison

The results of the comparative tests can be summarised as follows:

The ART algorithm proved robust needing the minimum of modification for specific problems, but tended to smooth out sharp features in the reconstructions. The Lent MART algorithm produced reconstructions that reproduced sharply changing features but also introduced spurious features. It also required the tuning of the relaxation factor for specific problems. The Gordon and Herman MART algorithm proved superior to both of the algorithms in confining reconstruction feature to the correct position and in the accuracy of the individual values in the reconstruction, it did however require the setting of the relaxation factor which is found on trial and error basis.

5.0 Comparative Tests of the Projection Schemes

To test the potential benefits of our 3-D projection scheme a series of comparative tests between it and the 2-D slice approach were made.

5.1 The cross planes

The first test object reconstructed using the 2-D scheme was the crossed planes model. This was reconstructed using the ART and Gordon and Herman MART algorithms in conjunction with the two projection methods in order to observe any effects caused by the interaction of projection scheme and algorithm. The 2-D slice reconstructions were produced using our tomography system with the computer program altered so that one of the two variable angles used for the 3-D scheme was made constant. Iso-surface figures of these 2-D reconstructions are shown in figures 63 and 67. In both figures it can clearly be seen that the horizontal plane has been severely distorted during the reconstruction process, while the vertical plane has been reconstructed relatively accurately. As the slices used for the reconstruction lay in the horizontal plane it can be deduced this caused less useful information to be available to the reconstruction process the parallel plane. This lack of information causes the horizontal plane to spread along the viewing direction so that the extremities of the plane reach the boundaries of the field. It is also noticeable that this distorted plane tapers at an angle corresponding to the direction where the sampling rays intersect the corners of the plane. Thus where there is sufficient data to constrain the spread of the plane, i.e. from the sampling rays that by pass the plane and experience zero attenuation, the 2-D projection schemes was operation was sufficient.

5.1.1 Slice reconstructions of the cross test object using the ART algorithm

A slice reconstructions of the cross test object was performed and the resultant reconstruction is shown iso-surfaced below.
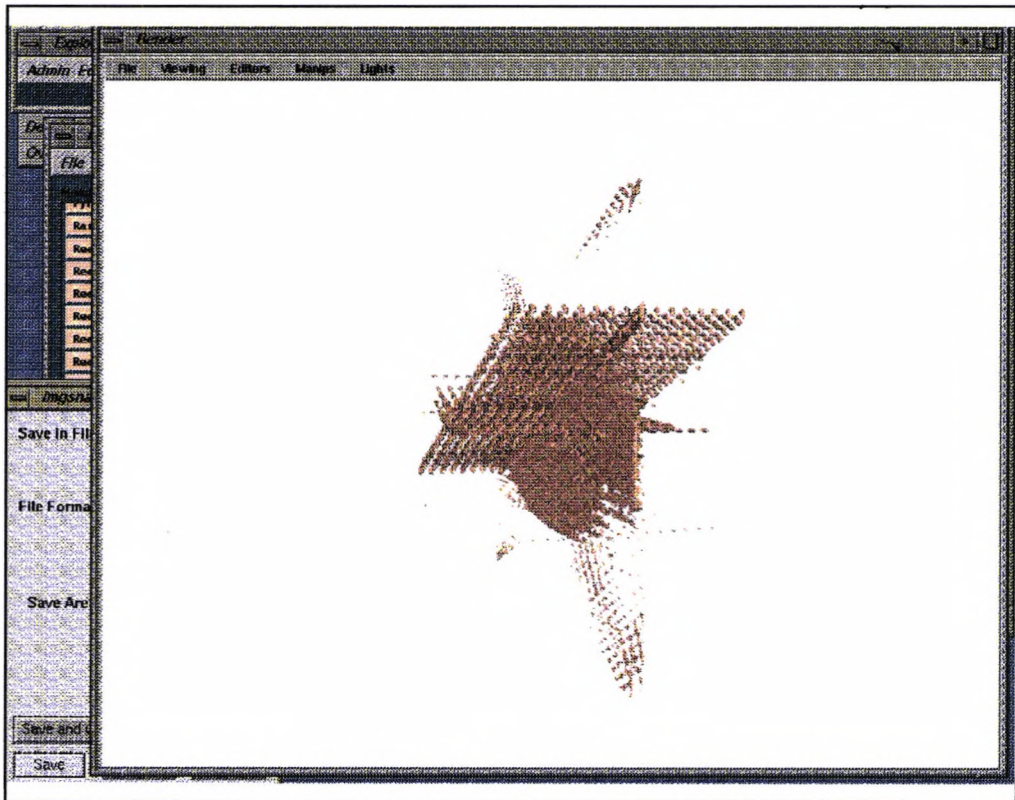
Figure 63 An iso-surface of the slice reconstruction of the cross test object, using the ART algorithm

It is immediately noticable that the test objects shape has been badly distorted. This reconstruction was also visualised by taking orthographic slices through it, allowing the distortion of the planes to be viewed in the x,y and z directions.

Figure 64 below is cut parallel to the vertical plane directly through it's centre. It shows how the slice reconstruction has distorted this square shaped feature into an almost diamond shaped one. This face is the one parallel to the slices used to reconstruct

117

the field. Thus the ray paths used to reconstruct this
feature all lie in the same plane as it with no out of
plane information being used to reconstruct it.
Because of this there is insufficient data to confine
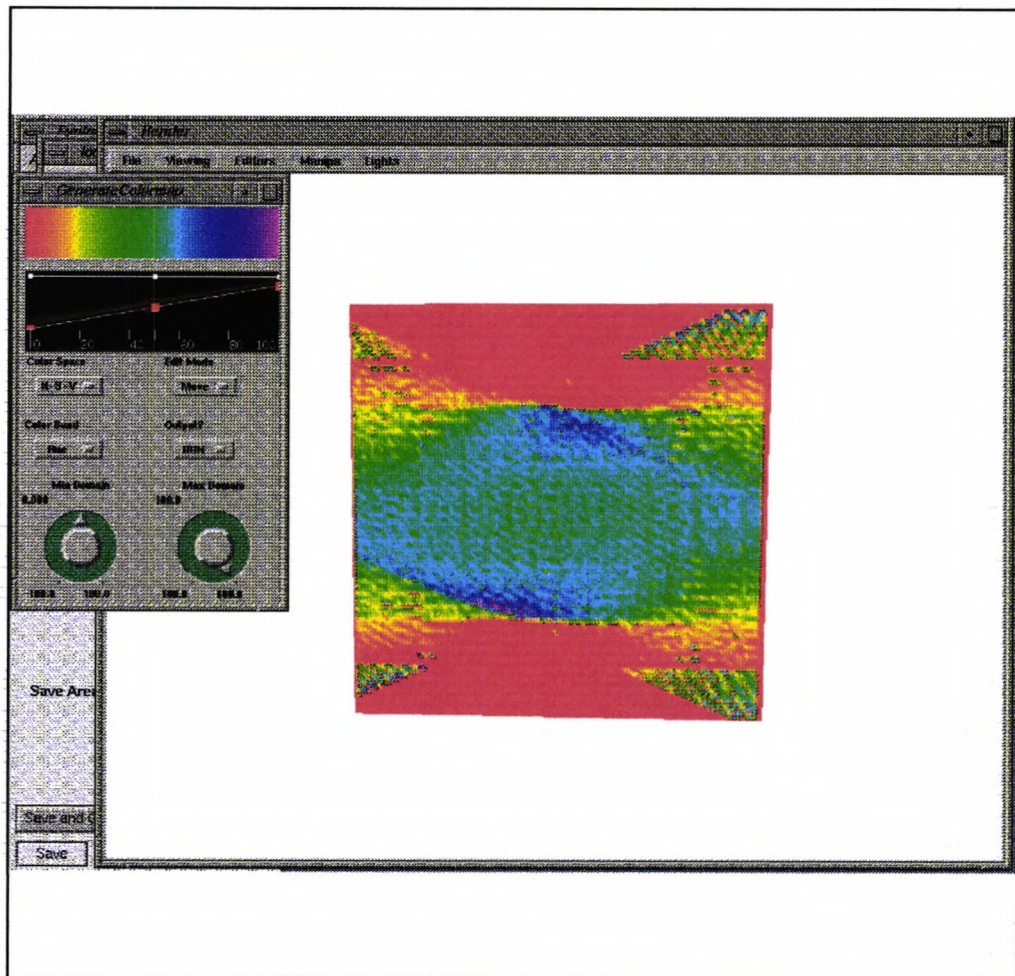
Figure 64   The slice through the vertical plane

the feature to it's correct square outline.

The section perpendicular to both planes shows the
cross out line has been preserved. However the final
section, figure 66, parallel to the horizontal plane
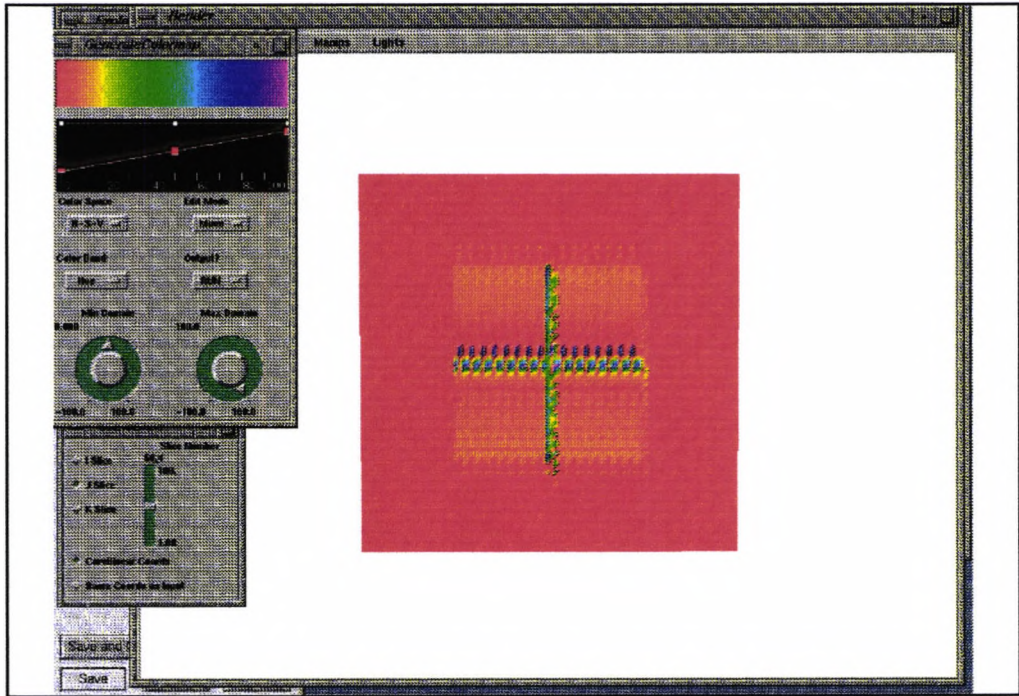
Figure 65 The section cut perpendicular to the viewing direction

also shows some distortion, the vertical plane spreading along the field with a thin central band at the centre of the planes location.

Figure 66 The section through the horizontal plane

The 3-D ART reconstructions for comparison.
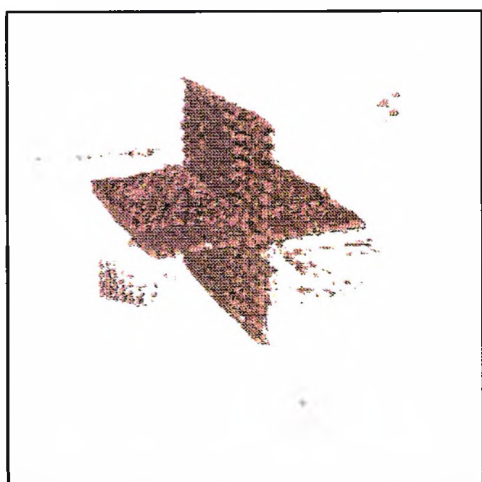
Figure 67 The iso-surface
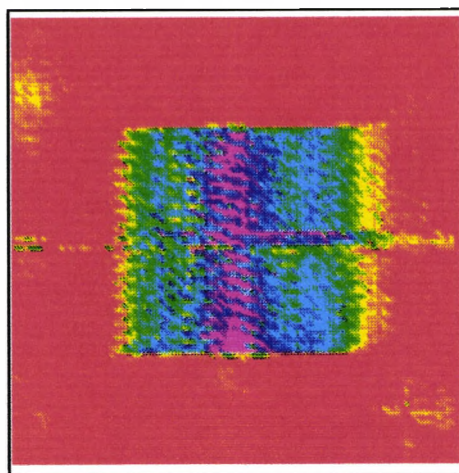
Figure 68 Vertical section
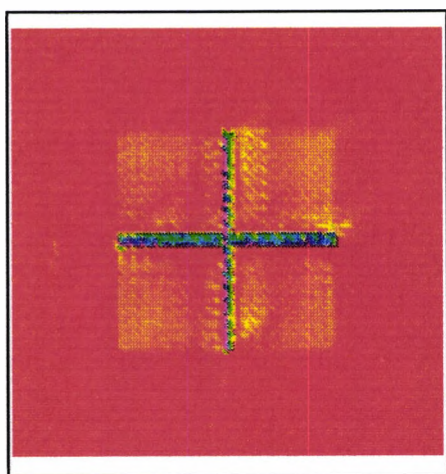
Figure 69 Section perpendicular to viewing direction
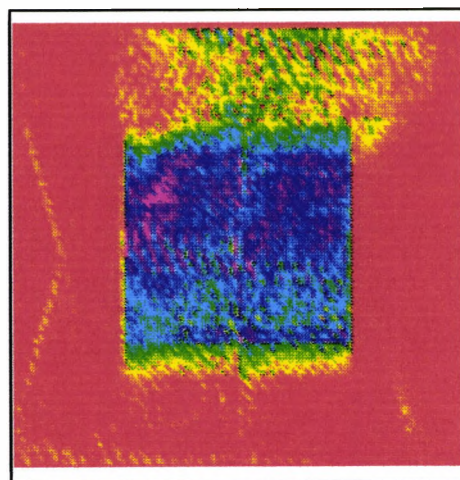
Figure 70 Horizontal section

A numerical measure was made of the relative effectiveness of the two projection schemes. The error present in the reconstructions at each iteration was measured and are shown in figures 71 and 72, comparing the ART and MART results separately.
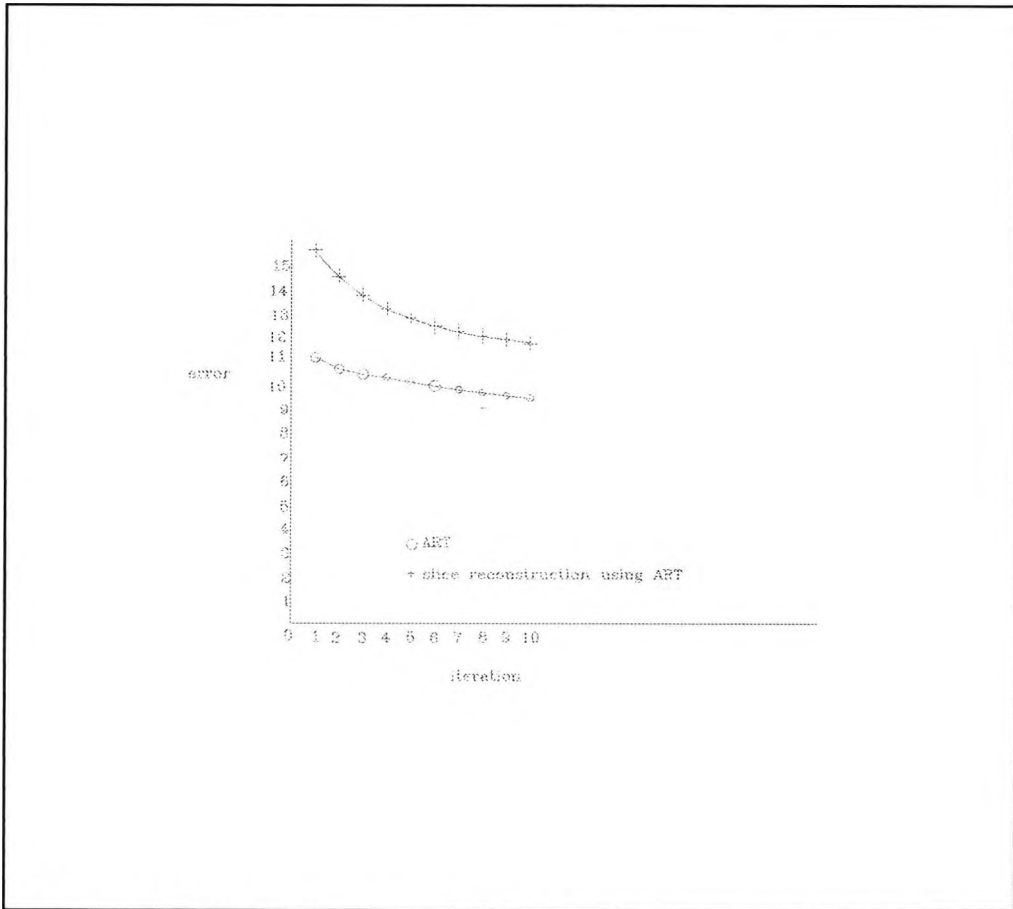
Figure 71 The slice reconstruction compared to the 3-D technique for the ART reconstructions

In both graphs the 3-D projection scheme shows significantly less error at each iteration. The Gordon and Herman results for the slice and the 3-D projection schemes respectively were lower than the ART values, as we would expect. Importantly the 3-D ART reconstruction had a lower error value than the Gordon and Herman slice reconstruction at every point in the reconstruction process, thus for this test figure the projection scheme used was a more significant the algorithm used. A point borne out by the iso-surfaced figures where the 3-D scheme gave

121

clearer definition over the 2-D regardless of algorithm.
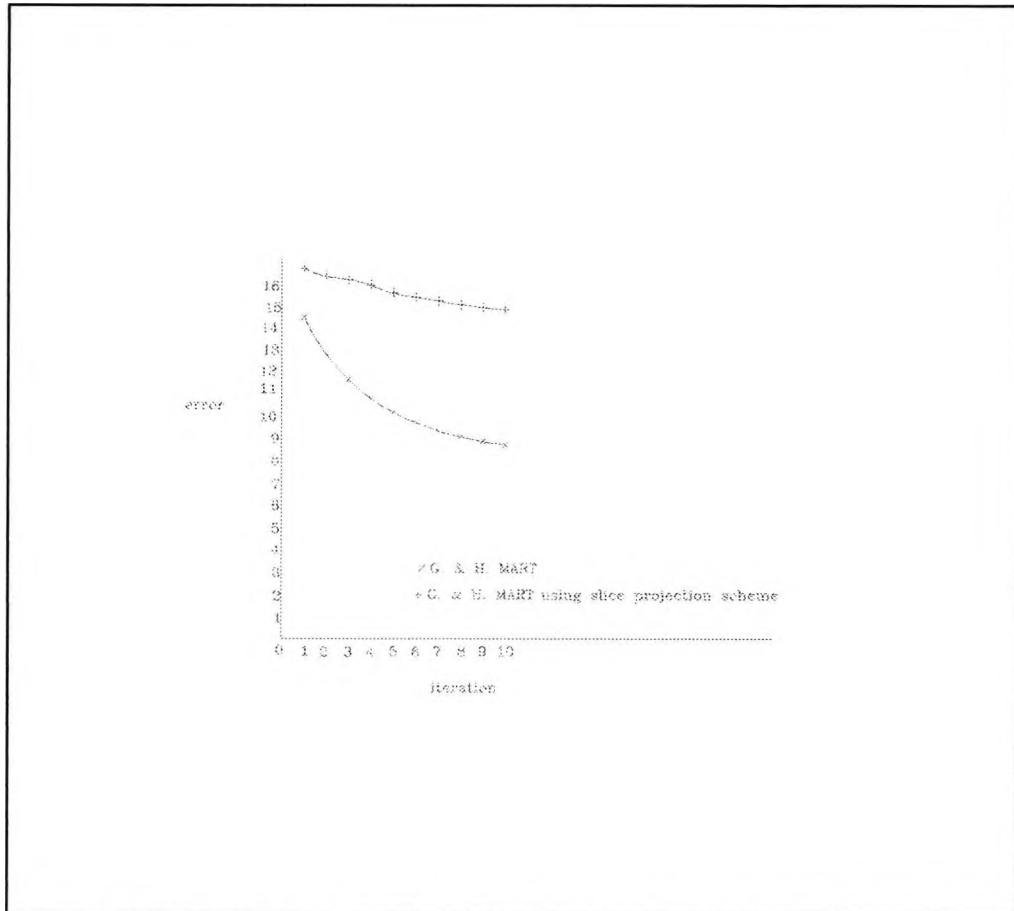
Figure 72 The slice reconstruction compared to the 3-D for the MART algorithm

Having demonstrated the superior performance of the 3-D scheme using the cross test object comparative reconstructions were then performed on spherical test objects.

5.2 Spherical test object comparative reconstructions

The spherical test objects used previously, i.e. the hollow sphere and the variable density sphere, were now tested with the slice reconstruction method.

The hollow sphere test object was considered first and these results are illustrated below in the form of iso-surfaces and orthographic slices.
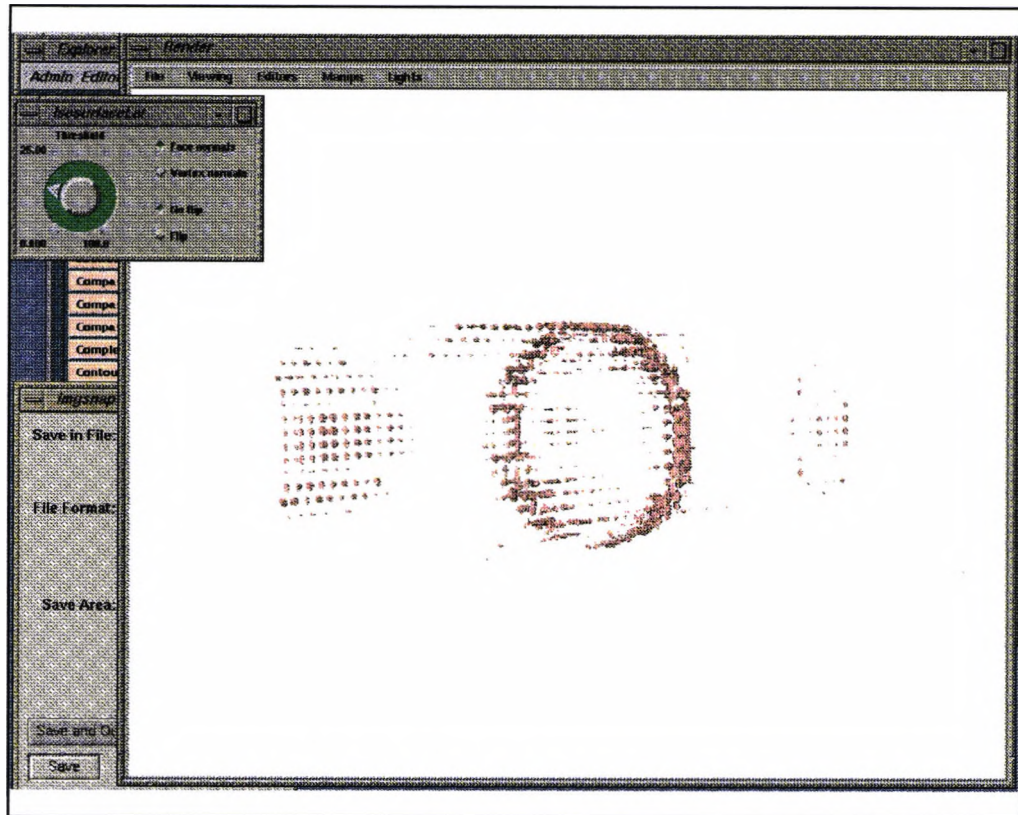
Figure 73 The iso-surface figure of the slice reconstruction of the test sphere.

In this iso-surface of the reconstruction, figure 73, the only remaining recognisable feature of the original spherical shell is a circular ring shape that corresponds to the outside diameter of the sphere when viewed end on. The sampling rays incident on that portion of the sphere would have been tangential to the surface and it is these rays which contained sufficient information to give a detectable ring structure. When compared to the results produced by the three dimensional projection scheme we have the same general loss at the front and rear of the sphere

123

but has an extra distortion in the form of two facets introduced at the front and rear of the field.

The orthographic slice through the centre of the reconstruction, figure 74, shows the ring structure which was visible in the iso-surfaced image.
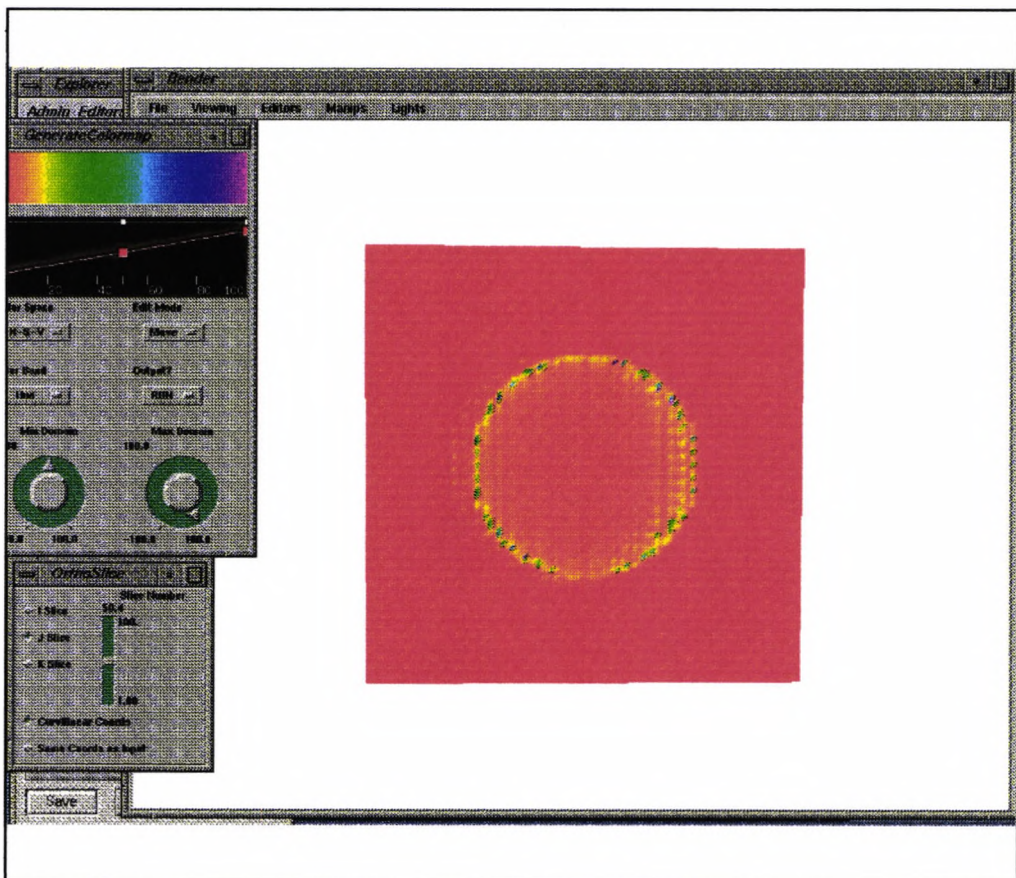
Figure 74 The orthographic slice through the sphere perpendicular to the viewing direction

An orthographic slice view of the figure in the horizontal plane was also taken and this is shown in figure 75.
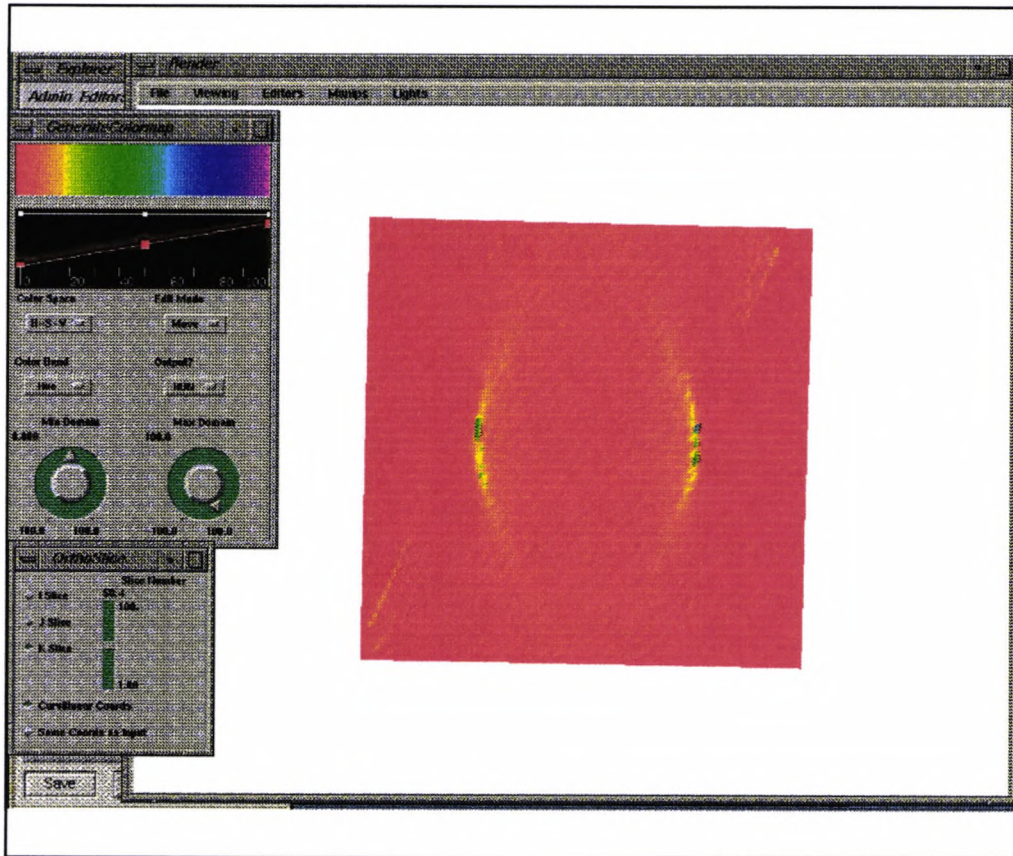
Figure 75 A horizontal slice through the centre of the sphere

and also in the vertical plane as shown in figure 76.
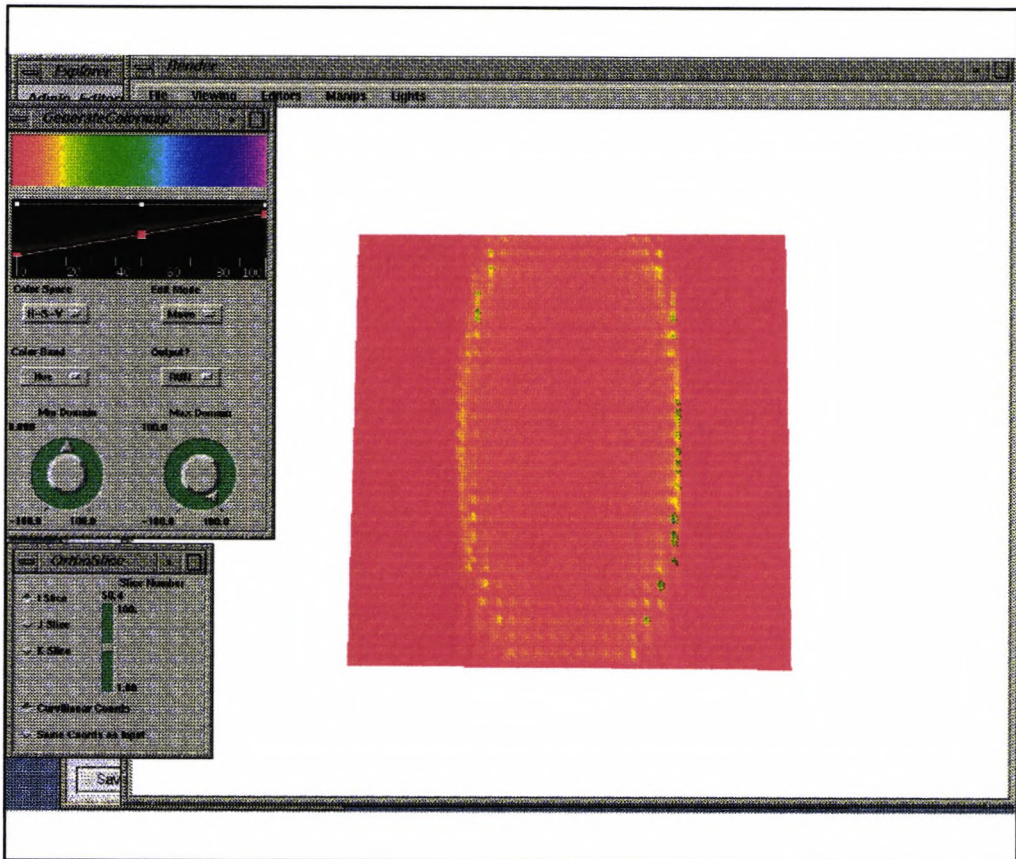
Figure 76 The vertical slice through the sphere

The sectional views of the 3-D scheme's reconstructions showed the ring feature it produced from the shell curving in an equivalent amount in both horizontal and vertical axes, corresponding to the sphere's curvature. However for the 2-D scheme these sections show a asymmetric reconstruction in the sectional views. This occurs in the vertical plane where the slice scheme causes a loss of information necessary to replicate the curvature of the original sphere. The wall of the sphere spreads along the axis of the reconstructing planes.

A slice reconstruction of the solid test sphere was also carried out for purposes of comparison. The slice view orthogonal to the direction of view shows
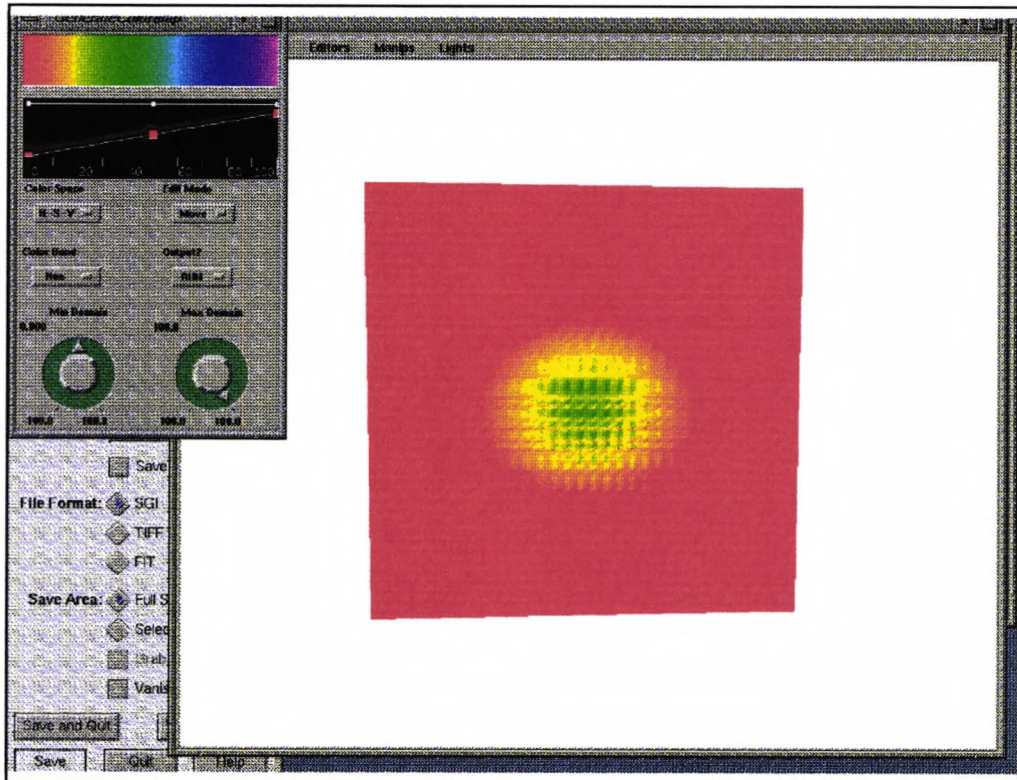
Figure 77 A vertical slice through the solid sphere test object, orthogonal to the viewing axis

the distortion produced by this reconstruction scheme as the spheres circular cross section now becomes oval. Using the 3-D projection scheme to reconstruct this gave a circular cross section, accurate to the original model, thus this oval distortion in the slice result shows the superiority of the 3-D scheme.
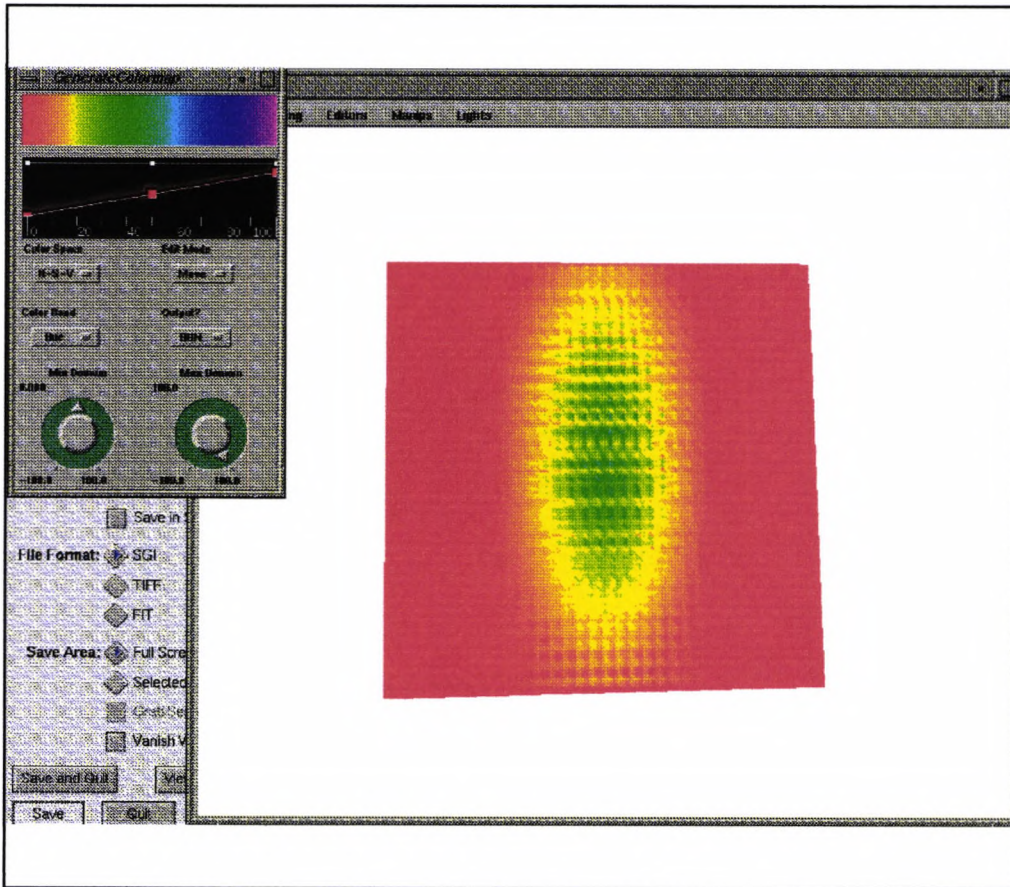
Figure 78 The section perpendicular to the projection scheme slices

Viewing the above section, perpendicular to the plane of the reconstructing slices it can be discerned that the elongation along the viewing axis is similar to that see previously in the 3-D projection scheme but to an even greater extent. When the orthographic slice parallel to the projection scheme slices is viewed the spreading is pronounced giving an "x" shape to the view.

128
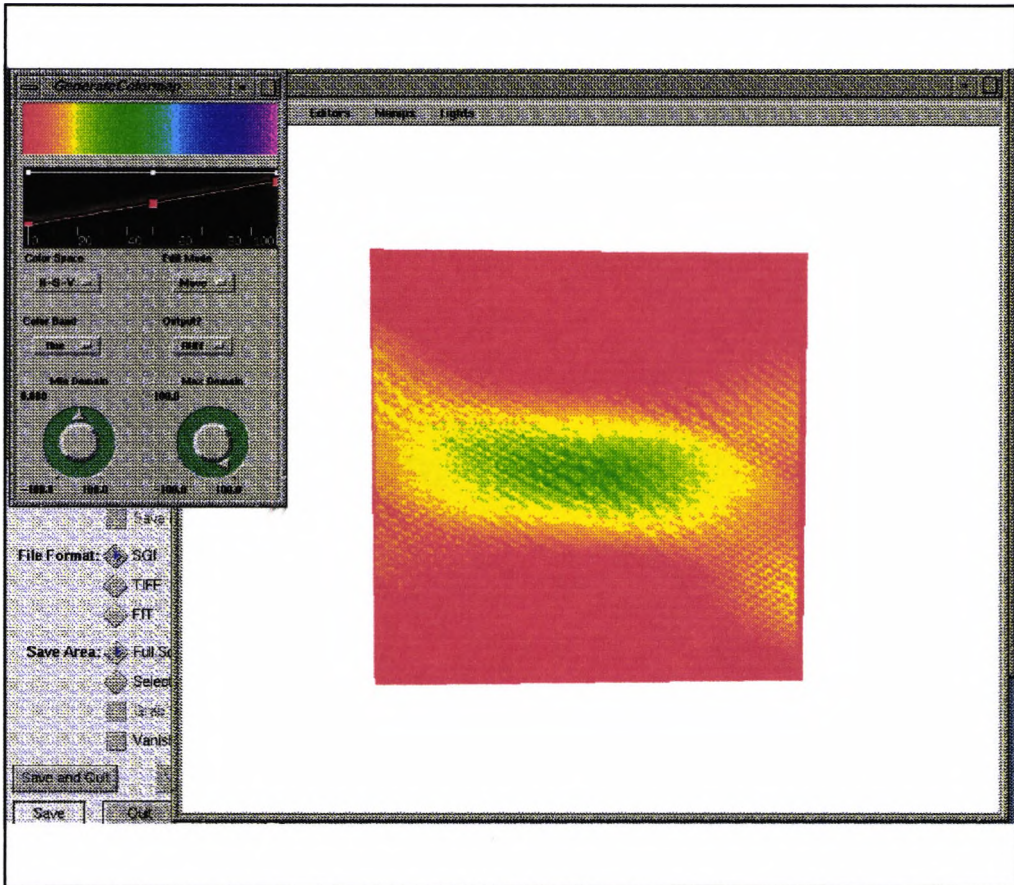
Figure 79 The slice parallel to the project schemes slices

Once again it clear that the slice reconstruction produced substantially poorer representations of the original test objects than the three dimensional projection scheme used previously.

6.0 Construction of a practical tomography system

Having successfully demonstrated the merits of our direct three dimensional projection scheme on computer models we moved to the next phase of our work, namely the application of this method to real holographic data. The next goal was to develop a practical tomographic system from this. The development of this practical system required two main areas of work, the construction of an image acquisition system to extract the data from the holograms and a computing system capable of handling real data.

6.1 Upgrading the tomographic systems computational power

Initially the tomographic reconstruction program had been developed on an IBM compatible PC computer and then transferred to a Silicon Graphics workstation. This was in order to allow the reconstruction of fields with higher resolution as it was necessary to increase both the processing speed and memory available. The computer in use at the start of this project was a PC with 486 processor running at 33 MHz and 8Mb of RAM; this had allowed reconstructions of a 30x30x30 cube of elements. At this resolution a test reconstruction took several hours. To increase resolution from 30x30x30 to 100x100x100, (an increase from 27,000 to 1,000,000 elements), would have resulted in run times measured in days and hence the PC computer had reached its practical limit in terms of run time. It was therefore decided to upgrade to a high performance workstation.

Several different machines were considered but the optimum in terms of price verses performance at the time was a Silicon Graphics R4000 Indigo with a MIPS 4000 RISC processor and 32 Mb of RAM. This had the added advantage of compatibility with the Silicon Graphics workstations used at the Rolls Royce Applied

Science Laboratories, easing the installation of the tomographic software on their computers. Our tomographic software had been developed using Microsoft's C version 6 compiler on the PC using the DOS operating system and thus had to be recompiled to run on the Silicon Graphics Workstation with it's UNIX operating system. In the original programming process care had been taken to use ANSI standard C functions with the ease of running the program on other computer platforms in mind and thus the code was able to be recompiled without modification using the Silicon Graphics C compiler. When a test reconstruction was run using a 30x30x30 field the Silicon Graphics computer was found to be approximately ten times faster than the 486 PC computer. The size of the test fields was then increase and the Silicon Graphics Workstation proved capable of processing cubic fields of 100x100x100 units when using test data and was hence suitable for use with data from the holograms.

6.2 Image acquisition

In order to extract data from the holograms an image acquisition system had to be constructed. The principle components for this were to be a high resolution charge coupled device, (CCD), camera and a frame grabbing board.

The camera selected was a Cohu monochrome CCD camera. As this camera is a relatively low noise device as this would contribute to accuracy in the final reconstruction. This was mounted on the 4 degree of freedom positioning system that enabling the holograms to be photographed about a cone of views as required by our tomography program. The principle of operation of the camera is the storage of electrons on a grid of semi-conducting elements, when exposed to light the electrons are able to migrate to a region in the semi-conductor where they can be detected when the

grid is read. A monochrome output was selected as the holograms contained no chromatic information, (they simply assume the colour of the laser light used to reconstruct them), and a monochrome camera gave greater pixel resolution than a colour camera with the same number of CCD elements. The resolution of this camera was 512x512 individual CCD elements, which were rectangular in shape to give the 4 by 3 aspect ratio of a video picture. The camera's output was a CCIR standard luminance signal.

To convert the video camera's analogue output into a digital form suitable for use in the computer an image acquisition card, (or frame grabber), was required. The frame grabbing card selected was an Overlay Frame Grabber made by Imaging Technology, maximizing compatibility with existing Imaging Technology equipment in use at Rolls Royce. The Overlay Frame Grabber, (O.F.G.), has a frame store which can be configured to acquire a 512x512 picture in monochrome, matching the output from our camera. This card was installed in PC compatible computer where the images were stored before being transferred to the workstation.

Software to drive the frame grabbing card was supplied by the manufactures but specific programs to control the operation of the frame acquisition process had to be written. The drive software was supplied in the form of libraries to be included in a Microsoft C compiler, which once installed allowed programs written in this C compiler to control the frame grabber. In terms of our particular needs the first requirement was for a program to display the camera output on a monitor with registration marks overlayed to enable the alignment of the camera to a point in the field. Once aligned the view would then have to be

digitised and stored on the IBM PC hard disk read for transfer to the workstation. A program was written in Microsoft C to perform these functions and it's operation is shown in the flow chart figure 80. The first process to take place is the initialisation of the card and then the setting of the Global Area of Interest for the framegrabber, (that is the area of the input image that will be processed, in our case all of the 512x512 image). Once the framestore had been cleared and the camera input detected an image would be displayed on the monitor. On this displayed image our program overlayed a cross hair to aid the alignment of images. The program then grabbed the image into the framestore and wrote this data to the hard disk for storage. This program proved adequate to acquire the images from the holograms in operation.
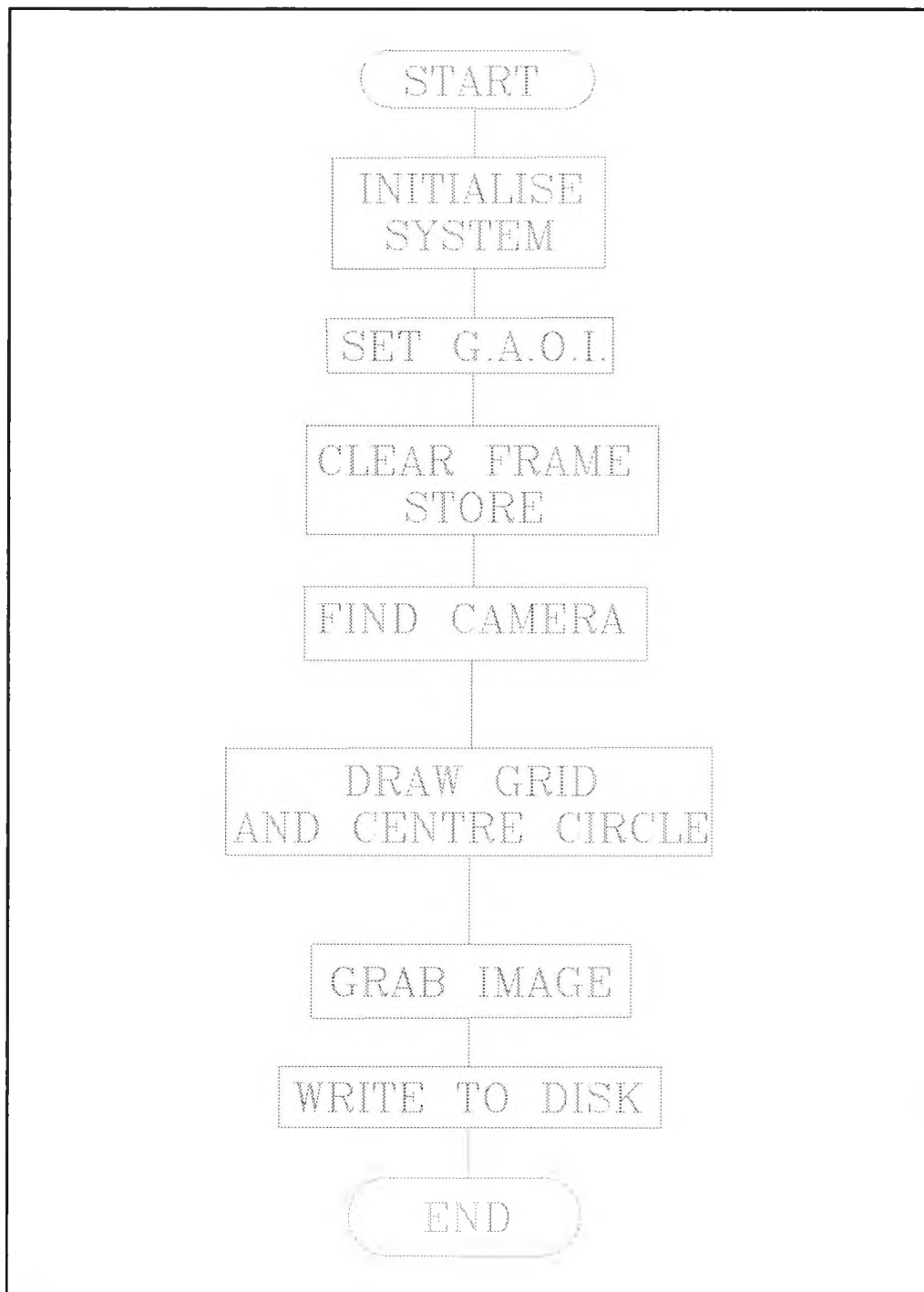
Figure 80 The image acquisition programs flow chart.

To provided an accurate method of moving the camera between views a precision mount was constructed. The required range of movement was determined by the views to be taken from the hologram, and as discussed previously these are in the form of a cone subtending

an angle of less than 45 degrees and typically no more than 15 degrees. Thus a translation system was devised to move the camera in the vertical and horizontal axes and rotate the camera in the x and y planes, thereby allowing a series of views to be taken about a cone. This is shown in figure 81. To minimise the cost of this system it was constructed from proprietary parts. Cost ruled out motor driven movement stages, however as the time penalty involve in manual adjustment of position did not effect the accuracy of the photographic measurements taken this was not an important consideration. The vertical and horizontal translations stages are simple screw thread movement devices from Time and Precision, these have a vernier scale which allows measurements to be made to one tenth of a millimetre. On top of the horizontal translation stage a rotary movement stage was fixed to provide the rotational movement in the horizontal plane. A right angle bracket was attached to this to act as a vertical mounting for the second linear translation stage. A final rotary stage was mounted on the side of the vertical stage to give the vertical plane rotation. Both rotary stages were supplied by Ealing Electro Optics and have a vernier scale to measure rotation which allows reading of 5 minutes accuracy. The complete mount was fixed on an optical table carrying the hologram and the laser used to illuminate it. By adjusting the cameras position with the linear stages and its direction with the two rotations it was possible to take the desired range of photographs. Appendix 13.3 shows the reconstruction optics.
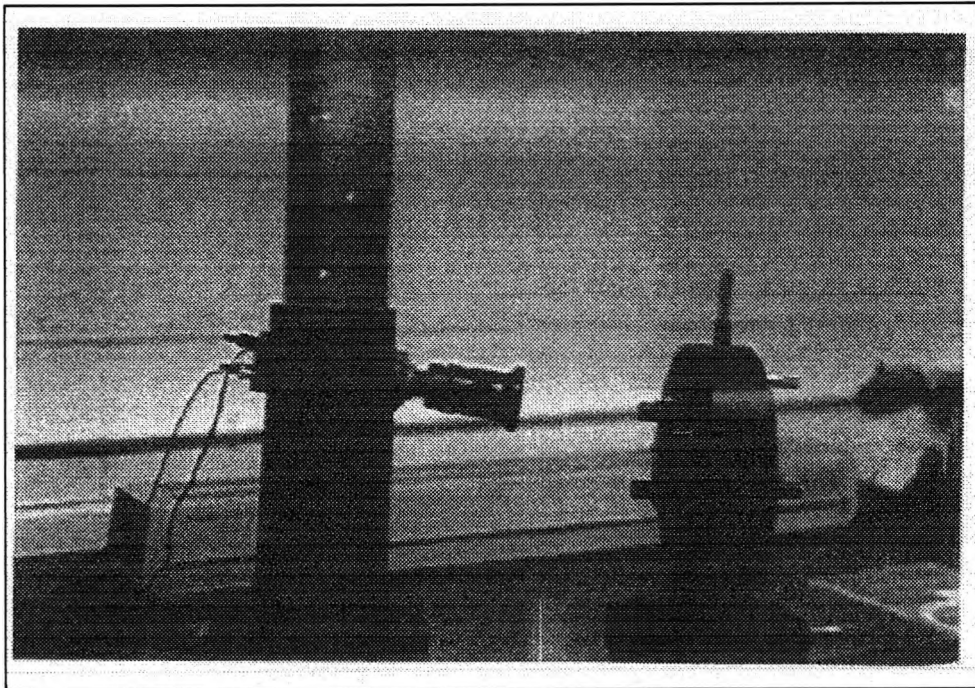
Figure 81 The image capture apparatus

6.2.1 Image data

The camera output the image in serial form to the frame grabber where it was converted to a series of digital levels between 0 and 256. A program written in Microsoft C and run on the PC was used to control the boards operation. Once an image had been converted its data could be written to a file from the C program. This gave a series of integer values representing the intensity at each pixel.

It was possible to perform various filtering functions at this stage using routines supplied with the OFG software. Some preliminary tests were carried out with the image sharpening algorithm, the Roberts filter, and the Sorbel filter. All three of these increase fringe visibility to some extent however a series of comprehensive tests would be required to accurately determine the effect of these processes on

136

final reconstructions. Hence at this stage it was decided to use the sharpening only on the holographic images to minimise the possible variables in the testing process.

After processing had been completed the image could then be transferred to the workstation for reconstruction via an etha net connection between the two computers.

6.3 Handling real data for tomographic processing

The tomographic processing took place in the workstation using a program closely based on that previously developed on the IBM PC. The three dimensional projection scheme is used with exactly the same subroutines to generate the geometric data required for the operation of the reconstruction algorithms as previously. The reconstruction algorithms used in conjunction with this were the ART, Lent MART and Gordon and Herman MART.

To give higher resolution in the final reconstruction the array representing the field was enlarged to 100x100x100 and the ray tracing process was also adjusted accordingly. As may more rays were processed in a single view it was found to be appropriate to reduce the relaxation factors for both MART algorithms. This was the case because more processing of each individual voxel occurred as more rays passed through it for a single iteration. The Lent MART algorithm was operated with a relaxation factor of 0.03 as was the Gordon and Herman algorithm.

As previously mentioned the images were represented by 512x512 data sets. Now a requirement of the program

for accurate ray tracing is that rays being considered from a single view are sufficiently widely space to avoid more than one ray passing through a voxel at the same time, (see Appendix 2). Imposing this restriction had greatly simplified the ray tracing process. However this condition could not be met with a 512x512 element view and a 100x100x100 cubic field as approximately 25 rays would pass through each voxel. Thus a method was devised to allow the rays in a view to be processed in turn so that the ray tracing program did not have to consider rays that were closely spaced at the same time. Each 512x512 view was broken up into a series of more widely spaced 50 x 50 views that could then be used with the existing program. The process can be considered as sampling the view with a 50x50 grid whose points are space 10 units apart in the vertical and horizontal direction. Once a 50x50 set of sampled data has been used the grid is then moved one element along in the view and the sampling process repeated. This was performed until all the individual data points in a view have been considered, thus utilising all the data in a view. A more detailed discussion of this process is give in appendix 2.

6.4 Alignment of views

In order to process the data from each view its position relative to all other views used has to be calculated and these positions entered into the tomography program. Two methods for the alignment of the view were considered, selecting a fixed alignment geometry with an arbitrary position or aligning the views to a point in the field. The method chosen was the latter as it allowed the areas of particular interest to be most easily selected which was important in a practical field, especially important as the actual range of views of

the total field would probably be limited. Its disadvantage is that this method required a manual alignment of the views to a particular point, the process being to align the central point of each view to the same point in the reconstructed field viewed in the hologram. Thus a set of projections from each view's centre should meet at one point. This allowed the views to be considered as if they lay around a cone projected from the hologram. The view's central point was aligned to the desired point in the field visually. By displaying the camera output with a targeting cross wire overlayed using the frame acquisition card's graphic facilities, it was possible to adjust the cameras position until the target was over the desired point achieving an accurate alignment. By measuring the change in each view's angular position in both the vertical and horizontal axes the relative position of each can be fixed and the appropriate values for vertical and horizontal displacement calculated. This process and its mathematics is detailed in Appendix 1. Three values had to be calculated for the tomographic reconstruction program; the view's distance for the reconstructed field in the x-axis, its height in the y-axis and its displacement in the z-axis. These were fixed relative to the top right hand corner of each view.

To check the accuracy of the positioning of each view, a back projection was made from each, then the paths produced compared to one another using a data visualisation program. The back projections were produced using the tomography program modified to operate on a single view simply tracing the rays paths back through the field. If correctly aligned with the appropriate constants entered in the program the back projections should overlap at a single position,

providing a simple and accurate check. This is the
condition shown in figure 82, with two cross back
projections meeting at a single position, (one back
projection is shown wire framed for ease of viewing).
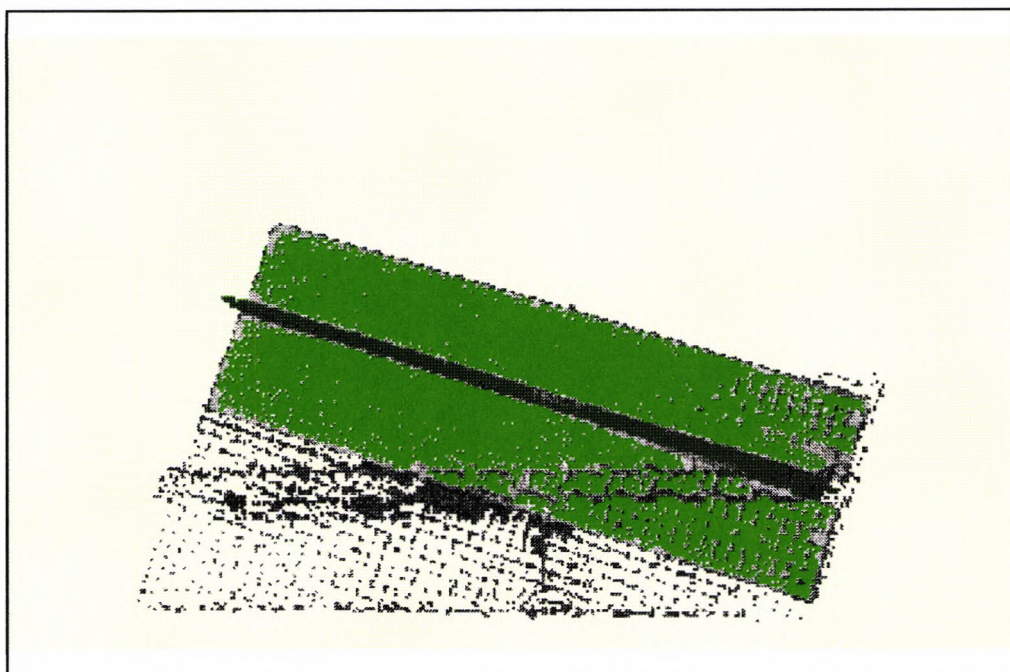
Figure 82 The alignment of two images

6.5 Visualisation of Reconstructions

Visual interpretation is a powerful tool in
assessing the shape of the reconstruction produced by
a tomographic system, however our program produced
numerical data only. Thus once the reconstruction data
had been produced by the tomographic reconstruction
program it had be converted into a form that could be
displayed graphically in order to be interpreted
visually. The complex task of generating high quality

140

representations of the data demanded a specialised software package, fortunately just such a package was provided with the workstation. This was the Silicon Graphics Explorer package which allowed the data to be viewed as either 3-D iso-surfaces, 3-D contour maps, or 2-D sections orthogonal to the x, y, or z axes. To produce these views the data first had to be entered into the Explorer package and this required the creation of a data entry module for use with our data. This data entry module was created in the explorer program and arranged the input data into a three dimensional array of floating point numbers from which the required views could be generated. To produce a view of the data the input module was linked to a processing module and then a display module using a graphical user interface. The functions of the processing module were as follows:

An iso-surface generator which would generate a view consisting of a three dimensional surface joining all the points of an equal value, this value being a variable entered in the processing module by the user. This function was particularly useful for studying the overall shape of a reconstructed object.

The contour generator produced a set of contours spaced between an upper and lower boundary value set by the user. The number of individual contours was also variable and these were automatically coloured for identification purposes. When observing the variation of values in a reconstruction the use of this function was particularly valuable.

A section generator module produced views that were two dimensional sections cut parallel to the x, y, or z axes. Used in conjunction with a false colour generator module, two-dimensional representations of the density variations in a reconstruction, could be produced with the colour of an area indicating its value. This was a very useful technique for

visualising the density variations through the centre of a reconstruction.

All the graphical views of our reconstruction were produced using these modules, either individually or in combination.

6.6 Assessment of Accuracy of the Real Object Reconstructions

The reconstruction of real objects presented new problems when considering the accuracy of the tomographic process. The sources of potential error increased to include the accuracy of the photographic images and the errors in the alignment of each view as well as the error in the tomographic process. Obviously the previously used method of comparing a reconstruction directly with the computer model sampled to produce the reconstruction data was impossible when dealing with real object data, and hence a new method of accuracy assessment had to be devised.

To determine the accuracy of feature reconstruction the reconstructions were compared to geometric computer models of the objects under test. The process was as follows: the reconstructed object was subtracted from a geometric model of the object generated in the computer from physical measurements of the object, if the reconstructed object was correctly present in a voxel the result was a zero, if it was missing or in an incorrect voxel the error was set to one for that voxel and the final error was calculated as the average of these individual errors for the whole field. Thus the error figure for a completely inverted reconstruction of the objects field, i.e. the exact reverse of the desired reconstruction, would be 1. The criterion used to

decide whether the reconstruction was present in a voxel was if the voxels value was greater than twice the mean value of the total reconstructed field. The results produced by this method are discussed in the following section.

7.0 Initial Results Produced By the Practical System

7.1 Test Reconstructions to Calibrate the System

A series of tests was carried out to establish that the fully integrated system was operating correctly and to calibrate it. To test the systems operation a dummy three dimensional figure was produced. A solid three dimensional cross test object was used as its fixed dimensions would allow the reconstructions accuracy could be checked. The cross object was black on a white background to mimic the effect of the holograms having a dark blade and shockwave in a bright field. As the holograms of the blade and shockwave could only be viewed over a 10 degree range the test object was photographed in a series of views with a maximum angles of variation of 5 degrees. Nine views in all were taken , one head on to the cross, two displaced vertically by +5 and -5 degrees respectively, two horizontally by +5 and -5 and the remaining four displaced in both axes at +5 & +5, -5 & -5, +5 & -5, -5 & +5. A reconstruction of this data was performed using the Gordon and Herman algorithm for 5 iterations. The result is shown in figure 83 as a three dimensional iso-surface.
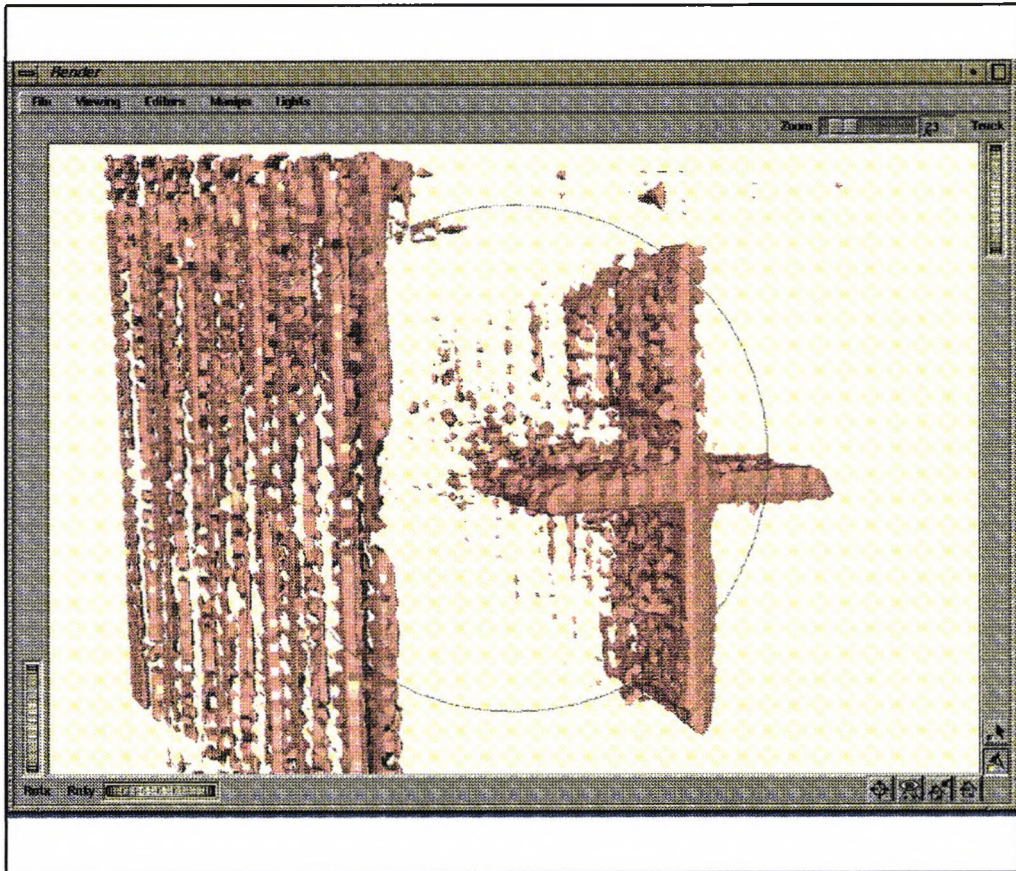
Figure 83 The reconstruction of the physical model

The shape of the reconstructed cross when viewed from the front shows an elongation in the vertical axis relative to the horizontal. This is due to the CCD camera having rectangular pixels rather than square. As our tomographic processing program used cubic voxel elements to represent the field and assumed the pixels in a view were square, when the 512x512 rectangular view was used we considered the pixel as square and in effect compressed the horizontal axis. A simple scaling in the horizontal axis, i.e. considering the voxel sides as rectangular when output for imaging, would overcome any problem caused by this.

Generally the effect of the very limited angle was to cause the cross to lose some spacial localisation

144

and spread along the viewing axis. This was as expected and the shape of the cross could still be clearly discerned in the figure. An effect of the photography is the reconstruction of a dark area in the extreme left of the field, clearly visible in the iso-surfaced cross. This was caused by the photographs including a dark area just off the left-hand side of the test object's brightly lit background. This dark area was reconstructed as a thin vertical plane on the left of the field.

The relative dimensions of the reconstructed cross, (formed from four square faces), were measured by aligning planes with the reconstructions edges. In the visualisation package it is possible to adjust these planes' positions and read off the voxels they pass through directly. The relative dimensions were retained when the effect of pixel scaling was taken into account, i.e. the stretching of the vertical axis in the ratio 4:3. The reconstructed crosses shape was analyzed by comparing it to a computer model corresponding to the physical dimensions of the crosses. Error figures were produced for the accuracy of the reconstructions using this method of comparison. To measure accuracy in the area of interest, i.e. around the cross figure, a boundary field was considered around the reconstruction in which the average error was calculated. This avoided averaging the errors over the rest of the 100x100x100 field which is sparsely populated and thereby reducing the average error unduly by having it average over these voxels. For a ten iteration Gordon & Herman reconstruction the error figure for the immediate field around the cross, (defined as a 60x60x20 box), was 0.0174 . A 10 iteration ART reconstruction was performed for comparison; this gave an error of 0.0322. Clearly the ART algorithm's performance is worse than the MART algorithm in this particular test,

as would be expected from our previous experiments with these algorithms.

From these tests it was concluded that the system was operating correctly, the cross object being reconstructed reasonably accurately, (with due consideration of the very limited angle used for photography). The accuracy comparisons between the ART and MART algorithms' reconstructions when using real data were entirely consistent with those obtained when using computer models in previous investigations and we therefore progressed to real data from holograms.

7.2 Test reconstruction of data from holograms

The second stage of our initial test program aimed
to determine the systems ability to handle data from
holographic interferograms. A holographic
interferogram of a test turbine blade was optically
reconstructed, (figure 84 shows a photograph of the
holographic reconstruction), and photographed using
the image capture system. The views were then entered
into the tomographic reconstruction program and
processed.
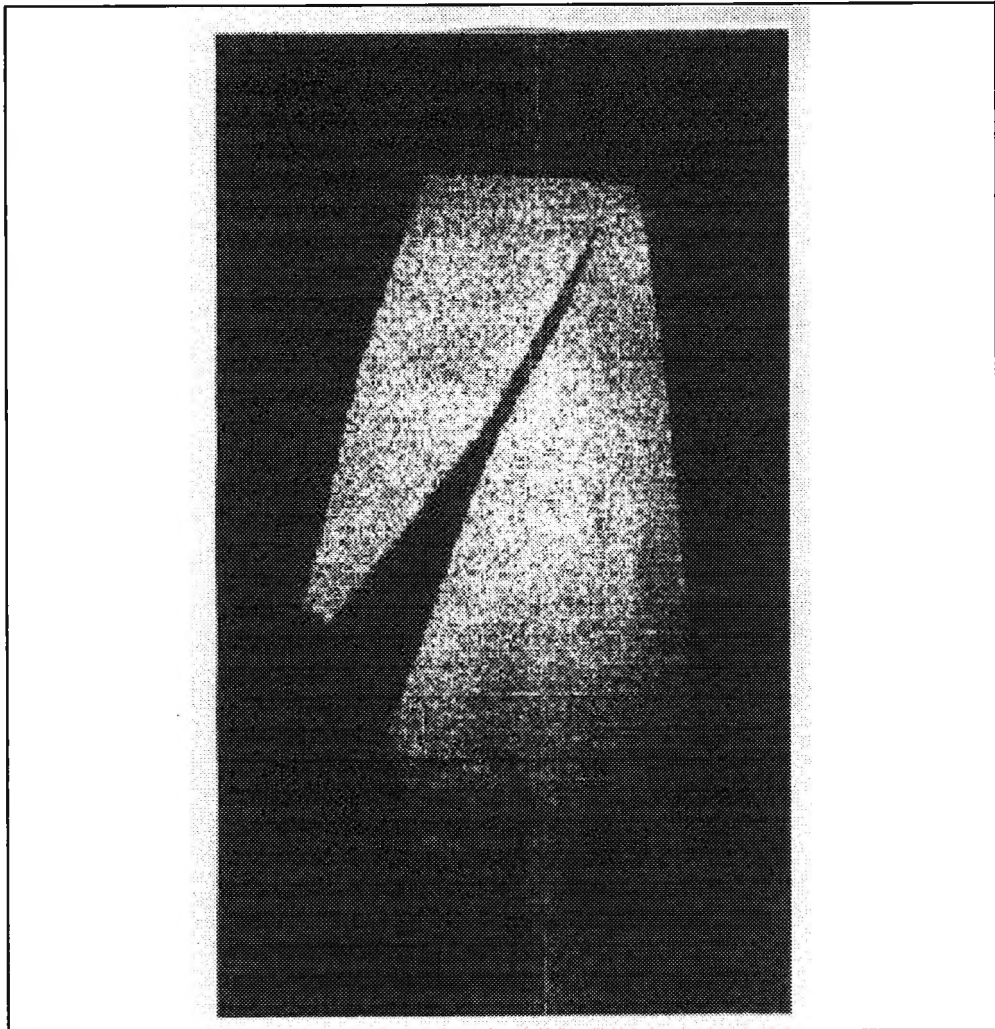
Figure 84 The turbine blade hologram

This test aimed to identify the shape of the turbine blade in the hologram in the reconstruction. The hologram of the blade appeared dark on a bright background and this feature was retained in the reconstruction, figure 85, so that the form of the blade appeared as a dark area surrounded by a high brightness region. The blade appears as a narrow triangular shaped cut out in the iso-surface from its bottom face upward and coming to a point toward the top of the reconstruction. This shape corresponds to that of the dark blade area when viewed in the hologram. The surface which surrounds this corresponds to the bright area in the hologram and resembles the general shape of this area in the hologram. It should be noted that the shape of this iso-surface does change with different threshold values and some care is required to produce a representative rendering of the data.

Figure 85 The reconstructed blade shown iso-surfaced

This test showed that the tomography system could perform reconstructions on views from a hologram photographed about a series of angles of +5 & -5 degrees. The shape of the turbine blade could clearly be visualised in these reconstructions.

7.3 An initial attempt to reconstruct shock wave data

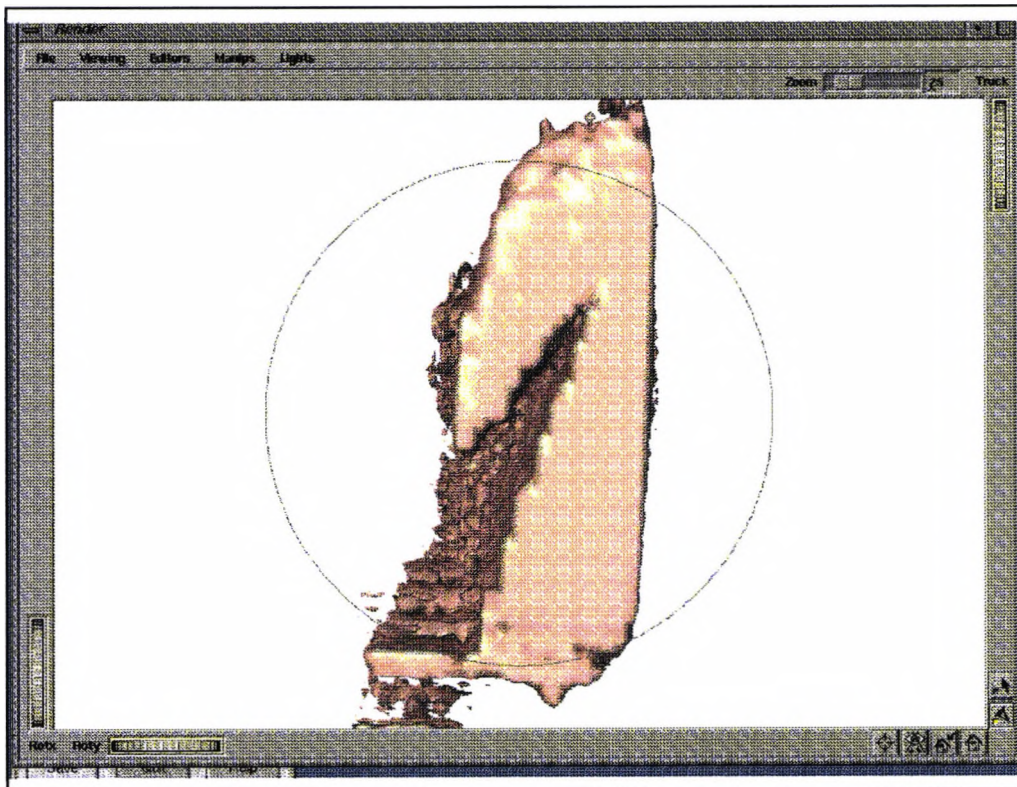Having complete tests on dummy objects and a turbine blade hologram the next stage in our test series was to attempt to reconstruct some shock wave information. The hologram used for the previous test had some shock information with faint fringes near the root of the turbine and as this was already set up for reconstruction it was decided to attempt to use this hologram. Although a shock wave formed near the middle of a blade would have been easier to photograph in terms of restrictions on viewing, being near the edge of the hologram and having worse contrast, this more difficult case would fully test the capabilities of the system.

In order to view the fringes with sufficient resolution for tomographic reconstruction a zoom lens was used to produce close-up images of this area of the hologram. Thus the reconstruction would show only a part of the field, that near the root of the blade. Nine images were taken in the same way as the cross reconstruction test, however the angles at which these could be taken we limited to +3.5 and -4.5 degrees in the vertical axis. This data was pre-processed with a sharpening algorithm and then entered in the reconstruction program and processed for ten iterations. The output was then examined using the orthographic slice module in the explorer software as this enables the greatest detail to be observed in a reconstruction.

149
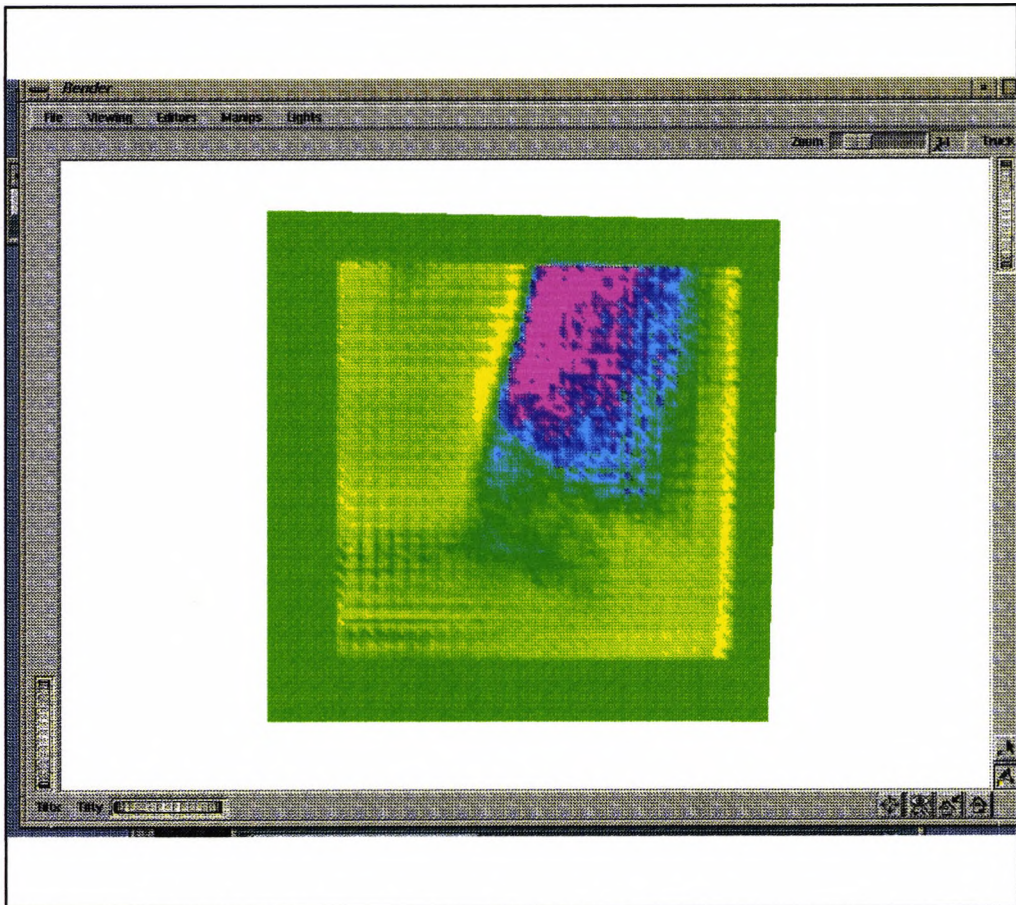
Figure 86 The shockwave reconstruction
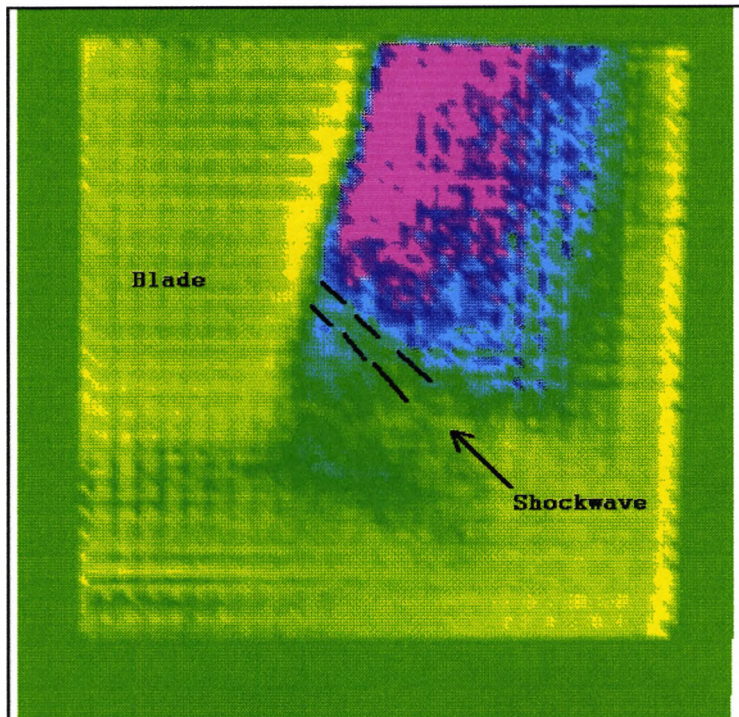
Figure 87 The shockwave highlighted

150

Studying figure 86 the diagonal line upward at approximately 60 degrees which is apparent in the centre of the view corresponds to the face of the turbine blade, the area to the right of this represents the brightly lit flow field and is coloured green and the area to the left is the solid blade. Toward the bottom of this region the shockwave was present in the hologram and thus should also be apparent if the reconstruction was successful. In this region of the reconstruction a faint line may be discerned which roughly corresponds to the shock shape; this is marked in figure 87. As this matches the expected position of the shockwave it appears to be a good candidate for interpretation as a reconstruction of the shock wave. It therefore appeared that the system was capable of resolving shock features.

7.4 Photogrammetry

Using the camera rig it was possible to perform some simple photogrammetric tests to determine the usefulness of this technique. The camera was set up to make point measurements of the cross test model, see figure 88. These were then used to
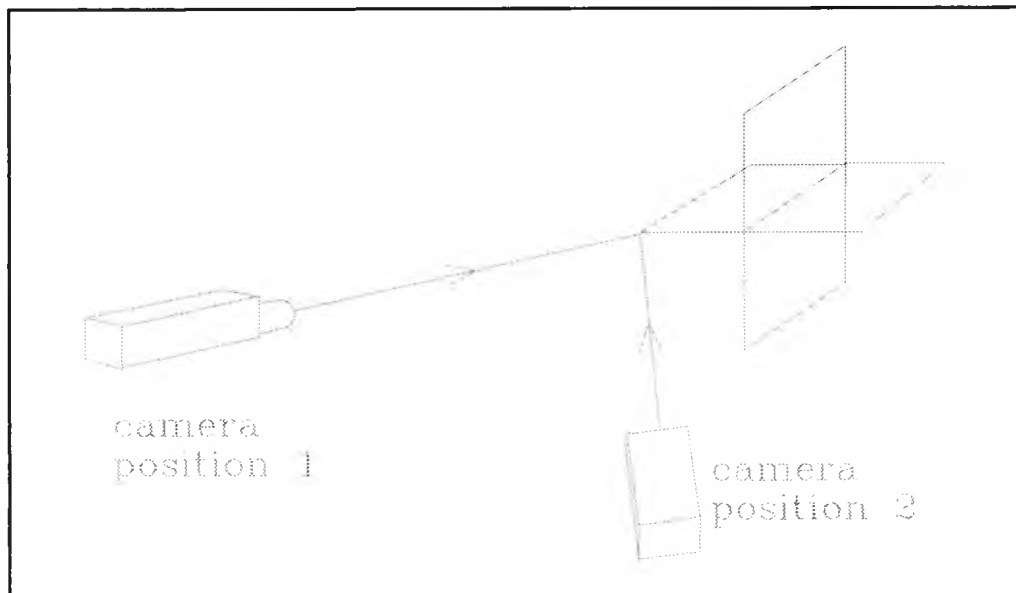
Figure 88 The photogrammetric layout

perform measurements by triangulation. This technique proved adequate to determine the position of the vertices of the cross relatively accurately, (an error of 1% in the crosses dimensions was typical). The drawback of using photogrammetry was that it required points which could be readily identified in each photograph in order to perform the calculations. As it was impossible to identify a series of registration points in the turbine blade holograms available any further work with this technique would require specially produced holograms incorporating registration marks.

7.5 Production of test holographic data

In order to test the effectiveness of the tomographic reconstruction process on the density information present in a holographic interferogram it was necessary to obtain some holograms of variable density fields. The theory of the formation of holographic interferograms for this case is discussed in section 2.2 and following this theory it was decided to produce a double exposure hologram in which the fringes would give density information. The first case that was attempted to study was the free convection flow about a soldering iron's tip.

The method of producing these holograms was by double exposing a holographic plate with light from a pulsed ruby laser. The optical arrangement is shown in figure 89. The pulsed output was required to capture an instant in a changing field during both exposures.
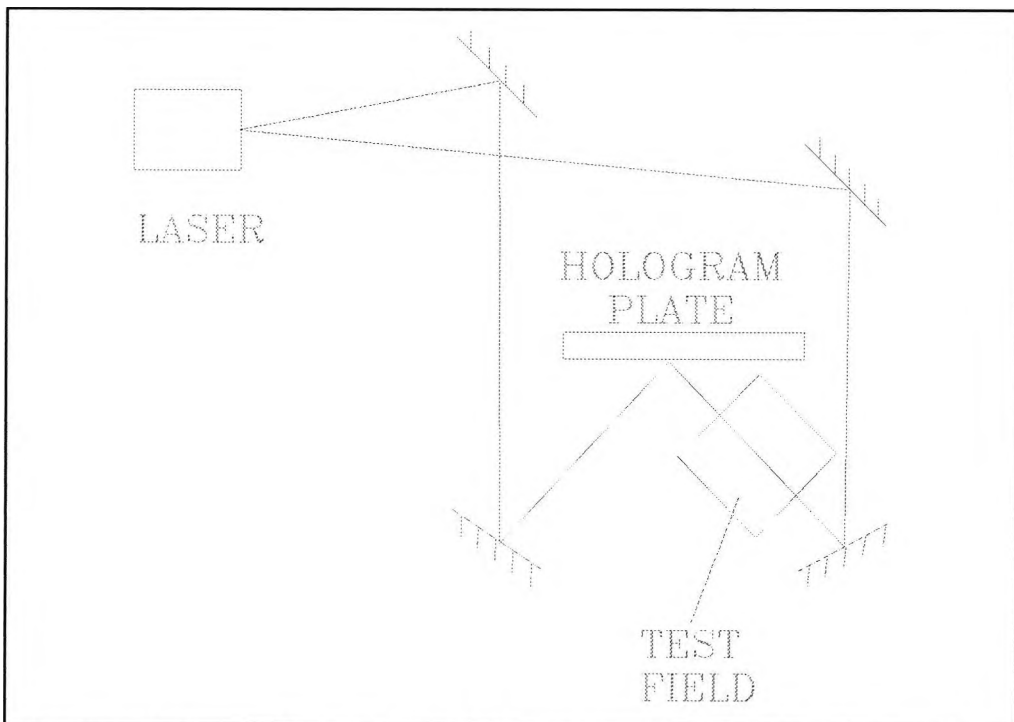
Figure 89 The optical layout required to produce holograms

The object used to produce the flow field was a hot soldering iron tip mounted horizontally, the air heated by it producing a convection plume. As shown in this figure the laser output was split into a reference and object beam with a two hole aperture, having previously been diverged. These beams were steered by mirrors so that the object beam passed through the convection field before reaching the holographic plate.
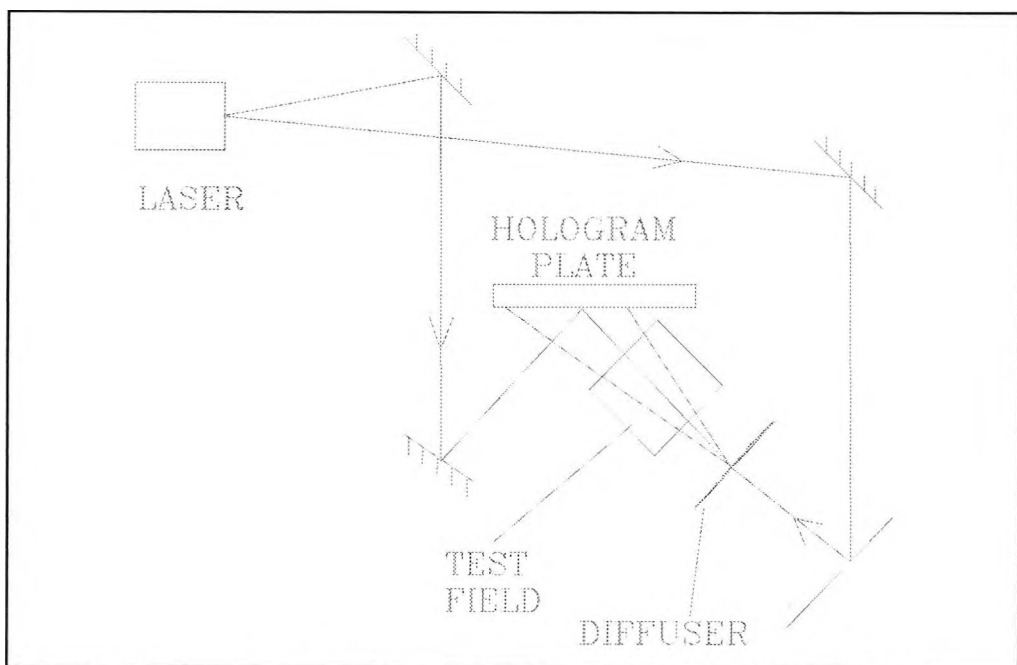
Figure 90 The revised optical path with diffuser

Initial test holograms produced using this optical set up gave a hologram of the object with some fringes in the field about it. These fringes had poor visibility, but did prove the feasibility of this study. Thus it was decided to continue with this set up with one important modification, the installation of a diffusing screen in the object beam path immediately preceding the convection field. This modified set up is shown in figure 90. The tests carried out with this new set up did show the general

suitability of it, however a problem was encountered with the some of the early holograms produced having anomalous field fringes. These appeared as a regular set of vertical fringes across the plate. The cause was traced to the operation of the laser at high power output, (greater than 1.2 joules), causing the output frequency to change, (mode hopping), between pulses. This effect was ameliorated by reducing the laser pulse power output to less than a joule. A series of holograms showing the convection flow around the tip of a soldering iron was then produced, an image taken from one of these holograms is shown in figure 91, (note it has been false coloured by the viewing package used to visualise the captured video images). The optical arrangement of the hologram and fringe position relative to the soldering iron are shown in appendix 13.4 and appendix 13.5.

Figure 91 The fringe pattern captured on the hologram

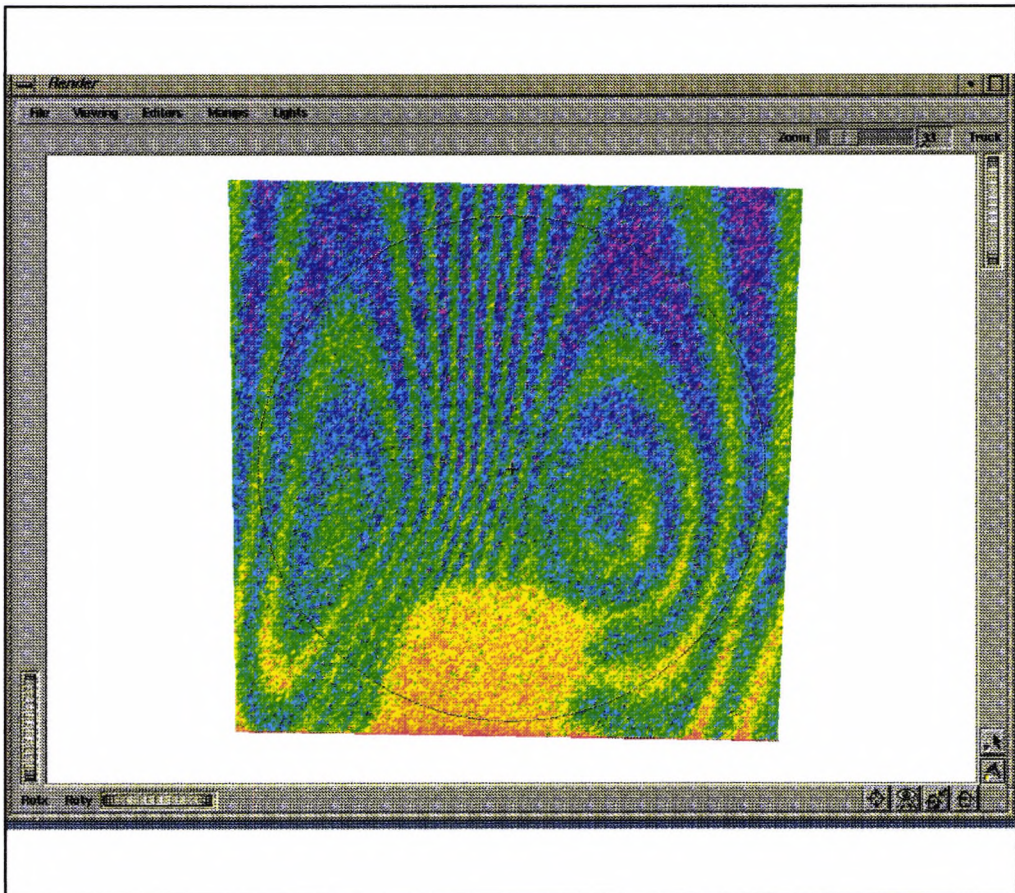The photographs of the holograms were taken from a series of positions each with a different viewing angle. The limit of the possible viewing angles was found to be ⁺₋15 degrees in the horizontal axis and ⁺₋10 degrees in the vertical plane. This effect is due to the diffuser and optical arrangement producing an object beam which diverges as it passes through the field about the test object, its elliptical nature being produced by the beam steering mirrors being tilted in the horizontal plane giving a greater divergence in this axis. These allowed views were particularly suitable for the 3-D tomographic reconstruct program as they contained information which was best extracted by photographing in two perpendicular axes.

After the successful production of the holograms showing free convection about the soldering irons' tip an attempt was made to study the flow about a disk rotating at high speed using holographic interferometry. A plane metal disk, which could be driven to very high speeds, was available and it was hoped that the compressibility effects as this was rotated at speeds, where its edge was approaching the supersonic region, would be sufficient to give noticeable refractive index changes. The experimental apparatus is illustrated in figure 92. Using this set up a series of initial tests was conducted, however these proved unsuccessful. The problem which was encountered was the vibration of the optical assembly caused by the windage from the disk at high speeds. Holograms could be formed at lower speeds, (3000 rpm corresponding to a tip speed of 90 m/s), but this was too slow to produce any compression effects. As the facilities were not available to modify the optics to isolate them from the vibration this line of investigation was abandoned.
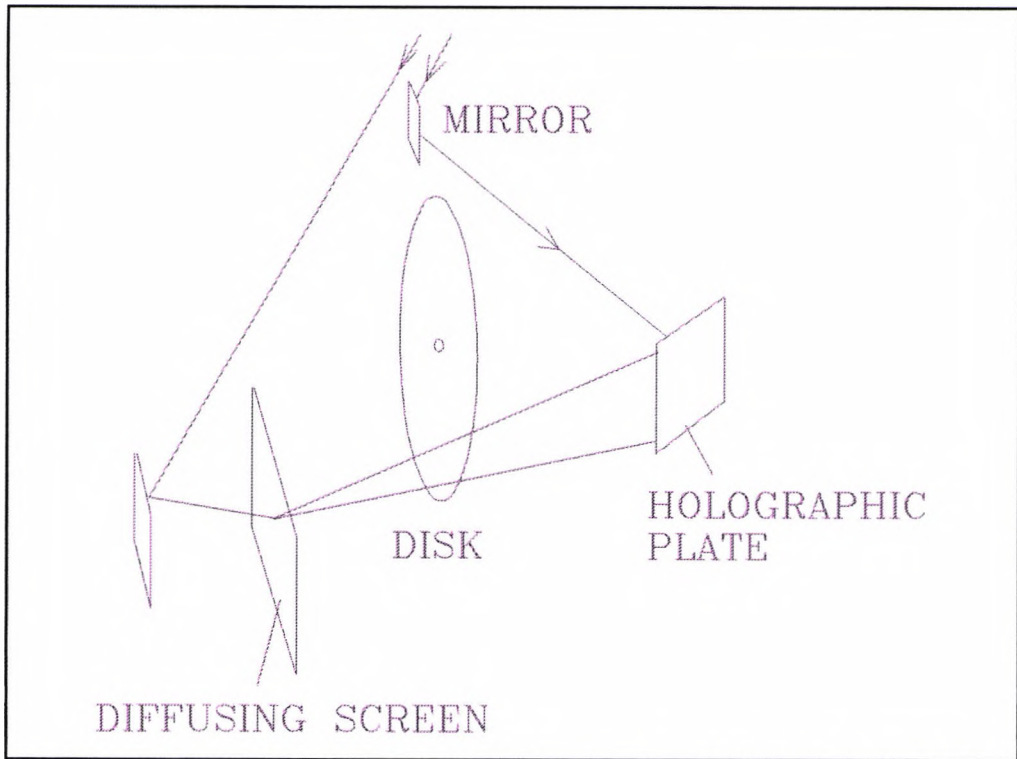
Figure 92   The rotating disk object and optical path.

8.0 Interpretation of the holograms

Having produced holographic interferograms with fringe data showing density variations the next requirement before these could be incorporated into the tomographic reconstruction program was that these were converted in density maps, that is two-dimensional representations of the span wise averaged density across the field in their direction of view.

The simplest method of analysing fringe data is fringe tracing, which can be performed manually. The fringes are simply identified and counted, staring with the reference fringe, to obtain the fringe order. The errors produced in fringe tracing must be weighed against this ease of application as fringe tracing is considered to be the least accurate method of fringe analysis. A previous paper by Hunter and Collins, ref. [5], discussed this and concluded that the maximum accuracy that could be obtained was $\pm 10\%$, compared to actual Mach number in a transonic flow. Hence this could be a major source of error which is independent of the tomography process.

As a starting point for the interpretation of the holographic interferograms an automatic fringe tracing program was chosen. The advantage of this technique was its relative simplicity of implementation and greater speed when compared to manual methods. Initially a fringe skeletonising routine was implemented to generated a map of each fringes path. The principle of operation of the skeletonising algorithm is to reduce a feature's width evenly until only the centre line remains. This approach was found to be unsuccessful when applied to our data as it introduced false branches on

the fringes instead of thinning directly to the centre of the fringe. A second attempt was made to implement fringe tracking using a method suggested by Hunter, ref. [14]. Rather than determine the centre of each fringe the edges of the fringes were detected at the 50% level of average field brightness. These were then used to determine the $\pi/4$ phase change contours. The details of this process are as follows.

As the photographic images of the holograms contained speckle noise, figure 93, a averaging filter was passed over each image. A 3x3 filter kernel which produced the central value from the average of all 9 surrounding pixel was used.
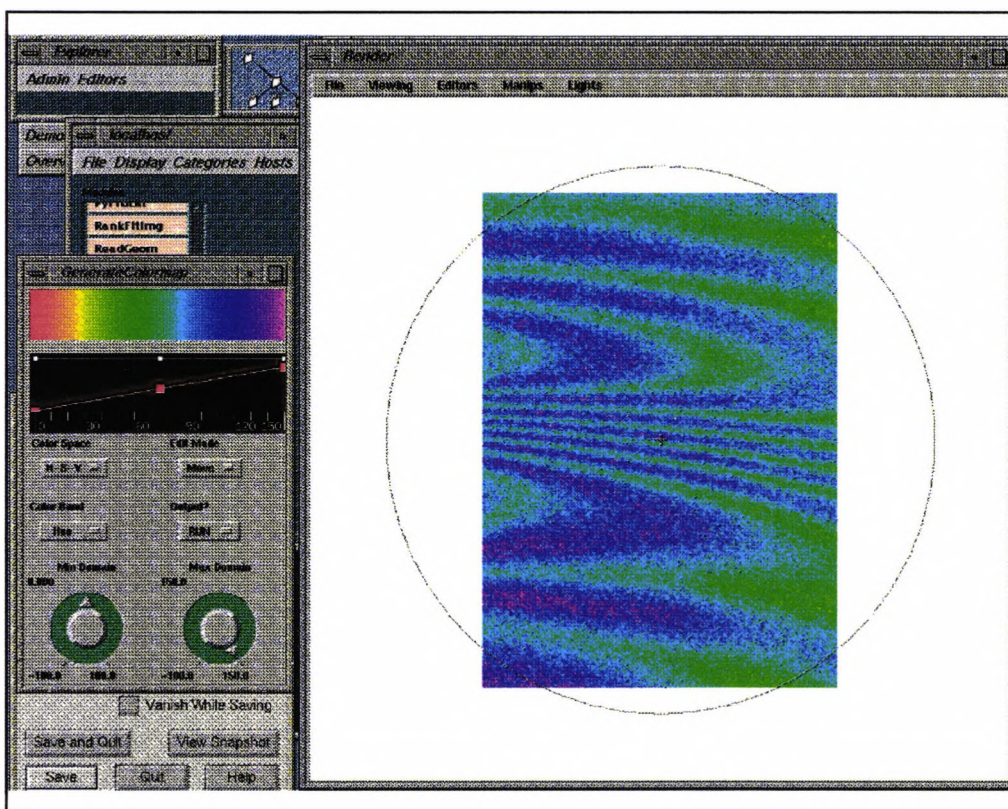
Figure 93   An image from the hologram, shown false coloured on the Explorer visualisation tool.

The filter kernel was
```
1    1    1
1   S/9   1
1    1    1
```
where S is the sum of the nine surrounding pixel values.

This smoothing reduced the speckle in the image. At first the smoothing kernel was passed over the image from top to bottom and then left to right. However when it came to tracing the fringes
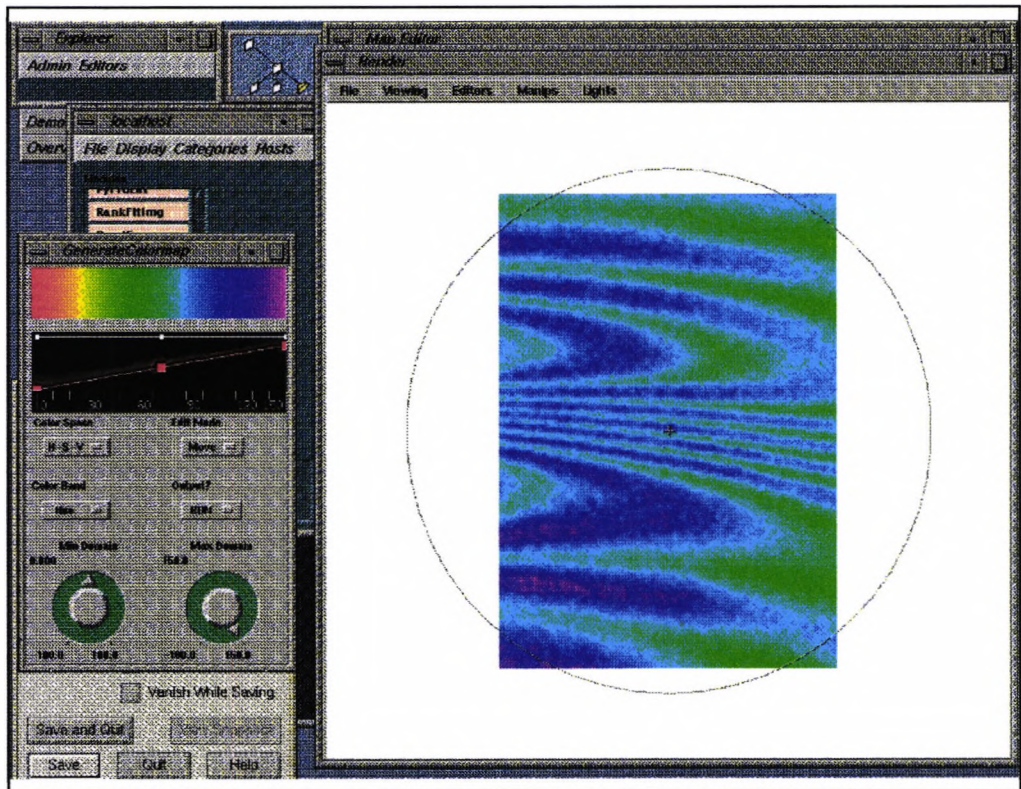
Figure 94   An image after smoothing

it was found that the left to right pass of the filter, which was largely perpendicular to the direction of the fringes, caused closely spaced fringes to smear into one another. As distinguishing between each fringe gives the order of each and thus the density change this was unacceptable. To achieve the required speckle reduction but retain fringe resolution, using only the vertical pass of the filter kernal was tried. This caused a smearing along the length of the fringes but did not significantly reduce

the resolution between them. The effect of this smoothing process on an image is shown in figure 94.

Once the speckle had been removed fringe tracking could be applied. The fringes were tracked by determining the average brightness level in a region of the image and connecting the points which had this value. This average value had to be changed from region to region over the whole image as the background illumination was not constant over the image area. To trace the path of a fringe a program was written on the workstation. It began by searching the image for a start pixel of the correct value in the bottom corner of the image. When a start pixel had been located it was assigned a marking value and its neighbouring pixel were examined to see if any of them were also at the appropriate level. If so they were assigned the same value as the start pixel and the process was repeated, building up a connected line of pixel with the marker value. When no neighbours could be found of the appropriate level the program would restart the search of the image, ignoring those pixel already marked. When a new start pixel was found the program incremented the marker value so this new fringe path would be marked with a different number. This process was repeated until all the fringes had be traced and marked with an individual value, thus enabling the different fringe order of each to be determined.
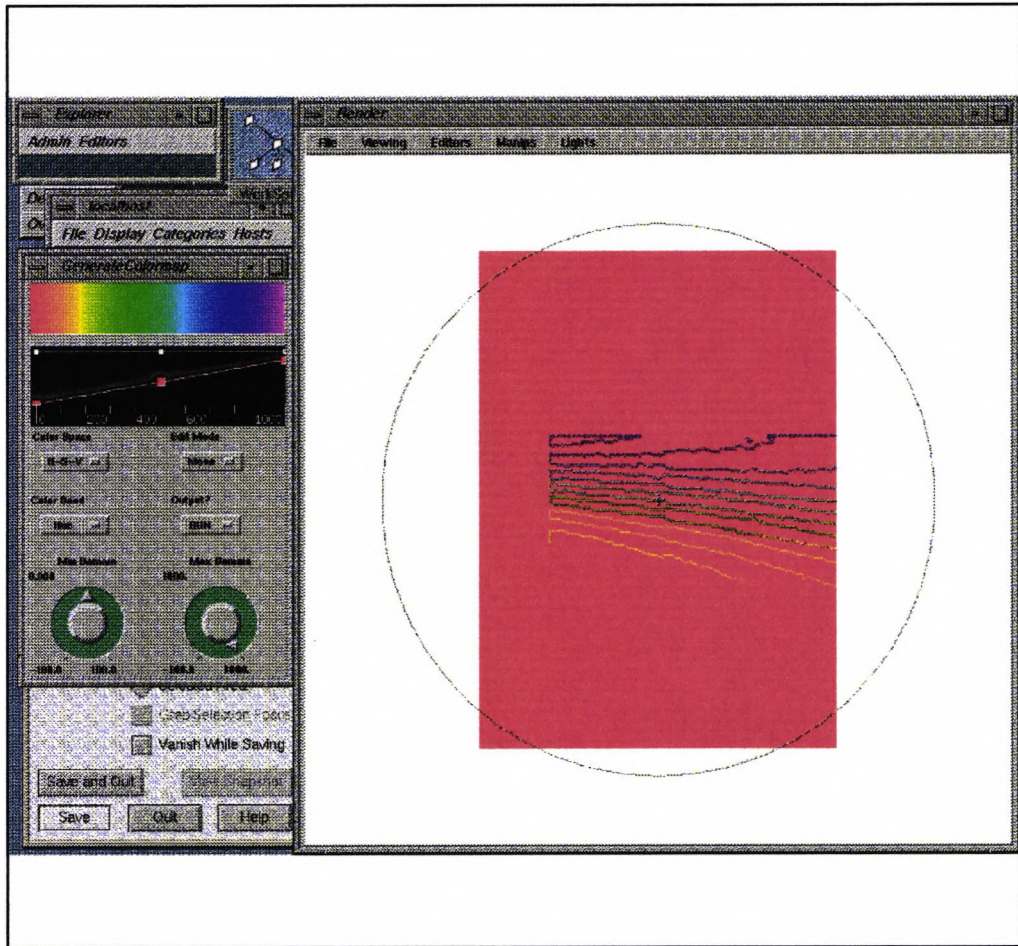
Figure 95 The traced fringe map, each line colour denoting a different marker value

Once the fringes had been marked they had to be converted to density maps. The information from the holographic interferogram is the spanwise averaged phase change across the field. The optical phase change for each ray is given by

$$\phi_i = \int_{S_i} f(x,y,z) dS_i$$

where $f(x,y,z)=n(x,y,z)-n_o$, is the changed refractive index field relative to the reference field, n_o. The

density of the medium, ϱ, is related to refractive index by the Gladstone-Dale relationship. That is: $\varrho G = n-1$, where G is the Gladstone-Dale constant. In the fringe traced images the phase change between two trace lines is π radians. Hence applying this formula to each view in turn allowed density maps to be produced from them.

In practice a step value change was applied at each fringe boundary on the traced fringe maps. The central fringe was located, by simply counting the number of fringes from the edge, and this was assigned the lowest value. This was because the convection column has its lowest density above the soldering iron tip, where the air is hottest. At each fringe boundary outward from the central one the density value assigned was increased by 10 units. These could be used in the tomography program and a final calculation made to convert the resultant field values to absolute density. The results of a conversion are shown in figure 96 with the density map colourised.
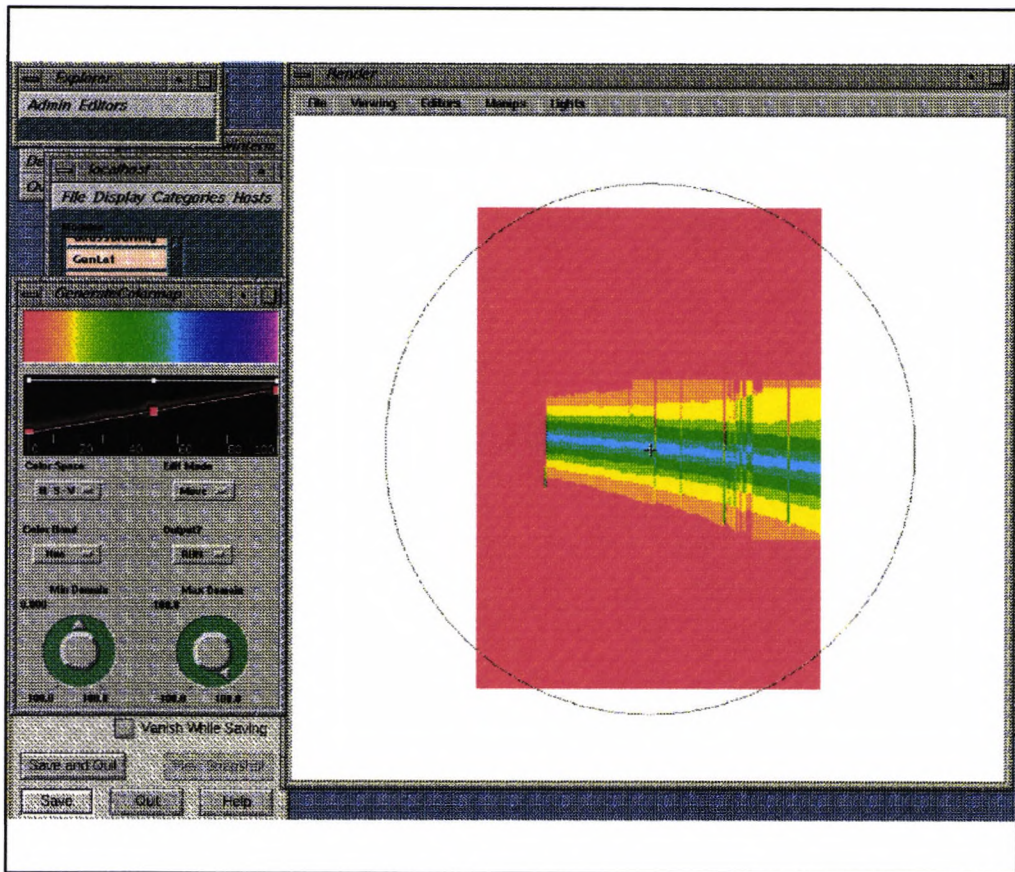
Figure 96 The resultant density map

This technique worked successfully and was used to produce the density maps from images of the holograms for use with the tomographic reconstruction system.

9.0 Results of tomographic reconstruction tests on convection holograms

Having produced holographic interferograms containing density information and successfully converted these into density maps the tomographic reconstruction system could now be tested using this data. Nine views of the hologram were taken over a range of angles, (0,0), (0,+5), (+5,+5), (+5,0), (0, -5), (-5,-5), (-5,0),(+5,-5) and (-5,+5). These views were converted into density maps using the methods described in the preceding section. The resulting maps were entered in the tomography program and reconstructed using the Gordon and Herman MART algorithm. The resultant reconstruction is illustrated in figures 97 to 100.
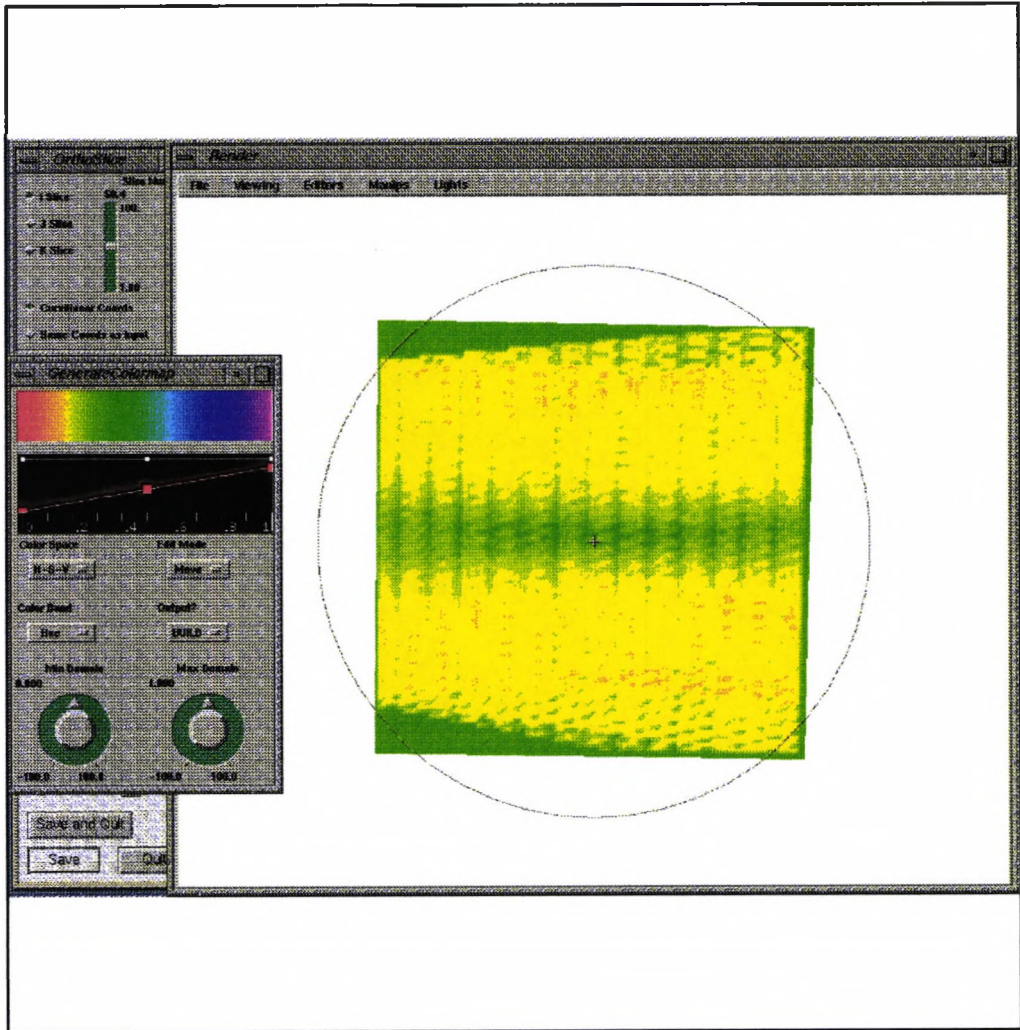
Figure 97 A horizontal slice through the field at a height of 50 units.

Figure 98 A vertical slice through the field at a depth of 50 units

Figure 99 The vertical section at a depth of 25 units
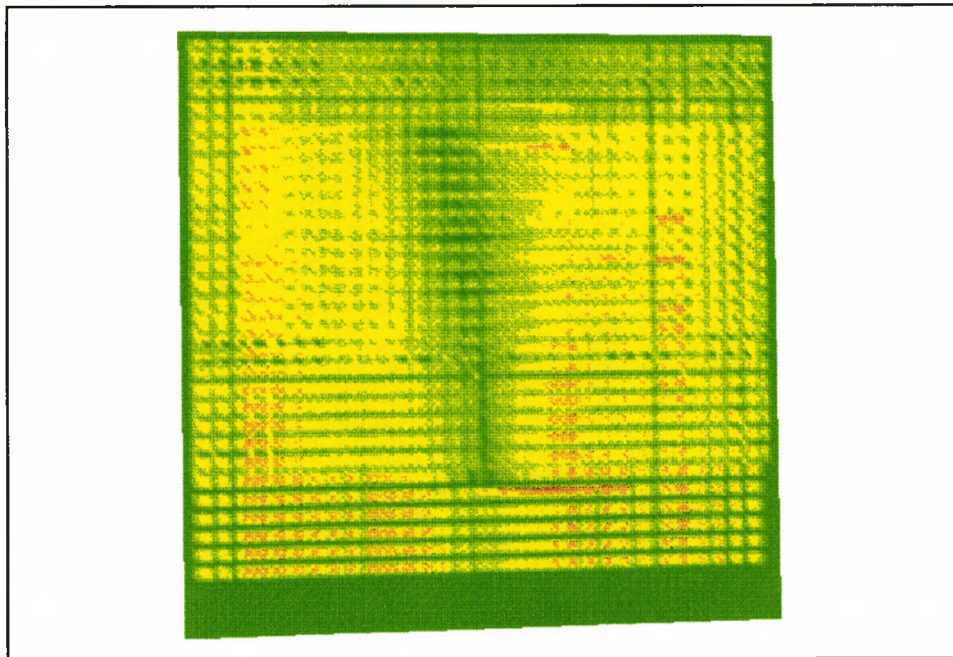
Figure 100 The vertical section at a depth of 75 units

This series of images was created from the reconstructed field in the Explorer visualisation package. The first image is a horizontal slice across the middle of the convection plume. In this image there was a small degree of aliasing, (false patterning due to the discretisation of the field into elements), however the main chequered patterning visible is due to artifacts introduced wh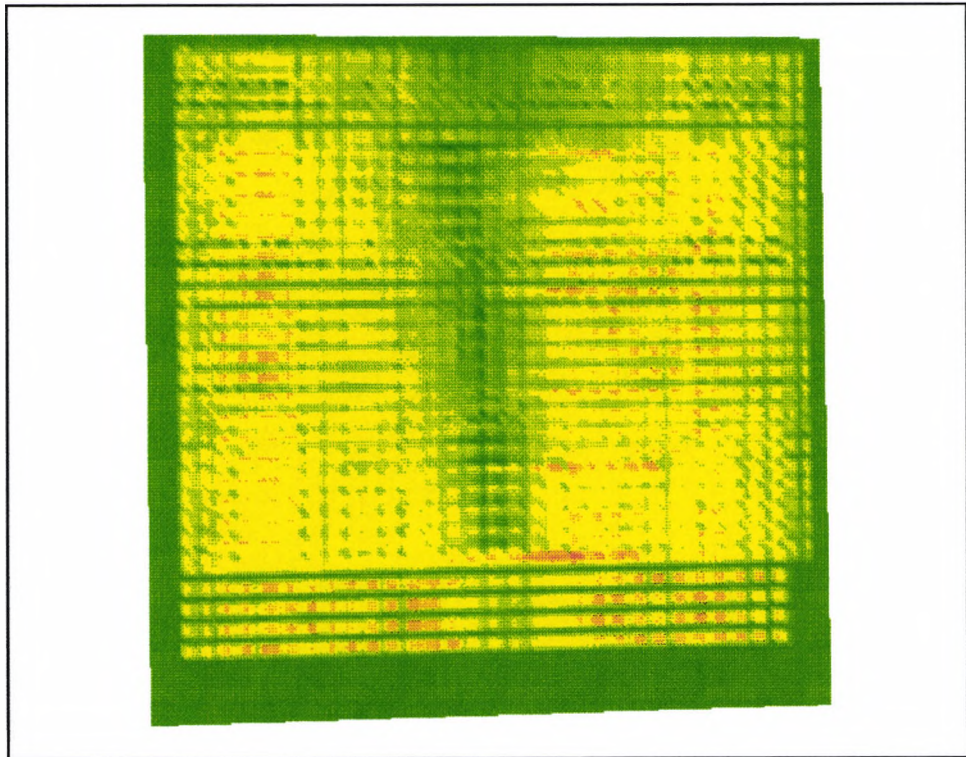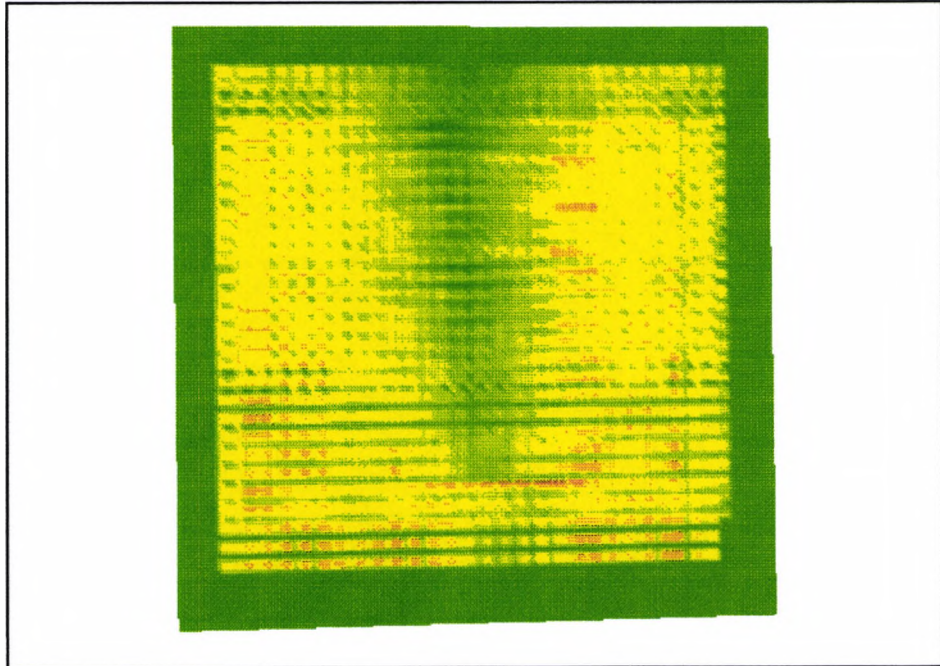en converting the images from TIFF to WPG formats. The green band in this image extends across the length the field because it corresponds to a plan view of the flow from the horizontal soldering iron, as would be expected. The other three diagrams are sections in the vertical plane, orthogonal to the shaft of the soldering iron. The show how the plumes width varies as it moves upward.

Now the expected flow pattern from a heated rod in still air would be a vertical convection column along the length of the rod. Clearly these generally conform to the expected flow pattern from the tip. The colour scale ran from 0.0 to 1.0 with 0 corresponding to red and 1.0 to violet, thus the background yellow area had a value of 0.2 units and the column a value of 0.4 units, giving a variation from the centre of the column to the sides of 0.2 of a unit. These values do not correspond to the absolute densities present but instead reflect input values which were not calibrated. While it would have been possible to calculate absolute values for views using the Galdstone-Dale relationship after reconstruction a further calibration would be required as we have seen in our previous experiments that the numerical values produced during reconstruction do not directly correspond to densities in the original test field. The values assigned in the input density maps were steps of 10 units at each fringe boundary, with these

169

increasing toward the central fringe. Hence increasing number values corresponded to decreasing density. The shape of the convection column is illustrated by an iso-surface generated from the reconstructed field shown in figure 101. This shape tapers towards the columns top as it disperses.
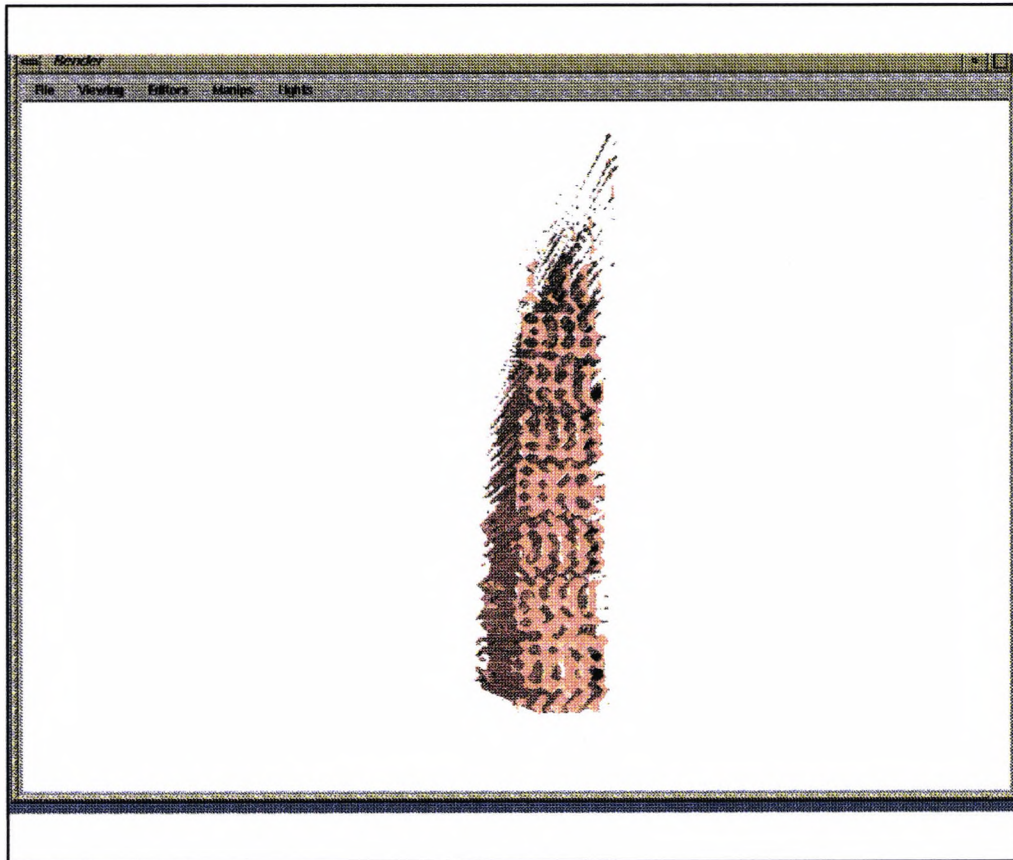
Figure 101 The iso-surface generated from the convection column reconstruction

A further sectional view was prepared with a reduced scale between upper and lower density values to show more detail, figure 102. This section was taken at the front of the field, corresponding to the start of the soldering iron. Once again the shape of

the convection column was plain.
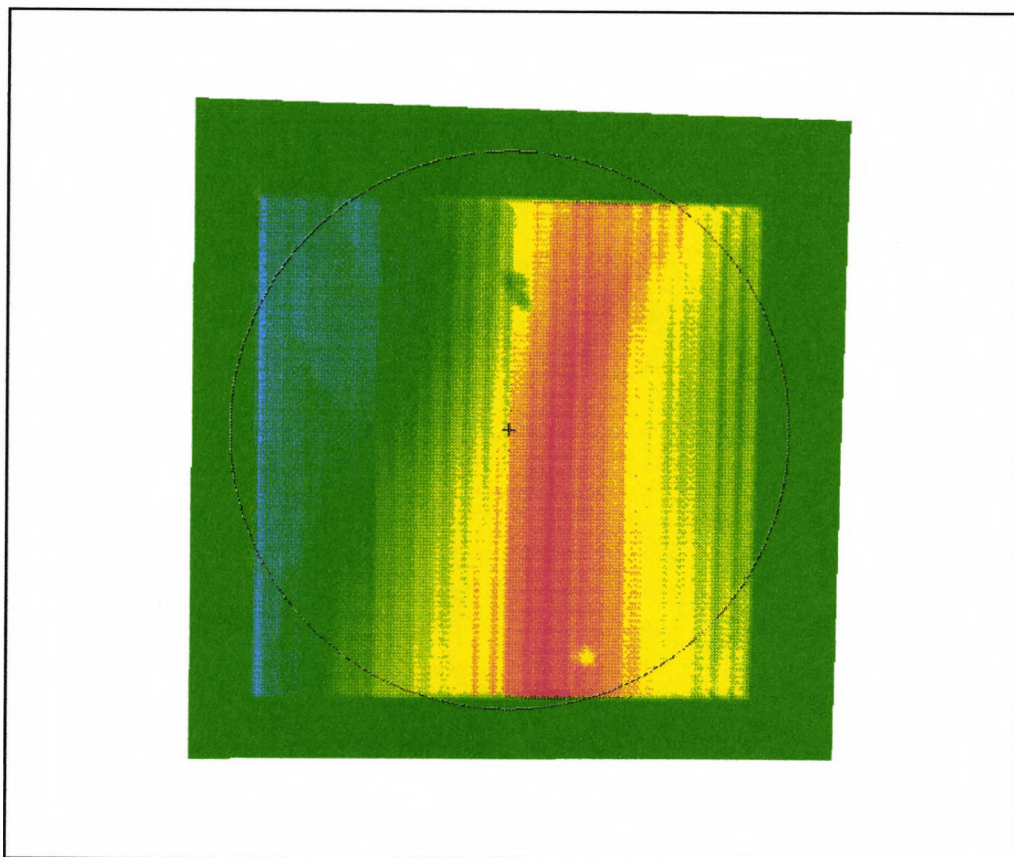
Figure 102 The section at 50 units recoloured with the minimum value set to red and maximum to blue

10.0 Discussion

This work investigated tomographic techniques suitable for the reconstruction of three dimensional fields that are recorded by data captured over a limited range of views. As tomographic reconstruction usually relys on collecting data over a wide range of view the imposition of the limited view angle criterion was the significant factor in our work. Holographic interferograms of the type produced by Rolls Royce Plc in their compressor studies had a very limited range of acceptable viewing angles and these were selected as an initial case study to provide a stimulus to our research. When these were reconstructed using a novel combination of a three dimensional projection scheme and MART iterative reconstruction algorithm a possible solution was identified that gave very promising results, as could be seen in the iso-surface image of the turbine blade and shockwave.

The use of a three dimensional projection scheme for tomographic reconstruction had been proposed previously for cases where limited viewing angle was a problem. By utilizing data from viewpoints which did not lie in a single plane but varied in two perpendicular directions extra information could be introduced into the reconstruction process. It was thought this new information would significantly improve the resultant reconstruction quality by virtue of its' independent nature and our comparative test results would appear to bear this out.

In previous studies the iterative reconstruction methods had been identified as particularly suitable for limited view reconstruction problems, with several different algorithm types suggested. A recent review identified the Gordon and Herman MART algorithm as

possibly the best for this type of problem so we conducted a series of tests against the ART and Lent's MART algorithms that appeared to confirmed this. However it was noted that the ART algorithm did prove to have very stable convergence characteristics and when used over a larger number of iterations than the Gordon and Herman MART the difference in reconstuction quality was reduced.

The tests on model data made one point clear; the three dimensional projection scheme was superior to slice reconstruction for limited angle of view problems and this was a more significant factor than the type of reconstruction algorithm used.

As the Gordon and Herman MART algorithm did appear to give the best overall performance it seemed logical to use it and the three dimensional projection scheme together to see how they would work when combined. When used with our projection scheme the Gordon and Herman MART algorithm did indeed give the best reconstructions. This was verified by the numerical results of error coefficient studies and the visual examination reconstructed test objects.

The model objects examined comprised a pair of thin planes crossed, a hollow sphere and a solid sphere. All three of these were reconstructed using both the 2-D slice reconstruction method and our 3-D projection scheme, with the same iterative algorithms and allowed range of views. The crossed planes reconstructions showed that while the 3-D scheme produced recognisable reconstructions of the original models the 2-D reconstructions were noticeably more distorted. It was the plane which lay parallel to the reconstruction schemes slices which suffered the more extreme distortion, giving an overall asymmetry to the reconstruction. The hollow sphere also showed this

asymmetric distortion when reconstructed using the slice method, with the top and bottom portions of the shell being lost. The 3-D scheme in contrast produced a more uniform reconstruction. Both projection methods failed to reproduce the front and rear of the sphere, these positions corresponding to the areas of the shell that are almost perpendicular to the sampling raypaths, and thus having small pathlength weighting products. The solid sphere had a density which increased towards it's centre and this was the object that the slice reconstruction technique performed best on. The solid sphere seemed to discretise well into a series of circular slices stacked one on top of the other, to give a reasonable reconstruction. However a noticeable asymmetry was produced with the sphere spreading horizontally, parallel to the discretisation planes. In contrast the 3-D reconstruction scheme gave a relatively symmetrical result, once again truer to the original. A comparison of numerical error between the original fields and the reconstructions confirmed the superiority of our scheme against a slice approach.

Having demonstrated the superiority of the three dimensional reconstruction approach a full system was developed around the new software and used to reconstruct real data. A CCD camera was successfully used with a PC frame grabber card to digitally acquire images. Using a set of views taken of a holographic interferograms with displacement in both the vertical and horizontal axes, reconstructions were made. The first holographic interferogram examined was a view of the shockwave generated by a turbine blade, produced by Rolls Royce. While this was not a particularly suitable holograms to use as it contained no density variation information, it did test the systems overall ability to cope with real data. When

174

views from this hologram were reconstructed the blades' shape was clearly visible, demonstrating the systems ability to handle solid objects in a hologram. The shockwave was very faint in the hologram and hence difficult to see in the photographs of it. Thus when reconstructed its appearance was indistinct. This was a limitation of the optical systems' ability to image very faint objects rather than a problem of reconstruction resolution.

To demonstrate the systems ability to handle information from a density field the reconstruction of a holographic interferogram of a convection plume was undertaken. Views from a hologram of a soldering iron showing free convection were taken and processed to give spanwise averaged density maps, which were then used to reconstruct the field. Using the Gordon and Herman MART algorithm and our 3-D projection scheme a reconstruction of the field was obtained despite a very limited variation of viewing angle being possible with this hologram. Thus the system was indeed able to handle real data from a variable density field.

11.0 Conclusions

Tomographic techniques for the reconstruction of three dimensional fields from data sets captured over a limited range of views have been developed and demonstrated. As tomographic reconstruction usually requires data from a wide range of view points this was a significant result.

The three dimensional projection scheme used in this tomographic reconstruction system was produced specifically to address the limited viewing angle problem. This significantly improved the resulting reconstruction quality in comparison to conventional techniques.

The three dimensional projection was used in combination with an iterative reconstruction algorithm, the Gordon and Herman MART algorithm, tests having shown this to be the most effective iterative algorithm. This combination of projection scheme and algorithm was novel and produced superior results to the other algorithms tested.

A practical system was developed around this approach and used to reconstruct real data. This was used to reconstruct a holographic interferogram produced by Rolls Royce of the shockwave generated by a turbine blade. In the resultant reconstruction the blades shape was clearly visible, demonstrating the systems ability to handle solid objects in a hologram.

The systems ability to handle information from holographic interferograms with a number of fringes was demonstrated by applying it to a hologram of a convection plume. Views from this hologram were successfully processed to give spanwise averaged density maps, and these were then used as data to

reconstruct the field, despite a very limited variation of viewing angle being possible with this hologram. Thus our system was indeed able to handle real data from a variable density field.

To summarise, this work has successfully demonstrated the suitability of direct three dimensional projection schemes, operating with MART type algorithms, for the reconstruction of limited angle of view data sets.

12.0 Further Work

Further improvements in the systems operation might be made by trying different algorithms with the 3-D projection scheme. The methods of simulated annealing and constrained maximum entropy optimisation have been suggested as methods suitable for limited data problems and our software could be adapted to use these approaches.

Applying the system to limited view problems would be a logical path of further work to follow. The operation of the tomographic reconstruction software and image acquisition system is such that irregularly spaced images can be processed, allowing a wide range of real world situations to be studied. For instance in wind tunnel experiments where available views are limited by window spacing around the tunnel, applying our technique might allow the reconstruction of the air density around the test object. Each window could be considered as a single viewing direction and the data from each entered on this basis.

Colour tomography using data generated by thermally sensitive liquid crystals encapsulated and seeded in a medium has been considered during the development of our system. Reconstructing this data would give a three dimensional temperature variation map for the field being studied. A colour reconstruction would require either the capture of a separate red, green and blue image from each view point and the reconstruction of each colour field or the reconstruction of a hue, saturation and intensity field from HSI images. For this to work the spacing between the seeded particles would have to be large enough to minimise the obscuration of distant particles by those closer to the view point, while

being present in sufficient quantities to accurately measure the temperature changes in the medium. Provided these conditions could be met the colour reconstruction should be possible.

13.0 Appendices

Appendix 13.1 Photographing the holograms

The holograms were photographed about a cone of views as shown in figure A1. From this it can be seen that a perpendicular

Figure A.1. The Views Positions From Angular Measurements.
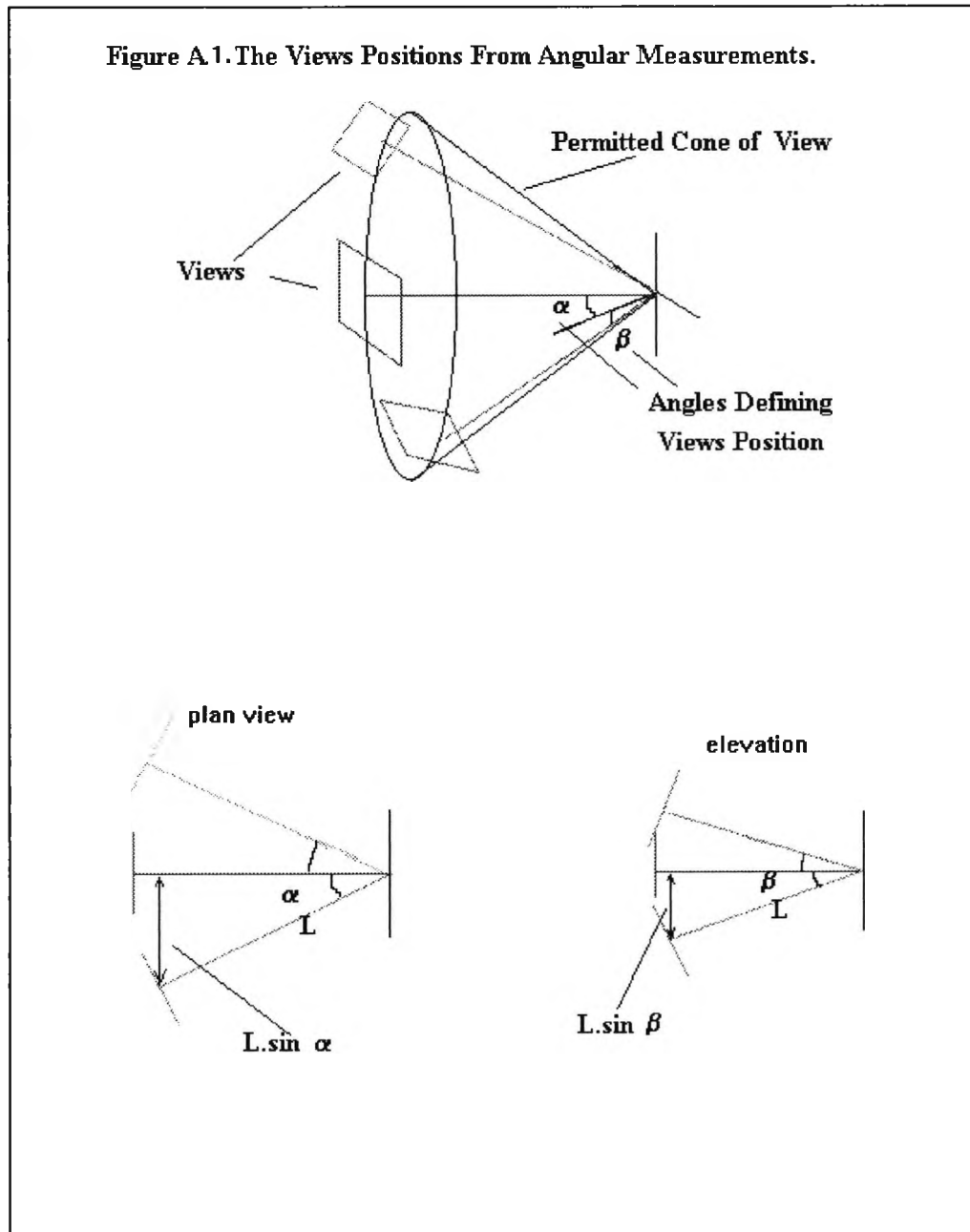
projection from the centre of each view meets all

others at a single point on the object. Thus the relative direction of a projection with respect to any other can be expressed by two angles, alpha and beta as shown in figure A1. If the length of each projection from the common point, (in our case a selected point in the holographic image), is known then the relative position of each view can also be fixed from these two angles. Now as the views are taken about a cone we can assume the length of each projection is equal and make this length arbitrary in our calculations while still maintaining the correct alignment.

The constants required for the position of each view were estimated by considering the views to be converging to a single point and thus making the absolute distance of the view plane arbitrary, say 10 units. Thus the values for the displacements in the x, y, and z axes are given by the following equations:

$$x = 10 - (10 - 10\sin\beta - (L/2).\sin\beta)) - (10 - 10\cos\alpha - (L/2)\sin\alpha)$$

$$y = 10\sin\beta - (L/2 - (L/2)\cos\beta)$$

$$z = 10\sin\alpha - (L/2 - (L/2)\cos\alpha)$$

These are the values entered in the computer program with the angular measurements and result in the tomography program generating the correct geometric information.

13.2. The Image Sampling Program Segment

When a ray propagates through the reconstruction field its path is marked in a ray tracing array by assigning a value to each voxel it passes through in

this array. These values are then used to select the voxels that affect the total attenuation experienced by a given ray. This method of marking voxels is simple to implement but only functions correctly when a single ray passes through a given voxel at a given stage in the computer program. If for instance two rays were considered which passed through the same voxel the marker value of the first would be over written with the marker value of the second thus losing the data of the first ray, as shown in figure A2.1 .
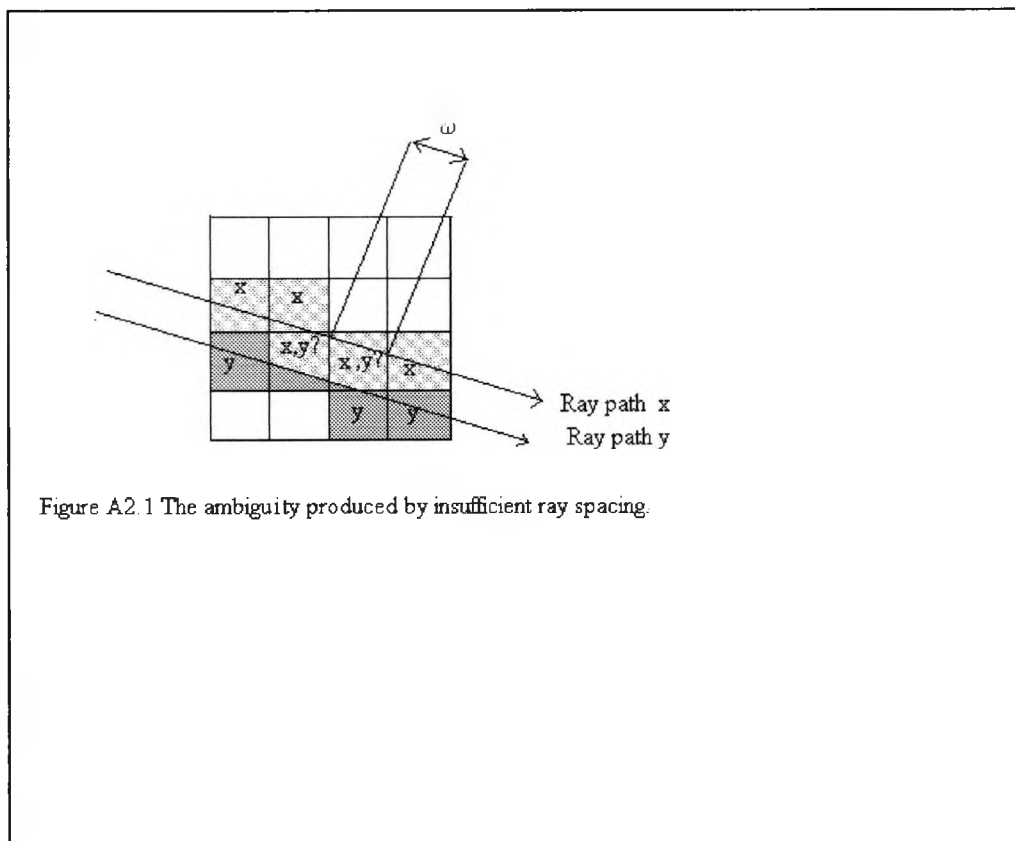
Figure A2.1 The ambiguity produced by insufficient ray spacing.

Now as a typical application involves approximately 25 rays per voxel from a single view this condition

must be considered. In order to retain the basic simplicity of the tracing scheme, and at the same time to overcome this problem a scheme was devised whereby rays were selected for processing which had sufficient spacing between them so as not to pass through any common voxels. Provided the spacing between two rays is 1.5 times the length of the side of a voxel there is no danger of them passing through the same voxel for the cone sampling regime being considered. Thus when a view from the 512x512 pixel camera is

Figure A2.2 The Data Sampling Grid.
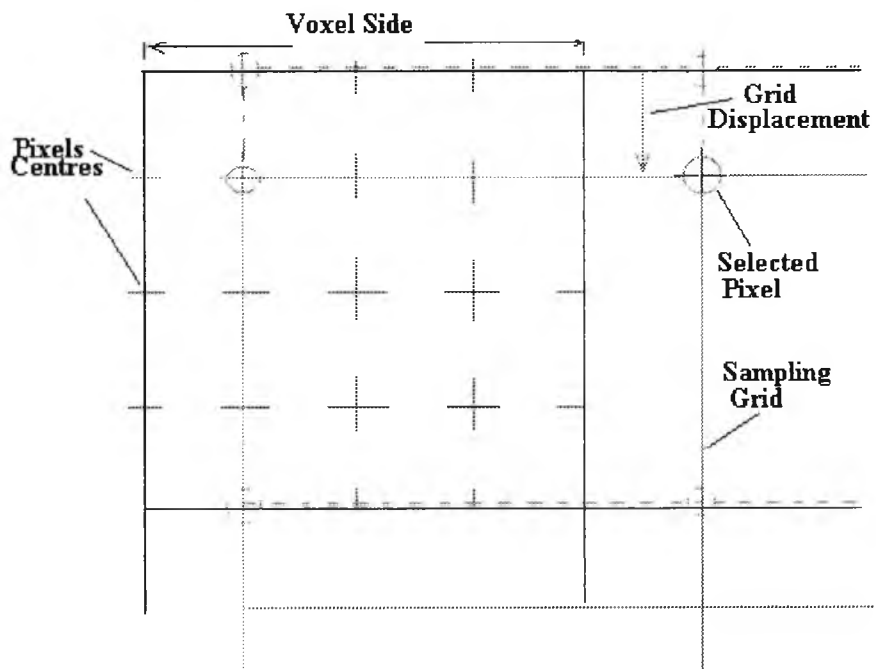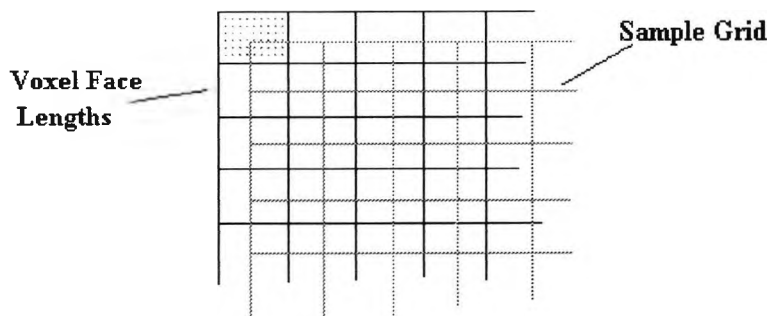
considered a 50x50 grid is used to sample this data to give the correct spacing between these ray points, this is illustrated in figure A2.2. When all the data has been processed the grid can *re-sample* the data except that this time it is displaced by one pixel. By re-sampling the 512x512 view until all the pixel values have been considered all the data in the view are extracted.

13.3. The Hologram Reconstruction Optics

The light from a He-Ne laser was sent round an optical path and then through a diverging lens to give a cone of light to illuminate the holographic plate.
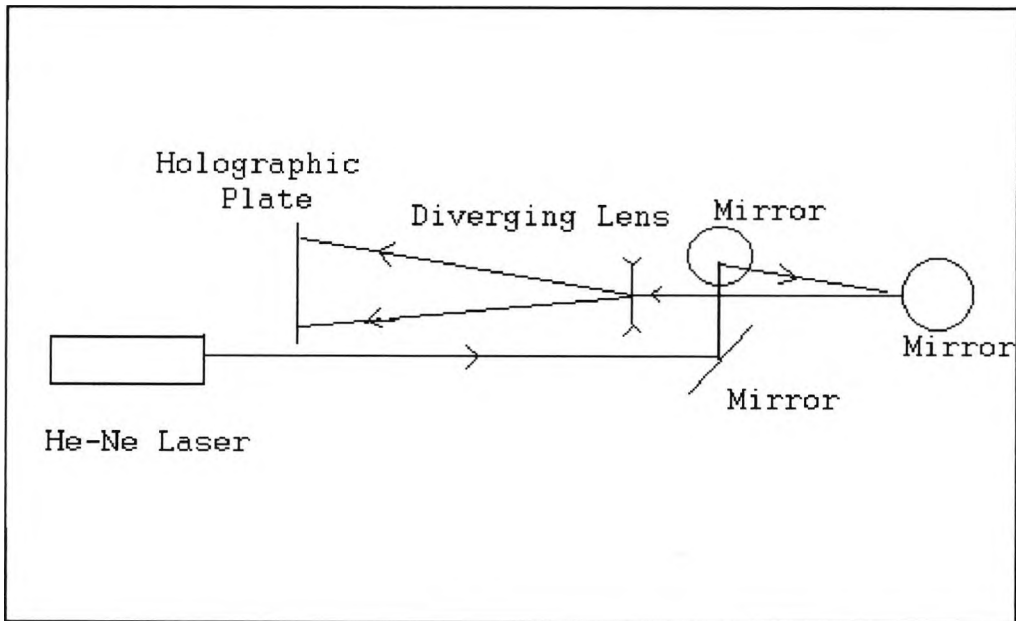
Figure A3. Hologram Reconstruction Optics

The He-Ne laser was used to give a visible image upon reconstruction rather than the Ruby laser to produce the holographic exposure originally. The wavelength shift caused by using different laser sources causes a scaling shift in the reconstruction. The size alteration was uniform across the image and thus the relative dimensions in the image are retained. As the reconstruction was relatively small the depth of focus of the telephoto lens used was sufficient to photograph the reconstruction.

13.4 The illumination of the soldering iron

Holographic Plate

Soldering Iron

Light
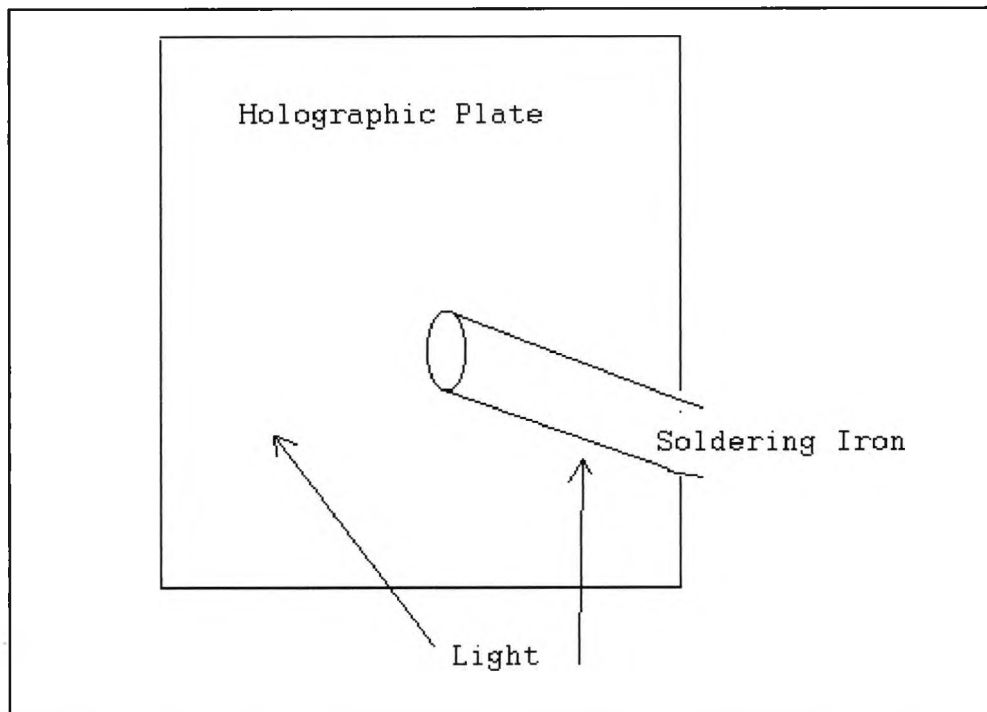
Figure A4. The illumination of the soldering iron

13.5 The fringe information relative to the soldering iron

Holograms Captured Volume

Fringes

Depth
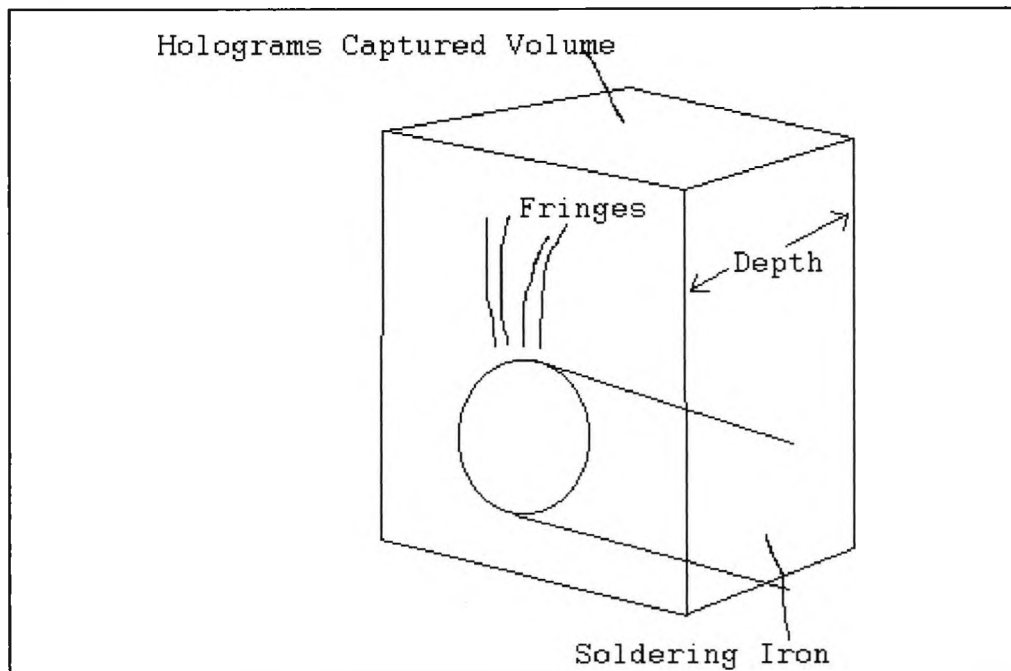
Soldering Iron

Figure A5. The soldering iron and the fringe data relative to it.

References

1.   Y.Censor, Finite Series-Expansion Reconstruction Methods, Proc. IEEE Vol. 71, No. 3, 1983.

2.   R.Gordon, R. Bender, and G.T. Herman, Algebraic reconstruction techniques (ART) for three-dimensional electron microscopy and x-ray photography. J. Theor. Biol. Vol 29, 471-481, (1970).

3.   R. Gordon and G.T. Herman, Three-dimensional reconstruction from projections: a review of algorithms. Int. Rev. Cytol. Vol. 38, 111-151, (1974).

4.   D. Verhoeven, Multiplicative algebraic computed tomographic algorithms for the reconstruction of multidirectional interferometric data. Optical Engineering, Vol. 32, No.2 410-419, (1993).

5.   A. Lent, A convergent algorithm for maximum entropy image restoration, with a medical x-ray application. Proc. SPIE Image Analysis and Evaluation, 249-257, (1977).

6.   S.S. Cha and H. Sun, Tomography for reconstructing continuous fields from ill-posed multidirectional interferometric data. Applied Optics, Vol. 29, No. 2, (1990).

7.   S.F. Gull and T.J. Newton, Maximum entropy tomography.
Applied Optics, Vol. 25, No.1, 156-160, (1986).

8.   Zhang and G.A. Ruff, Reconstruction of refractive index fields by using relative fringe data. Applied Optics, Vol. 32, No.16, 2921-2926, (1993).

9. D.D. Verhoven, Application of computer tomography and holographic interferometry to the study of transparent media.
Repot No. 38501, Institut Francais de Petrole, BP311, (1990).

10. G. Minerbo, MENT: A maximum entropy algorithm for reconstructing a source from projection data. Computer Graphics and Image Processing, Vol. 10 (1979).

11. R. Frieden and C. Zoltani, Maximum bounded entropy: application to tomographic reconstruction. Applied Optics, Vol.24, No. 23, (1985).

12. J. Hunter and M.W. Collins, Three-dimensional refractive index field reconstruction from holographic interferograms. Int. Journal of Optoelectronics, Vol.4, No. 2, (1989).

13. R. Rangayyan, A. Dhawan, and R. Gordon, Algorithms for limited-view computer tomography: an annotated bibliography and a challenge. Applied Optics, Vol. 24, No. 23, (1985).

14. J.G. Colsher, Iterative three-dimensional image reconstruction from tomographic projections. Computer Graphics and Image Processing, Vol. 6, pp. 513-537, (1977).

15. M. Schlindwein, Iterative three-dimensional reconstructions from twin-cone beam projections. IEEE Trans. Nuclear Sci., Vol. NS-25, pp. 1135-1143, (1978).

16. M.D. Altschuler, Y. Censor, P.B. Eggermont, G.T. Herman, Y.H. Kuo, R.M. Lewitt, M. McKay, H.K. Tuy, J.K. Udupa, and M. Yau, Demonstration of a software

package for the reconstruction of the dynamically changing structure of the human heart from cone beam x-ray projections. Journal Medical Systems, Vol. 4, pp. 289-304, (1980).

17. G.N. Hounsfield, A method of and apparatus for examination of a body by radiation such as x or gamma radiation, The Patent Office, London, Patent Spec. 1283915, (1972).

18. S. Kaczmarz, Angenaherte Auflosung von Systemen Linearer Gleichungen. Bull. Acad. Polon. Sci. Lett., Vol. 35, pp 355-357, (1937).

20. J.D. Trolinger and J.C. Hus, Flowfield diagnostics by holographic interferometry and tomography. Procedings SPIE, (1991).

21. D.W. Watt, Synthetic MAP Tomographic Reconstruction of Turbulent Flow Fields, Proc. SPIE, Int. Symposium on Optics, Imaging and Instrumentation, (1993).

22. K.M. Hanson, Object detection and amplitude estimation based on maximum a posteriori reconstruction, Proc. SPIE 1231, (1990).

23. W.E. Smith, R.G. Paxman, and H.H. Barrett, Image reconstruction from coded data: I. Reconstruction algorithms and experimental results, J. Opt. Soc. Am. A, 2, pp. 491-500, (1985).

24. S. Geman and D. Geman, Stochastic Relaxation, Gibbs distributions, and the Bayesian restoration of images. IEEE Trans. Pattern. Anal. Machine Intell., PAMI-6, pp. 721-741, (1984).

25. G.T. Herman, Two direct methods for reconstructing pictures from projections: A comparative study, Computer Graphic and Image Processing, 1, pp.123-144, (1972).

26. R. Kikuchi and B.H. Soffer, Maximum entropy image restoration : the entropy expression. Journal of the Optical Society of America, Vol. 67, no. 12, (1977).

27. B.R. Frieden, Restoring with maximum likelyhood and maximum entropy. Journal of the Optical Society of America, Vol. 62, no.4, (1972).

28. J.G. Sanderson, Reconstruction of fuel pin bundles by a maximum entropy method. IEEE Trans. Nuclear Sci. NS 26, no.2, (1979).

29. R. Gordon , A tutorial on ART. IEEE Trans. on Nuclear Science, NS-21, 1974, pp.78-93, (1974).

30. D. Gabor, A new microscope principle. Nature, Vol. 161, pp. 777-778, (1948).

31. E.N. Leith and J. Upatnieks, Wavefront reconstruction with diffuse illumination and 3-dimensional objects. Journal of the Optical Society of America, Vol. 54, pp. 1295-1301, (1964).

32. E.N. Leith and J. Upatnieks, Wavefront reconstruction photography. Physics Today, Vol. 18, No. 8, pp. 26-32, (1965).

33. A.J. Decker, Neural networks for calibration tomography.
Proc. SPIE conf. Optics, Imaging and Instrumentation, (1993).

34. R.J. Parker and D. G. Jones, Holographic flow visualisation in rotating transonic flows. Inst. Phys. Conf. Ser. No. 77: Section 3, (1985).

35. R.J. Parker, Extraction of 3-d flow data from transonic flow holograms. Proc. SPIE Industrial Optoelectronic Measurement Systems Using Coherent Light, Vol. 863.

36. R.J. Parker, Holography the RR experience , Journal Turbo Jet Engineering, (1993).

37. L.O Heflinger, R.P. Wuerker, and R. E. Brooks, Holographic interferometery, Journal of Applied Physics, Vol. 37, pp642-649, (1966).

38. H.M. Chau and G.J. Mullaney, An example of the application of pulsed light holography to aerodynamics, Applied Optics, Vol. 6, p 981, (1967).

39. R.F. Wuerker, R.J. Kobayashi, L.D. Heflinger and T.C. Ware, Application of holographic flow visualisation within rotating compressor blade row, NASA, CR-121264, (1974).

40. C.M. Vest, Holographic Interferometry, Wiley, (1979).

41. M.H. Horman, An application of wavefront reconstruction to interferometry, Applied Optics, Vol. 4, pp333-336, (1965).

42. R.L. Powell and K.A. Stetson, Interferometric analysis by wavefront reconstruction. JOSA, Vol. 55, pp 1593-1598, (1965).

43. K.A. Stetson and R.L. Powell, Hologram

interferometry, JOSA, Vol. 55, (1965).

44.   J.M. Burch, The application of lasers in
production engineering, Production Engineering, Vol.
44, pp 431-442, (1965).

45.   K.A.   Haines and B.P. Hildebrand, Surface-
deformation measurement using wavefront reconstruction
technique, Applied Optics, Vol. 5, pp 595-602, (1966).

46.   L.O. Heflinger, R.F. Wuerker, and R.E. Brooks,
Holographic   interferometry,   Journal   of   Applied
Physics, Vol. 37, pp 642-649, (1966).

47.   L.O. Heflinger, R.F. Wuerker, and R.E. Brooks,
Interferometry with a holographically reconstructed
reconstruction   comparison   beam,   Applied   Physics
Letters, Vol. 7, pp. 248-249, (1965).

48.   S. Cha and C.M. Vest, Tomographic reconstruction
of strongly refracting fields and its application to
interferometric   measurement   of   boundary   layers,
Applied Optics, Vol. 20, No. 16, pp. 2787-2794,
(1981).

49. P.J. Bryston-Cross, T. Lang, M.L.G. Oldfield,
R.J.G. Norton, Interferometric measurements in a
turbine cascade using image-plane holography, Journal
of Engineering for Power, Vol. 103, pp.124-30, (1981).

50. C.J. Moore, D.G. Jones, C.F. Haxell, P.J.
Bryanston-Cross, R.J. Parker, Optical methods of flow
diagnostics in turbomachinery, Proc. International
Conference on Instrumentation in Aerospace Simulation
Facilities, IEEE, pp. 244-255, (1981).

51. A.J. Decker, Holographic flow visualisation of

time-varying shockwaves. Applied Optics, Vol. 20, pp. 3120-26, (1981).

52. A.J. Decker, Fringe localisation requirements for three-dimensional flow visualisation of shockwaves in diffuse-illumination double pulse holography. NASA TP1868, (1982).

53. G.W. Faris and R.L. Byer, Three-dimensional beam-deflection optical tomography of a supersonic jet, Applied Optics, Vol. 27, pp. 5202-5212, (1988).

54. R.D. Matulka and D.J. Collins, Determination of three-dimensional density fields from holographic interferometry. Journal of Applied Physics, Vol. 42, pp 1109-1119, (1971).

55. D.W. Watt and C.M. Vest, Turbulent flow vizualisation by interferometric integral imaging and computer tomography. Exp. Fluids, Vol 8, pp301-311, (1990).

56. D.W. Watt, Column relaxed algebraic reconstruction algorithm for tomography with noisy data. Applied Optics, Vol. 33, no. 20, pp. 4420-4427, (1994).

57. Adler and Guard, A neutral network image reconstruction technique for electrical impedance tomography. IEEE, Trans. on medical imaging, Vol. 13, no. 4, pp. 594-600, (1994).

58. Neural Network for pattern association in electrical capacitance tomography. IEE Proceedings Circuits, Devices and Systems, Vol. 141, no.6, pp517-521, (1994).

59. H.Q. Guan and R. Gordon, A projection access

order for high speed ART convergence. Physics in Medicine and Biology, Vol. 39, no. 11, pp.2005-2022, (1994).

60. N. Jan, C.Y. Chen, C.H. Yek, T.R. Yek and M. T. Wang, 3-D image reconstruction using cone-beam tomography. NDT and E international, Vol. 27, no. 2, pp. 83-87, (1994).

61. M. Zinth and R. Mc Williams, An improved optical tomographic device. Review of Scientific Instruments, Vol. 65, no. 8, pp. 2574-2579, (1994).

62. S.S. Cha, Holographic tomography for reconstructing flow fields: a review, AIAA paper 92-3934 at the 17th Aerospace Ground Testing Conference, (1992).

63. K.M. Hanson and G.W. Wecksung, Bayesian approach to limited-angle reconstruction in computer tomography. JOSA, Vol. 23, pp. 1501-1509, (1983).

64. P. Oskoui-Fard and H. Stark, Tomographic image reconstruction using the theory of convex projections. IEEE Trans. on Medical Imaging, Vol. 7, pp. 45-58, (1988).

65. B.J. Sullivan, and A.K. Katsaggelos, New termination rule for linear iterative image restoration algorithms. Optical Engineering, Vol. 29, pp. 471-477, (1990).

66. G.T. Herman and A. Lent, Iterative reconstruction algorithms. Comput. Biol. Medical, Vol. 6, pp. 273-294, (1976).

67. M. Tasto, Reconstruction of random objects from noisy projections. Computer Graphics and Image

Processing. Vol.6, pp. 103-122, (1977).

68. A.V. Lakshminarayanan and A. Lent, Method of least squares and SIRT in reconstruction. Journal of Theoretical Biology, Vol. 76, pp. 267-295, (1979).

69. G.T. Herman, A.V. Lakshminarayanan, and A. Lent, The reconstruction of objects from shadowgraphs with high contrast. Pattern Recognition, Vol.7, pp. 157-165, (1975).

70. G.T. Herman, A. Lent, and S.W. Rowland, ART: Mathematics and applications. Journal of Theoretical Biology, Vol. 42, pp. 1-32, (1973).

71. P. Gilbert, Iterative methods for the three-dimensional reconstruction of an object from projections. Journal of Theoretical Biology, Vol. 36, pp. 105-117, (1972).

72. R.M. Rangayyan and R. Gordon, Streak prevention image reconstruction with ART and adaptive filtering. IEEE Trans. Medical Imaging, Vol. 1, pp.173, (1983).

73. C.R. Crawford and A.C. Kak, Aliasing artefacts in computerized tomography. Applied Optics, Vol. 18, pp. 3704, (1979).

74. C.M. Vest, Formation of images from projections: Radon and Abel transforms. JOSA, Vol. 64, no. 9, pp.1215-1218, (1974).

75. K. Tam and V. Perez-Mendez, Limited-angle three-dimensional reconstructions using Fourier transform iterations and Radon transform iterations. Optical Engineering, Vol. 20, no.4, pp. 586-589, (1981).

76. H. Kudo and T. Saito, Feasible cone beam scanning methods for exact reconstructionin three-dimensional tomography. JOSA, Vol. 7, no. 12, (1990).

77. R.J. Santoro, H.G. Semerjian, P.J. Emmerman and R. Goulard, Optical tomography for flow field diagnostics. Int. Journal Heat and Mass Transfer, Vol. 24, no. 7, pp.1139-1150, (1981).

78. H.M. Hertz, Experimental determination of 2-D flame temperature fields by interferometric tomography. Optics Communications, Vol. 54, no. 3, pp. 131-136, (1985).

79. P. Riso, P. Grangeat, P. Sire, P. Lemasson, and Melennec, Comparison of two three-dimensional x-ray cone-beam reconstruction algorithms with circular source trajectories. JOSA, Vol. 8, no. 10, (1991).

80. H. Tan and D. Modarress, Algebraic reconstruction technique code for tomographic interferometry. Optical Engineering, Vol. 24, no. 3, (1985).

81. A.J. Decker and S.H. Izen, Three-dimensional computer tomography from interferometric measurements within a narrow cone of views. NASA Technical Memo. 103257, (1991).

82. N.J. Dusaussoy and I.E. Abdou, The extended MENT algorithm: A maximum entropy type algorithm using prior knowledge for computer tomography. IEEE Trans. on Signal Processing, Vol. 39, no.5, (1991).

83. R.T. Smith, C.K. Zoltani, G.J. Klen, and M.W. Coleman, Reconstruction of tomographic images from sparse data sets by a new finite element maximum entropy approach. Applied Optics, Vol. 30, no. 5,

(1991).

84. D.W. Watt and C.M. Vest, Consistant iterative convolution: a coupled approach to tomographic reconstruction. JOSA, Vol. 6, no. 1, pp. 44, (1989).

85. S. Cha, Interferometric tomography for three-dimensional flow fields via envelope function and orthogonal series decomposition. Optical Engineering, Vol. 27, no. 7, pp. 557-563.

86. B.P. Medoff, W.R. Brody, M. Nassi, and A. Macovski, Iterative convolution backprojection algoritms for image reconstruction from limited data. JOSA, Vol. 73, no. 11, pp. 1493-1500, (1983).

87. R. Synder , L. Hesselink, Optical tomography for flow visualisation of the density field around a rotating helicopter blade. Applied Optics, Vol. 23, no. 20, pp 3650-3656, (1984).

88. C. Soller, R. Wenskus, P. Middendorf, G.E. Meier, and F. Obermeier, Interferometric tomography for flow visualisation of density fields in supersonic jets and convective flow. Applied Optics, Vol. 33, no. 14, pp. 2921-2932, (1994).

89. H. Kudo and T. Saito, Sinogram recovery with the method of convex projections for limited-data reconstruction in computer tomography. JOSA, Vol. 8, no. 7, pp.1148-1160, (1991).

90. K.C. Tam , J.W. Eberhard, and K.W. Mitchell, Incomplete-data CT image recostructions in industrial applications. IEEE Trans. on Nuclear Science, Vol. 37, no. 3, (1990).

91. K.C. Tam, V. Perez-Mendez, and B. Macdonald, 3-D object reconstruction in emission and transmission tomography with limited angular input. IEEE Trans. in Nuclear Science, Vol. NS- 26, pp. 2797, (1979).

92. K.C. Tam and V. Perez-Mendez, Tomographical imaging with limited-angle input. JOSA, Vol. 71, pp.582, (1981).

93. S. Bahl and J.A. Liburdy, Three-dimensional image reconstruction using interferometric data from a limited field of view with noise. Applied Optics, Vol. 30, pp 4218-4226, (1991).

94. D. Yan and S.S. Cha, Computational and Interferometric Systems for Real-Time Limited-View Tomography of Flow Fields. Applied Optics, Vol. 37, pp.1159-1164, (1998).

95. M. Schweiger and S.R. Arridge, Comparison of Two- and Three-Dimensional Reconstruction Methods in Optical Tomography. Applied Optics, Vol. 37, pp.7419-7428, (1998).

96. G.N. Blinkov, N.A. Fomin, and D.E. Vitkin, Speckle Tomography of Gas Flows. Atlas of Visualisation, Vol. 1, pp.171-182, Pergamon Press, (1993).

97. N.A. Fomin, 30 Years of Speckle Photography, (Keynote Lecture). International Seminar on Optical Methods and Data Processing in Heat and Fluid Flows, IMechE, pp.433-442, (1998).

98. D.J. Cha and S.S. Cha, Holographic Interferometric Tomography for Limited Data Reconstruction. AIAA Journal, Vol. 34, pp.1019-1026, (1996).